NON-INVASIVE DETECTION OF HUMAN VITAL SIGNS USING CONCURRENT DUALBAND RF SENSOR

Ph.D. THESIS

by

BRIJESH R. IYER

DEPARTMENT OF ELECTRONICS & COMMUNICATION ENGINEERING
INDIAN INSTITUTE OF TECHNOLOGY ROORKEE
ROORKEE-247667 (INDIA)
DECEMBER, 2014

NON-INVASIVE DETECTION OF HUMAN VITAL SIGNS USING CONCURRENT DUALBAND RF SENSOR

A THESIS

Submitted in partial fulfilment of the requirements for the award of the degree of

DOCTOR OF PHILOSOPHY

in

ELECTRONICS & COMMUNICATION ENGINEERING

by

BRIJESH R. IYER

DEPARTMENT OF ELECTRONICS & COMMUNICATION ENGINEERING
INDIAN INSTITUTE OF TECHNOLOGY ROORKEE
ROORKEE-247667 (INDIA)
DECEMBER, 2014

INDIAN INSTITUTE OF TECHNOLOGY ROORKEE, ROORKEE

CANDIDATE'S DECLARATION

I hereby certify that the work which is being presented in the thesis entitled **" NON-INVASIVE DETECTION OF HUMAN VITAL SIGNS USING CONCURRENT DUALBAND RF SENSOR "** in partial fulfilment of the requirements for the award of the Degree of Doctor of Philosophy and submitted in the Department of Electronics and Communication Engineering of the Indian Institute of Technology Roorkee, Roorkee is an authentic record of my own work carried out during a period from **July-2011 to December-2014** under the supervision of Dr. N. P. Pathak, Associate Professor, Department of Electronics & Communication Engineering, and Dr. Debashis Ghosh, Associate Professor, Department of Electronics & Communication Engineering, Indian Institute of Technology Roorkee, Roorkee.

The matter presented in the thesis has not been submitted by me for the award of any other degree of this or any other Institute.

(BRIJESH R. IYER)

This is to certify that the above statement made by the candidate is correct to the best of our knowledge.

(Dr. N.P.Pathak)
Supervisor

(Dr. Debashis Ghosh)
Supervisor

Dated: _____

ईशवराचा लेश मिळे तरि ।
मूढयत्न शेवटीं जातो ।।

With a Smallest Measure of God's Grace.....

Even the Mediocre Attempt Comes To Fruition

Acknowledgements

Though only my name appears on the cover of this thesis, many individuals have contributed towards its commencement. I'm thankful to all individuals who have made this dissertation possible and due to whom my research experience has been one that I will relish eternally.

My deepest gratitude is to my supervisors, **Dr. Nagendra Prasad Pathak and Dr. Debashis Ghosh**. I have been incredibly providential to have advisors who had given me the freedom to walk around on my own and also the direction to recuperate when my steps faltered. Their patience and support helped me overcome crisis situations and complete this dissertation. I am also thankful to them for careful reading and commenting on countless revisions of this manuscript. I hope that one day I would become a good advisor to my students as Dr. N. P. Pathak and Dr. D. Ghosh Sir has been to me.

I am grateful to my research committee members **Prof. Vinod Kumar, Prof. M. V. Kartikeyan, Prof. Dharmendra Singh** for taking interest in my work. I thank them for their encouragement and practical advice towards my research work.

This journey began with the motivation and support of **Prof. A. W. Kiwlekar, Prof. S. B. Deosarkar, Prof. P. K. Brahmankar** (Dr. BATU, Lonere-MS-India), **Prof. G. V. Chowdhary** (Director, School of Comp. Sci. SRTMU, Nanded), **Prof. S. N. Talbar and Prof. R. M. Manthalkar** (SGGSIE&T, Nanded-MS-India). Most

importantly, I'm thankful for the rock-strength support of **Prof. S. L. Nalbalwar, Prof. & Head, Dept. of E & TC Engg. Dr. BATU, Lonere - Maharashtra-India** without whom it was next to impossible to join this program.

I am also indebted to the Radio Frequency Integrated Circuit (RFIC) laboratory members for technical discussions on my views and helping me comprehend and enrich my views. I'm in debt of my dear friends **Mr. Vivek Sharma, Mr. Prateek Dolas, Mr. Pravin R. Prajapati, Mr. Kola T. (Research Scholars, IITR), Mr. Kapil Saraswat (Research Scholar, IITK) and Dr. Amit P. Shesh (Assistant Professor, Dr. BATU, Lonere-MS-India)** for their unconditional support during my research tenure.

I am also thankful to the technical staff **Mr. Gour and Mr. Rajaram** for upholding all the equipments in my lab efficiently. I believe that they are the best technicians in IIT Roorkee. I'm also thankful to **Mr. Tarun Prasad and Mr. Arpit Kumar (Agilent Technology-India)** for providing various RF equipment for experimentation.

I'm short of words to express my feelings towards my **Mother-AKKA**, who had seen a dream...always motivated to do the best in the life. Most importantly, none of this would have been possible without the love and patience of **my wife-PRACHI**. She is instrumental right from joining of this program and has been a constant source of love, concern, support and strength all these years.

BRIJESH R. IYER

Author's Publications

International Journals

1. **Brijesh Iyer** and N. P. Pathak, "Concurrent dual−band LNA for non−invasive vital sign detection", *Microwave and Optical Technology Letters*, vol. 56, no. 2, pp. 391−394, Feb. 2014.

2. **Brijesh Iyer**, M. Garg, N. P. Pathak and D. Ghosh, "Detection and analysis of heartbeats and respiration rate using concurrent dual−band RF system", *Journal of Procedia Engineering*, vol. 64, pp. 185−194, 2013.

3. **Brijesh Iyer** and N. P. Pathak, "A Concurrent dual input dual output RF sensor for indoor human existence monitoring ", *IEEE Sensors Journal*, Under Revision since Nov. 2014.

International Conferences

1. **Brijesh Iyer**, N. P. Pathak and Debashis Ghosh, "Concurrent dualband patch antenna array for non−invasive human vital sign detection application", *IEEE Asia−Pacific Conference on Applied Electromagnetics (APACE−14)*, Johor Bahru, Malaysia, Dec. 2014, pp. 150−153.

2. **Brijesh Iyer**, N. P. Pathak and Debashis Ghosh, "Reconfigurable multiband concurrent RF system for non−invasive human vital sign detection", *Proceed-*

ings of IEEE R−10 Humanitarian Technology Conference(HTC−14), Chennai, India, Aug. 2014.

3. **Brijesh Iyer**, A. Kumar, N. P. Pathak and Debashis Ghosh, "Concurrent multi-band RF system for search and rescue of human life during natural calamities", *International Microwave and RF Conference (IMaRC−2013)*, New Delhi, India, Dec. 2013, pp. 1−4.

4. **Brijesh Iyer**, A. Kumar, and N. P. Pathak, "3.36 / 5.24 GHz Concurrent dualband oscillator for WiMax / WLAN applications", *International Microwave and RF Conference (IMaRC−2013)*, New Delhi, India, Dec. 2013, pp. 1−4.

5. **Brijesh Iyer**, A. Kumar, and N. P. Pathak, "Design and analysis of subsystems for concurrent dual−band transceiver for WLAN applications", *IEEE International Conference on Signal Processing and Communication (ICSC−2013)*, Noida, India, Dec. 2013, pp. 57−61.

6. **Brijesh Iyer**, M. Garg, N. P. Pathak and D. Ghosh, "Concurrent dualband RF system for human respiration rate and heartbeat detection", *IEEE International Conference on Information and Communication Technologies (ICT − 2013)*, Tamilnadu, India, Apr. 2013, pp. 563−567.

Award

1. Won the **IEEE IMaRC−2013 best paper award** for the paper entitled ***"Concurrent Multi-band RF System for search and rescue of human life during natural calamities"*** at International Microwave and RF Conference (IMaRC − 2013) held at New Delhi, India in Dec.− 2013.

Abstract

Conventionally, the human vital signs are detected using invasive methods. A non-invasive detection of the vital signs is an attractive alternative over the conventional methods due to its two-fold advantage over them. Firstly, the attention and cooperation from the human subject under test are optional. Secondly, it does not cause distrace to the human being as in case of conventional methods. In addition, the non-invasive method of human vital sign detection is, in general, free from periodic maintenance. Since 1970s, researchers and academicians started the effort towards the development of RF systems based on Doppler principle for applications like healthcare, military and disaster management. All such reported efforts are characterized by their non-invasiveness and use of a particular single band during measurements.

A number of noteworthy overseas research groups like the Centre for Radio Frequency Electronics Research (CREER) in Canada, Radio Frequency Circuits and Systems (RFCS) research group in the University of Florida, Department of Electrical Engineering at the University of Hawaii, Yonsei University in Seoul,Korea and the 'WiPLi' Lab in the University of Udine, Italy carried out research towards the development of a human VSD Radar. In India, research groups at several premier technological institutes like Centre for Applied Research in Electronics (CARE), IIT Delhi, IIT Kanpur, IISc Bangalore and IIT Roorkee are engaged in the design and development of non-invasive RF sensor for a variety of day-to-day applications. IIT Bombay in Mumbai

is also engaged in the study of biological effects of radiation on the human body.

For any non-invasive human vital sign measurement system, the detection accuracy and sensitivity are two very crucial factors. With single band operation, either accuracy or noise sensitivity in detection can be achieved in a particular operation. The challenging issue in front of the existing single band NIVSD system is to bridge the trade off between the detection sensitivity and the amount of noise in the received signal. The performance of the existing single band NIVSD systems may be improved by using multiband operation. While higher frequency allows signal detection even with very minute variations but at the cost of increased noise, the lower frequency band minimizes noise with inferior detection sensitivity. The cross-correlation between the individual base band signals will emphasize significant information present in both the bands while suppressing unwanted signal components.

A concurrent multiband system can fulfill these requirements. Hence, this thesis aims at designing and development of a concurrent dualband RF system for human vital sign detection. Multiband transceiver architecture may be implemented using parallel, switchable or concurrent arrangements of the basic functional blocks. Use of parallel system architecture for the concurrent operation is less attractive due to high power consumption, complex hardware and its bulky nature. A switched mode multiband system suffers from the drawback of inconsistent measurement conditions for the same human subject due to switching delay. Consequently, these two schemes are not viable due to one or more reasons like the requirement of a large hardware, high-power consumption, and / or complex radio architecture.

The current trend in the area of Microwave / Millimeter wave integrated circuit research is to reduce the system losses, component count and power consumption level so that the RF systems can be used as a portable handheld device. A concurrent multiband system, based on hardware sharing, fulfils all these criteria. In view of this, the present thesis aims at designing and development of a concurrent dualband RF sensor for human vital sign detection.

The research work reported in this thesis focuses on the design, implementation and characterization of a concurrent dualband RF sensor for non-invasive detection of human vital signs. Out of many vital signs, the human life and its existence can be ascertained by virtue of its respiration and heartbeat signal. Hence, respiration and heartbeat signal of the human being are considered as the vital sign for the experimentation. The proposed sensor operates simultaneously at dual frequency bands centered at 2.44 GHz and 5.25 GHz. The sensor prototype is developed using indigenously designed concurrent dualband subsystem and few commercially available components. Finally, a hardware prototype of the proposed RF sensor has been developed and experimentally characterised to validate the concept.

Table of Contents

List of Figures

List of Tables

Chapter 1

Introduction

1.1 Introduction

Recently, in June-2013, thousands of people lost their lives due to heavy flood and landslides in the hilly area of the Uttarakhand state of India. The quick search and rescue operation was worst affected due to lack of suitable portable wireless sensors to ascertain the human life under debris as the electric power supply system, roads and communication network in the region were destroyed due to natural calamity. The necessary of wireless and non-invasive sensor in such a situation was heavily felt by the rescue team as well as the research community.

Another important application scenario is in rural India, where a large number of unattended and uncovered bore well pit is the cause of human life disaster. Due to lack of literacy and awareness, young children usually fall inside it, which may be fatal. With existing rescue mechanism, one can not ascertain the life until the rescue operation is over. With a wireless non-invasive sensor, it may be possible to keep track of the human life during the rescue operation thereby guiding the rescue team to decide its course of action.

A wireless and non-invasive sensor may also be useful in a variety of applications like through-the-wall detection for presence of human being, remote monitoring of

patients' health in hospitals and infant care units, to ascertain the life of wounded soldiers in battlefields, in the elderly people home-care, in structural health monitoring system and to decide the viability of a particular construction.
Motivated from these day-to-day life needs, in this thesis, an effort is initiated to design and develop a handheld portable wireless sensor to detect the existence of human life non-invasively. Presence of human life is ascertained by the virtue of its vital signs such as respiration rate and heartbeat. Hence, they are used as vital signs to indicate the existence of a human life in the proposed sensor. For successful deployment of the device as a sensor for all the above mentioned applications, it must fulfill the various criteria such as:

- The device should be sensitive and capable of detecting even a minute variation in the human vital signs.
- The prediction accuracy of the device must be very high, i.e. it should be robust against any variation in the measurement conditions.
- The device should be portable enough to be easily carried from one place to another.
- The power consumption of the device should be minimum.
- Most importantly, the device must be cost-effective and reproducible.

As per the records available in the literature, efforts were initiated in early 1970s towards the non-invasive detection of human vital signs using radio frequency (RF) systems. In 1975, RF systems was used for the first time in the assessment of vital signs of human beings and animals [1]. Inspired by [1], analogous systems were proposed in [2–6]. The high sensitivity and miniaturized RF system based on Doppler principle have been employed as wireless sensors in numerous day-to-day applications, e.g. it is used in sleep disorder detection [7], vehicle speed measurement [8–11], location and distance estimation [12, 13], detection of food contamination, characterization

of materials and substances [14–17], human vital sign detection in battle fields and sports fields [18, 19], etc. These systems have also been found to be very useful by law enforcement agencies to inflict through-the-wall human detection and direction of arrival estimation [20–24] and in hospitals for non-invasive human healthcare monitoring [25–27]. Recently, the sensors based on the radar principle had been employed for structural health monitoring and aircraft fuel measurement [28, 29].

However, all these reported systems are focused on the use of a particular single band radio or instrument-based bulky systems. The challenging issue in the reported systems is the compromise between the detection sensitivity and the noise content in the signals. This factor has hindered the deployment of such systems as a portable sensor with high detection accuracy. In view of this, this thesis work is focused on the design, development and analysis of a concurrent dualband RF sensor for remote monitoring of human vital signs to detect and ascertain the presence of human life.

1.2 Theory of NIVSD Radar

Vital signs are the symptom of physiological information, frequently used to evaluate the fundamental body functionality. In healthcare terminology, measurements of vital signs are classified into two types: in-vivo (on or within a human body) and in-vitro (exterior of human body) [30]. Measurement of vital signs, in principle, involves recording of heartbeat and respiration rate, body temperature and blood pressure. Among these, the respiration rate and heartbeat are more significantly used vital signs to predict physical health of a human being since a close nonlinear relation exists between the respiratory and the cardiovascular systems. Both the heartbeat and respiration rate are modified by the target activity (i.e. the human being).

Vital signs changed continuously with the age of the human being. In general, measurement of the human vital signs may be principally carried out by either using the bioelectric energy generated within the cardiac muscle (direct method) or measure-

(a)

(b)

(c)

(d)

Figure 1.1: Motivation of the proposed thesis: (a) Disaster management (b) Social aspects (c) Health care applications (d) Battle field and Law enforcement applications.

ment of periodic displacement of the chest wall surface due to heart's contractions (indirect method). The direct method of assessment requires a measuring device capable of detecting changes in the surrounding electric field. The indirect method works on the principle of Doppler phase shift.

1.2.1 Working Principle

With advancements in technology, the traditional invasive vital sign monitoring systems are becoming less invasive and sophisticated. RF systems with non-invasive

monitoring of respiration and heartbeat provide a choice over well known invasive techniques. The non-invasive vital sign detection system works on the principle of change in phase of electromagnetic waves due to partial reflection at the separation of two mediums and propagation all the way through the medium. Such RF-based non-invasive measurement methods neither confines nor cause distress, as conventional vital sign measurement methods, to the human being. Table 1.1 provide a comparison between the traditional invasive systems and the non-invasive vital sign detection (NIVSD) system.

Table 1.1: Comparison of Invasive and NIVSD system

VSD system	Invasive	Wireless detection	Cooperation of subject	Detection Methodology
Invasive (Traditional)	Yes	Not Possible	Essential	Using Electrodes
NIVSD	No	Possible	Optional	Using RF Signals

This aspect of non-invasive detection becomes predominantly significant for long term continuous monitoring of vital signs of human being. Radio detection and ranging (Radar) is an RF system used for detection of objects with radio waves. Since its first report, Radar technology continuously progressed and established over the decades [31–34]. RF sensor system for NIVSD is based on Radar. It transmits a continuous wave (CW) signal in the medium. This signal is reflected back from the target object which is subsequently received in a receiver.

As per Doppler's principle, an object with time varying location produces a phase modulated reflected signal in proportion to its time varying location. Thus, RF system with chest as a target, receives a phase modulated signal in proportion to the time varying chest position. Accordingly, a baseband signal having intelligence about the

heartbeat and respiration rate can be retrieved after demodulation of the received signal. Based on this theory, a non-invasive heartbeat and respiration rate monitoring system has been developed in the literature illustrated.

1.2.2 Issues with the NIVSD Sensor

For successful deployment of an RF sensor for non-invasive detection of human vital signs; issues like clutters and phase noise, DC offset, null point detection, higher order harmonics along with appropriate signal processing techniques are the main challenges that need to be addressed. Moreover, the number of operational band governs the accuracy of detection. Each one of these issues or a combination of multiple issues may demean the total system performance. The evolution of RF system for NIVSD has its roots in unearthing solutions to these challenges.

1.2.2.1 Clutters

Clutters are superfluous echoes from the innate surroundings. Large clutter may masquerade echoes from the targets and in turn, decrease the system capacity. Clutter and phase noise effect may be minimized by using the same local oscillator (LO) source for transmission and reception. Phase noise of the reflected signal is allied with the LO and the degree of association depends on the time lag between the two signals. Smaller delays minimize the baseband noise significantly. This time delay is related to the distance between the RF system and targets, i.e. the range of the target. Accordingly, this phase noise reduction is recognized as range correlation effect [7]. Owing to the impact of clutters over the sensitivity of detection of very minute vital sign signals, several techniques have been proposed to overcome the effect of clutter, as discussed in the following chapters.

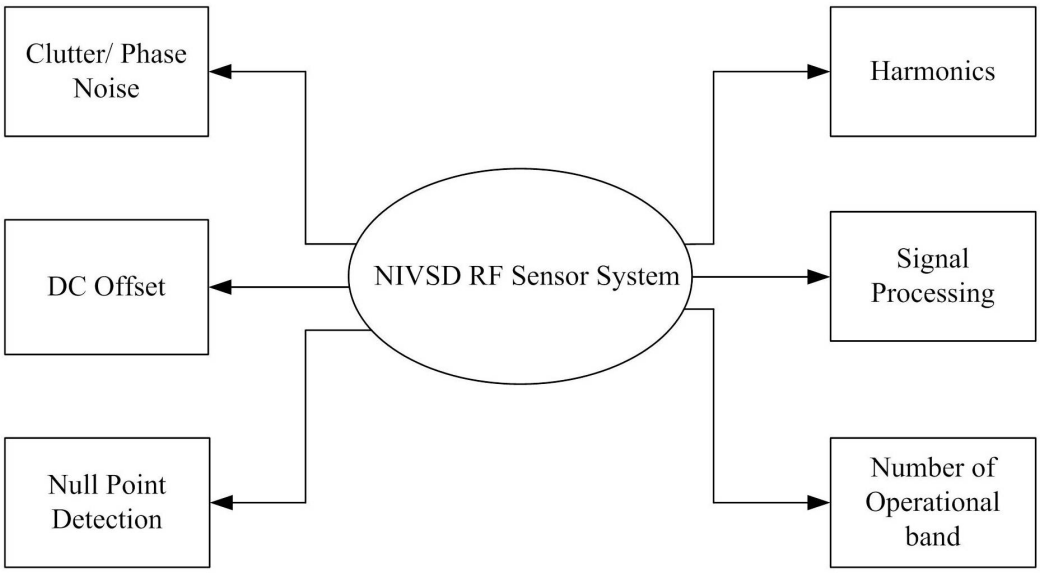

Figure 1.2: Challenges associated with a NIVSD RF sensor design.

1.2.2.2 DC Offset

DC offset results from receiver limitations, clutters and DC information related to target location and its allied phase. Due to random body movements, DC component may be significant compared to the AC signal which adversely affects the resolution during digitization. Frequency of the detected signal in an NIVSD system is generally between 0.1 Hz to 2 Hz in the baseband spectrum. This is in close proximity to the DC voltage. Hence, effect of DC offset is extremely significant in an NIVSD system. This DC offset can be effectively minimized with the help of a proper receiver architecture.

1.2.2.3 Null Point Detection

The performance of an NIVSD system is largely governed by the phenomenon of null point and optimal point. The sensitivity of the system is decreased when the detected signal is proportional to the second (or higher) order of the chest disarticulation signal instead of the *x(t)* itself. As a result, the fundamental component of chest wall disar-

ticulation is decreased and the overall sensitivity of the system is decreased. This is recognized as the null point problem in NIVSD. When the baseband signal is proportional to the sporadic chest movement, conceivable phase demodulation sensitivity is attained. This is the optimum point [35]. The adjacent null point and optimum point are always $\lambda/8$ distance apart from each other [26]. Fig. 1.3 depicts the concept of occurrence of a null point and the optimum point. The accurate detection of human vital sign is possible only with negligible null point effect. Due to its importance, a lot of efforts had been initiated by the researchers to overcome null point problem.

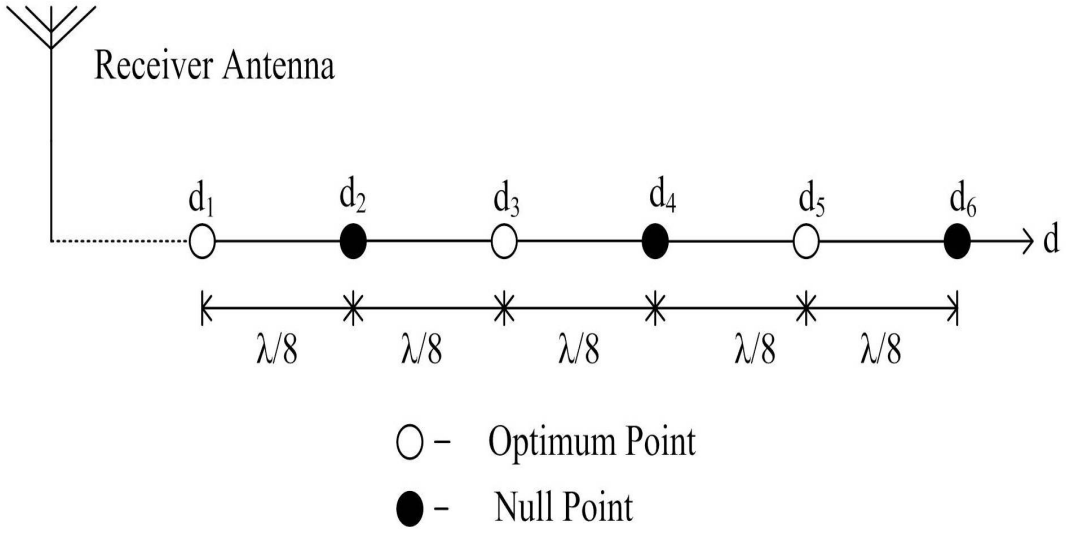

Figure 1.3: Illustration of optimum and null point.

1.2.2.4 Higher Order Harmonics

In general, the amplitude of respiration signal is greater than (even more than 10 times) the amplitude of heartbeat. Therefore, the baseband signal cannot be considered linear when displacement due to respiration is adequately large. As a consequence, dominant higher order harmonics will emerge in the region of the heartbeat frequency. The blocking effect of higher order harmonics decreases the accuracy of heartbeat detection.

1.2.2.5 Signal Processing

The radar signal processing aims at reduction in false alarm and improvement in SNR. For processing the baseband signal, in general, all NIVSDs use the simple fast Fourier transform (FFT) technique. Recently, wavelet transform (WT) [36–39] has also been used in the analysis of NIVSD. A comparative study between FFT and WT shows that WT is a better alternative for NIVSD analysis [40]. The RELAX algorithm, a parametric and cyclic improvement approach, least square method, method of correlation, maximum likelihood (ML) estimations, principal component analysis (PCA) based adaptive filter algorithm are also used to estimate respiration and heartbeat parameters [41–44].

Further, various other signal processing techniques for the extraction of human vital sign have been reported, such as Kalman filters, blind source separation, preservation of DC information, and fast clutter cancellation methods [45–48]. Recently, Chirp z-Transform (CZT) has been proposed as an option to FFT. It is a simplification of the z-Transform that achieves better resolution even without expanding the number of specimens [49]. Statistical signal processing and MIMO adaption can also be alternatives to the existing signal processing technique. From the available literature, it may be inferred that the NIVSD technology is matured enough on the signal processing front.

1.2.2.6 Number of Operational Band

For human vital sign detection, detection sensitivity and accuracy are the challenging issues. The existing technology for RF NIVSD system is based on the operation with a particular single band. These systems can either provide detection sensitivity or accuracy at the cost of each other. Hence, the operational band employed for detection is a key for successful deployment of such systems as a sensor.

1.3 Conclusions

This section of the thesis describes the motivation behind the present work. The need of a non-invasive sensor for human life detection is discussed. This is followed by the theory and working principle description for a human VSD RADAR. In addition, the technical issue, which can affect the detection accuracy is discussed. As a concluding remark, this section presents the basics of an NIVSD system and paves the way for design and development of a new non-invasive RF sensor for human vital sign detection.

Chapter 2

Preliminaries and Review

2.1 Introduction

The initial discussion in $Chapter 1$ paved the way for the design and development of an NIVSD sensor for human vital sign detection. Since the first time report in 1970s, contactless human vital sign detection system had drawn the attention of researchers and academicians due to its attractive features like non-invasiveness, low cost and ability to perform long term monitoring of human vital signs.

Notable overseas research groups like the 'Centre for Radio Frequency Electronics Research (CREER)' in Canada, 'Radio Frequency Circuits and Systems (RFCS)' research group in the University of Florida, 'Department of Electrical Engineering' at the University of Hawaii, 'Yonsei University' in Seoul, Korea and the 'WiPLi Laboratory' in the University of Udine, Italy carried out significant research towards the development of a human VSD Radar. In India, research groups at several premier technological institutes like Centre for Applied Research in Electronics (CARE), IIT Delhi, IIT Kanpur, IISc Bangalore and IIT Roorkee are engaged in the design and development of non-invasive RF sensor for a variety of day-to-day applications. IIT Bombay in Mumbai is also engaged in the study of biological effects of radiation on human body.

This chapter presents the state-of-the-art in the advancements in technology for the design and development of a non-invasive RF sensor for human vital sign detection. The chapter has been divided into two parts. First part describes topologies used for NIVSD applications, while the second part describes various measures reported in the literature for alleviating the challenges encountered during the NIVSD operation, as discussed in *Chapter 1.* Based on the available literature, research gaps have also been discussed in this chapter. Finally, the problem statement, objective and organization of the thesis are given.

2.2 The State-of-the art NIVSD Radar

The working principle of a non-invasive RF system for human vital sign detection is illustrated in Fig. 2.1.

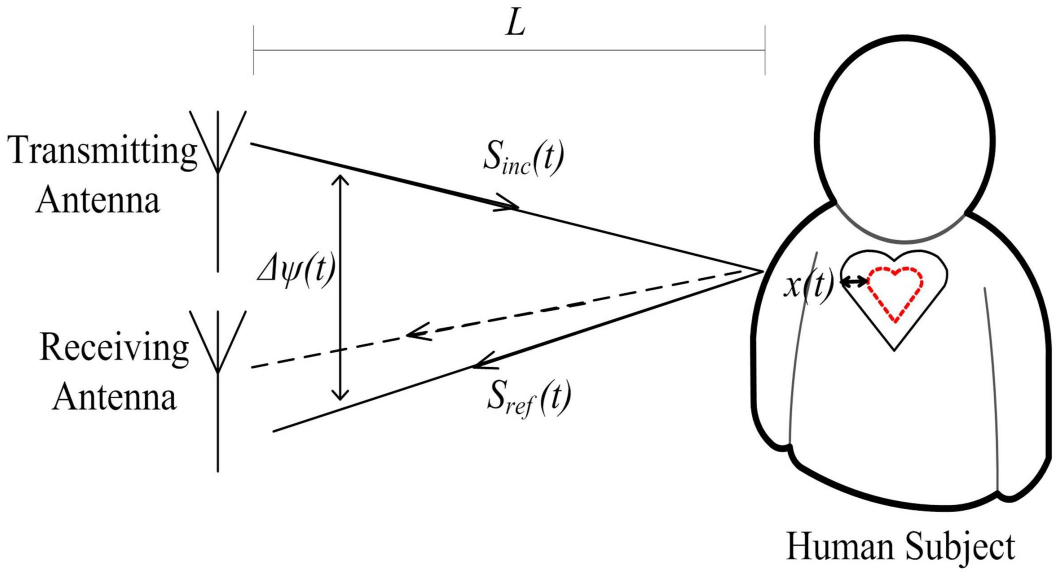

Figure 2.1: Working principle of a NIVSD RF sensor.

Here $S_{inc}(t)$ is the transmitted signal, $S_{ref}(t)$ is the received signal, ψ is the phase variation between $S_{inc}(t)$ and $S_{ref}(t)$, L is the distance between the RF system and the target, $\Delta\psi(t)$ is the total phase noise due to signal source and subsystems of trans-

mitter. Baseband signal $S_B(t)$ is obtained after demodulating the received signal. Let the transmitted signal $S_{inc}(t)$ is a sinusoidal wave with frequency *f*, then:

$$S_{inc}(t) = Cos[2\pi ft + \psi(t)] \tag{2.1}$$

Let a target (human body) is at a distance *L* from the transmitter and having a chest disarticulation *x(t)*. Then the total distance between the transmitter and the receiver is $2L(t) = 2L + 2x(t)$. According to [7], the received signal can subsequently be approximated as

$$S_{ref}(t) \cong Cos[2\pi ft - \frac{4\pi L}{\lambda} - \frac{4\pi x(t)}{\lambda} - \psi(t - \frac{2L}{c})] \tag{2.2}$$

where c is transmission velocity of the signal, λ is signal wavelength in air, $\psi[t - (2L/c)]$ is the phase noise contributed by the medium noise and the source.

From Eq. 2.2, it can be inferred that the received signal is analogous to the transmitted signal, except that it has a time lag equal to the sum of target distance and phase modulation due to the irregular movement of the target(human being). Information about the irregular chest movement can be retrieved by demodulating the received signal. The consequential baseband signal $S_B(t)$ obtained after demodulation is estimated as [7]

$$S_B(t) = Cos[\frac{4\pi L}{\lambda} + \frac{4\pi x(t)}{\lambda} + \Delta\psi(t) + \Phi] \tag{2.3}$$

$$\Delta\psi(t) = \psi(t) - \psi[t - \frac{2L}{c}] \tag{2.4}$$

where $[4\pi L/\lambda]$ is phase shift due to distance *L* of the target, Φ is a phase shift due to the surface reflection and delay caused in the subsystems, $\Delta\psi(t)$ is the residual phase noise.

It is intricate to devise a specific model to describe a human chest disarticulation. This is because the heart and lung endure complex movements inside the thorax. The disarticulation due to this results in amplitude and phase variation at different areas of the chest surface. In addition, the heartbeat and respiration rate for human being varies with age and other physiological conditions. However, from monitoring point of view,

it is sufficient to know whether the subject's heartbeat and respiration rate is normal or due to sporadic chest disarticulation. Owing to all these facts, the heartbeat and respiration can be symbolized as the sum of two sinusoidal waves with heartbeat and respiration rates as their respective frequencies. Then, the signals due to the respiration rate is approximated as

$$x_{resp}(t) = a_{resp}Cos(2\pi f_{resp}(t)) \tag{2.5}$$

where $x_{resp}(t)$ is the displacement of chest due to respiration, a_{resp} is the amplitude of the displacement of respiration and f_{resp} is the respiratory frequency. The signals due to the heartbeats is approximated as

$$x_{hb}(t) = a_{hb}Cos(2\pi f_{hb}(t)) \tag{2.6}$$

where $x_{hb}(t)$ is the chest displacement due to heartbeat, a_{hb} is the amplitude of the displacement of heartbeat and f_{hb} is the heartbeat frequency. The overall displacement due to the heartbeat and respiration is approximated as

$$x(t) = x_{resp}(t) + x_{hb}(t) \tag{2.7}$$

Equations 2.1 to 2.7 indicate that the NIVSD system measures only the disparity on the surface of the chest wall. As a result, the amplitude of the detected signals heavily depends on the physiological structure of the subject under test. Table 2.1 summarizes the parameters of the two vital sign signals of a human being with normal physique that are considered for analysis.

2.2.1 The radar Architecture

In case of invasive detection of human vital signs, the conventional electrodes are used, which not only gives a starchy feeling to the users but also suffers from need for periodic maintenance. In case of non-invasive detection of human vital sign, radios based on Doppler phase shift are used in which the microwave sensing systems transmit a radio frequency, single tone continuous-wave (CW) signal, which is reflected

Table 2.1: Summary of human vital sign [30]

Activity	Beats per Minute (BPM)	Frequency (Hz)
Respiration rate	$10 - 24$	$0.16 - 0.4$
Heartbeats	$60 - 90$	$1 - 1.5$

from the target and then demodulated in the receiver. Demodulation provides a signal corresponding to the human chest wall position that contains information about the movement due to heartbeat and respiration. This technique enables non-contact detection of vital signs of humans or animals from a distance, without any sensor physically attached to the body. The measurements may be carried out by using different Radar topologies. Fig. 2.2 represents the different Radar topologies involved in typical NIVSD applications.

2.2.1.1 CW Doppler Radar

In CW radar approach, the transmitted signal itself is used as the local oscillator signal in the down conversion process. Due to this, the baseband signal does not suffer from any frequency offset problem and the associated time delays. Hence, it directly eliminated the requirement of synchronizing mechanism. CW radar radio approach has drawn interest of the researchers primarily due to its simple architecture, low power requirement and clutter cancellation with proper front-end arrangement [48, 50]. A MIMO technique for detection of multiple movements and target tracking can be implemented with ease using CW radar. The front-end architectures for non-invasive detection of human vital sign include direct conversion or zero-IF receiver [51, 52], heterodyne radios [1, 53], double side band radios [35], direct IF sampling radio [54] and a self-injection locking architecture [55].

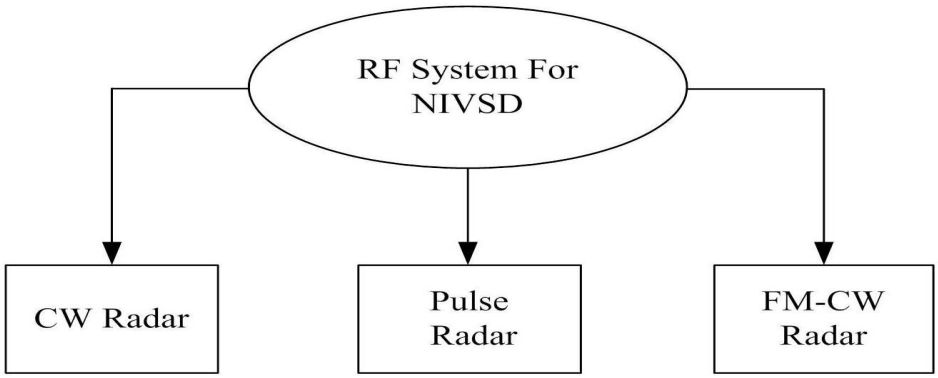

Figure 2.2: Radar classification.

2.2.1.2 UWB Radar

With UWB pulse radar, a very short electromagnetic pulse is transmitted towards the target. The topologies used to build a UWB pulse radar is described in [51, 56]. The principal advantage of UWB pulse radar is its ability to eliminate the multipath reflections and clutters. However, it suffers from the need for recalibrations when the distance between radio and object changes.

2.2.1.3 FMCW Radar

Recently, FMCW radar has been investigated and used in the human vital sign detection applications [57–60]. It transmits a chirp signal for a certain interval. The received ricochets are mixed with the transmitted chirp signal to produce the desired signal with the help of a low pass filter. In comparison to the traditional pulse radar, FMCW radars have better sensitivity, low power consumption and higher clutter rejection capacity.

2.2.1.4 Interferometric CW Radar

It employs CW Radars operating at different frequencies for human vital sign sensing applications. Particular Radars are selected by an RF switching mechanism, combined

together by a combiner. At the receiver side, an RF splitter is used to distinguish between the individual band signals. This topology enhances the target detection probability in a highly cluttered environment without increasing RF spectrum requirement by transition to a multicarrier interrogating signal [61].

2.2.1.5 On-chip Integrated Radar

Developments in the early 2000s have demonstrated the feasibility of integrating this function into modern wireless communication devices operating in *L* and *S* band [62]. The first integrated vital sign radar sensor chip using silicon CMOS has earlier been demonstrated in [63]. The chip integrates all the RF circuits, including a free running oscillator that provides the transmission signal and also servers as the reference [7].

2.2.2 Alleviation of Performance Issues

As discussed in *Chapter 1*, an NIVSD sensor for human vital sign detection suffers from various technical issues like clutters, DC offsets, Null point and higher-order harmonics. For effective detection of weak human vital signs, these issues must be addressed. Many efforts have been initiated to alleviate these issues. Based on the reported efforts, it may be concluded that the NIVSD system has reached to its maturity as a technology.

2.2.2.1 Clutter and Phase Noise

A microprocessor based clutter cancellation system was proposed by *Chen et al.* in [64]. In this approach, microprocessor reduces the direct component (DC) in the transmitted and received signal by regulating the phase delay and attenuation. The system generates an optimal signal (where the DC level of combined signal is minimum) to eliminate clutters from the surroundings. It also alleviates null point setback. The 1150 MHz microwave life detection system is shown in Fig. 2.3. The major draw-

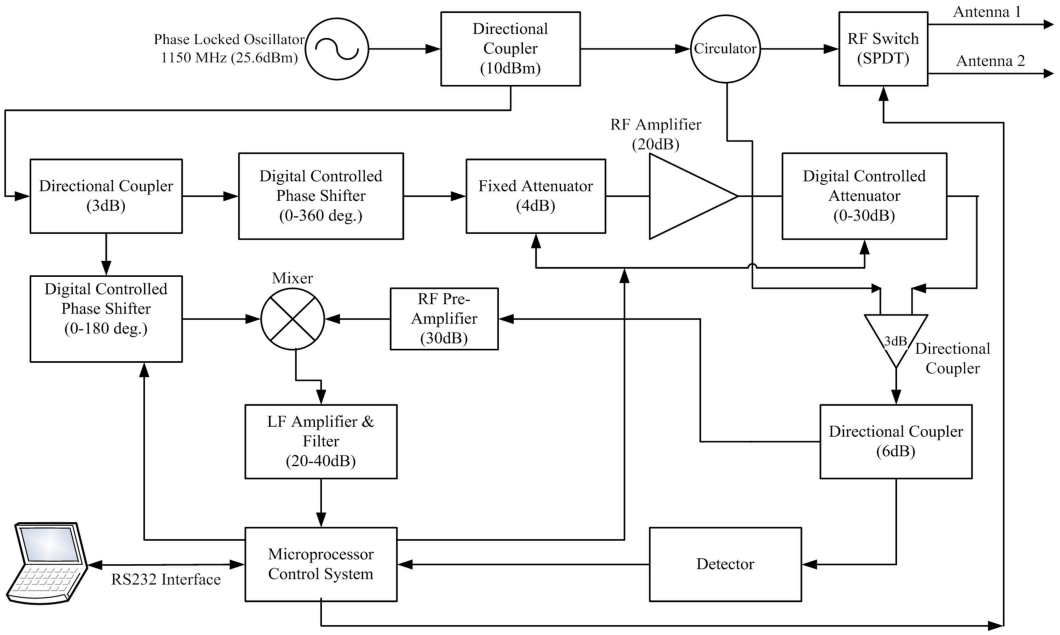

Figure 2.3: 1150 MHz microwave life detection system [64].

back of this system is its bulky hardware size and additional circuitry requirement. Multiple-input multiple-output (MIMO) technique was used to solve the problem of noise elimination due to random body movement [65]. The individual RF subsystems contribute noise in an NIVSD system. In [66], *Xiaogang Yu et al.* evaluated the detector subsystems individually and in collective to figure the overall noise performance of the detector. Following this, the authors carried out experiments for the analysis of trade off between output SNR and detection distance.

A 60 GHz millimeter wave life detection system (MLDS) was developed at National Cheng Kung University, Taiwan [67]. In this system, a clutter canceller is incorporated with an adjustable attenuator and phase shifter. It effectively reduces clutters from transmitting power leakage and background reflections up to a distance of 2 m. A synchronized motion technique (SMT) based on Doppler concept was reported by *Cheng et al.* of *National Taiwan University, Taipei- Taiwan* [49]. SMT was used to suppress the interference from the respiration in non-contact heartbeat detection. The experimentation proved that SMT effectively improved the heartbeat to respiration ra-

tio (HRR) up to 76% in subjects with normal breathing . Use of impulse ratio UWB radar along with a moving averaging filter has been proposed for suppressing clutter arising from random body movement [68]. Thus, all these efforts improved the performance of the existing NIVSD system by alleviating the effect of clutters.

2.2.2.2 DC Offset

DC offset can be effectively minimized with the help of indirect conversion receiver architecture shown in Fig. 2.4, arctangent demodulation in quadrature receivers and by double sideband indirect conversion radio architecture [69–71]. The cancellation of noise, caused by random walk of the human being and the DC offset problem in NIVSD were further improved by using a Doppler radar array approach.

A compensation algorithm was also introduced in [72] to diminish the disturbance of DC offset. An instrumentation Doppler radar system using laboratory equipment was proposed in [73]. In this approach, heterodyne digital quadrature demodulation architecture is used to mitigate the inequality in the quadrature channel and need of a complex DC offset calibration in arctangent demodulation. Fig.2.5 shows the block diagram of the instrumentation radar.

2.2.2.3 Null Point Detection

In low power ultra wide band (UWB) radar [74], the I/Q demodulator to acquire two baseband signals in quadrature [7] is an effective mechanism to eliminate the null point problem. Thus, UWB radar mechanism is free from the null point problem. However, a time discriminator with quick acting switches is solicited to select the preferred reflected pulses. With I/Q demodulator approach, at least one signal will be at an optimum point. This architecture is less complicated than that reported in [1]. However, this method suffers from the drawback of double baseband and signal processing part due to the use of separate I/Q channels.

By keeping double sideband waves at the transmitter output in quadrature [35], the

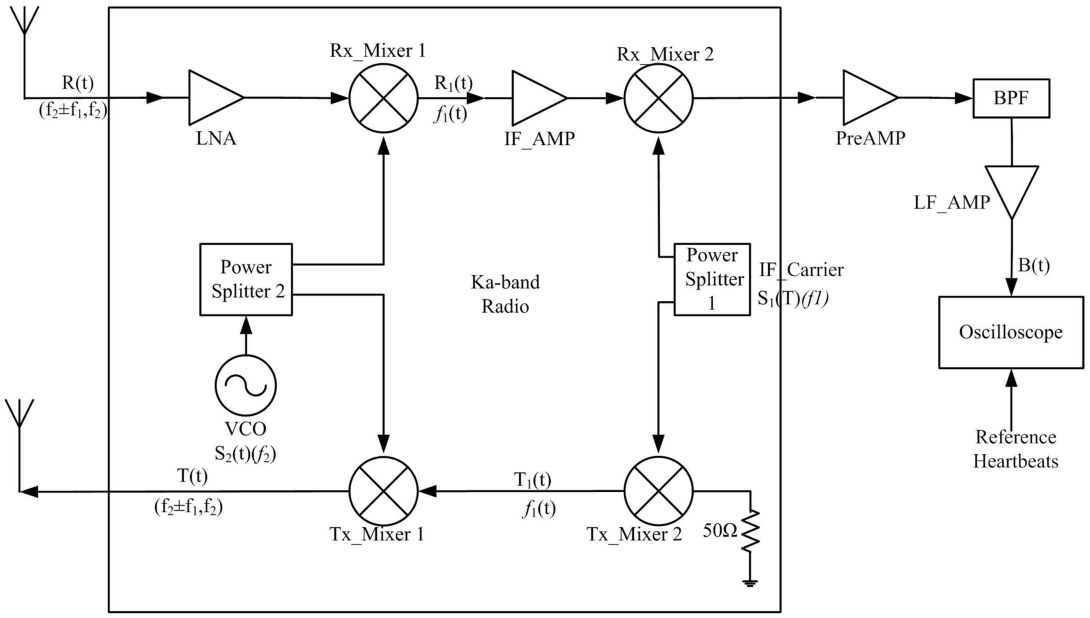

Figure 2.4: Ka-band transceiver for NIVSD [69].

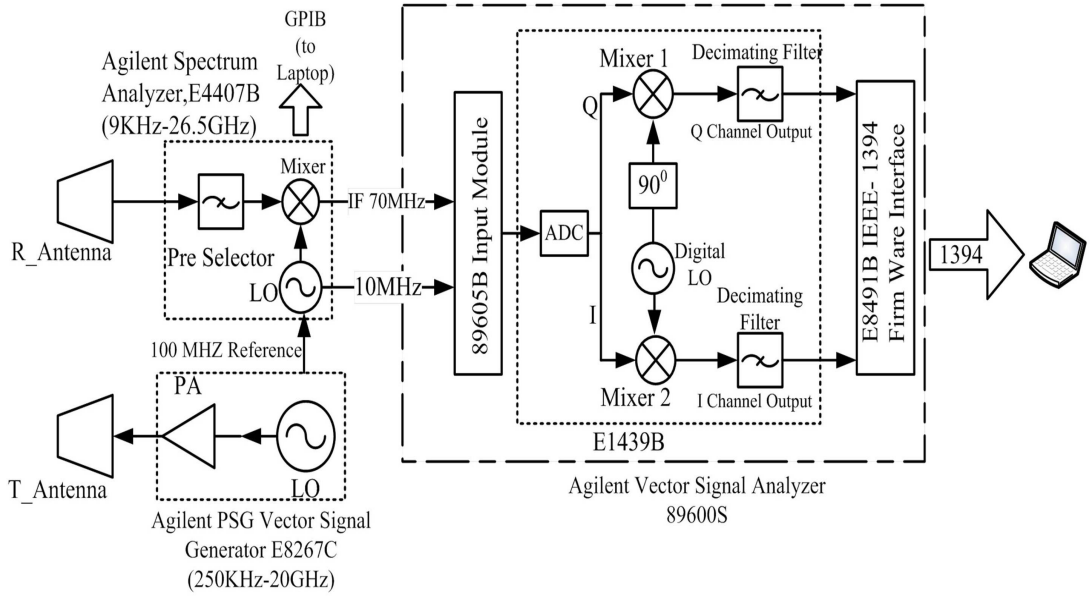

Figure 2.5: Block diagram of the instrument based radar system [73].

effect of null point can be minimized. Similar concept was analyzed to overcome the null point problem in [75]. Fig.2.6 shows the Ka-band transceiver for vital sign de-

tection from four sides of the human subject under test. Direct conversion quadrature architecture [71], ray tracing technique and spectrum analysis [76], Phase diversity and frequency diversity technique [77] that act as alternative approaches to I/Q demodulation [7] and double sideband transmission [35] are also used to overcome the null detection problem.

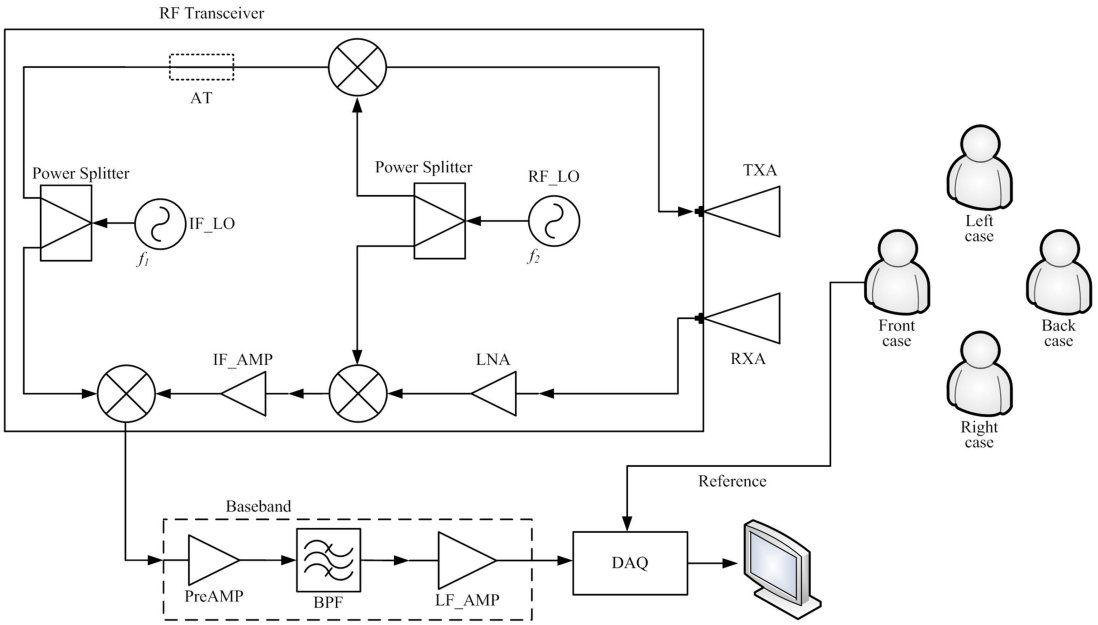

Figure 2.6: Ka-band transceiver for vital sign detection from four sides of the human subject [75].

2.2.2.4 Higher Order harmonics

Complex signal and arctangent demodulation [35] and tunable phase shifter direct conversion transceiver [71] may be used to minimize the effect due to random body movement. At high carrier frequencies, harmonics and intermodulation interference are eliminated with the help of arctangent demodulation. A comprehensive analysis of the combined effect of sensitivity, null points and DC-offset was carried out in [78]. A multi-frequency radar system [79] with signal correlation function provides a significant improvement in detection sensitivity of human VSD. The main drawback in

this approach is the need for a switching mechanism to toggle between the individual bands. The switching delay incorporates variation in the respiration and heartbeats over time. The methodology proposed in [79] may be a boon to the modernization of NIVSD system if these drawbacks are eliminated.

2.3 Research Gaps In The Existing NIVSD Systems

An NIVSD system must be able to sense very minute physiological disarticulation in millimeter or centimeter range. Hence, existence of arbitrary body disarticulation and different physical conditions can considerably affect detection sensitivity of NIVSD system. Also, for people having a wider chest disarticulation due to gasp, system supporting lower frequency is superior and vice-versa.

From the available literature and reported systems, it is observed that the NIVSD system operates with a particular single band. With such systems, detection sensitivity and minimum noise content can be attained at the cost of each other. The challenging issue in front of the existing single band NIVSD system is to bridge the trade-off between the sensitivity and the noise in the detected baseband signal. Hence, a new methodology is necessary to minimize this trade-off thereby improving the performance of the existing NIVSD systems.

Performance of the existing single band NIVSD systems can be improved by using multiband operation. Higher frequency allows signal detection even with very minute variations but at the cost of increased noise whereas lower frequencies minimize noise but with decreased detection sensitivity. Multiband systems can reap the advantage of increased detection sensitivity with lower noise interference. A multiband architecture can be achieved by parallel, switchable or concurrent arrangement of transceiver building blocks. Use of parallel system architecture for concurrent operation at individual frequency band is less attractive due to the requirements for high power consumption, large hardware and bulky nature. Detection from either side of the human body by two

separate transceivers is unappealing due to its hardware requirements [76]. A switched mode multiband system has a drawback of inconsistent measurement conditions for the same human subject due to switching delay [79]. Further, multifrequency interferometric radar [61] is used for this purpose where selection of frequency is incorporated by means of an RF switch. Similar methodologies were proposed in [80, 81] for random body moment cancellation so as to achieve fair detection of the required signals . However, all these schemes are not commercially viable due to one or more reasons like the requirement of a large hardware, high power consumption, and complex radio architecture. A brief summary of the state-of-the-art of the non-invasive human vital sign detection system is given in Table 2.2. The current trend in the area of Microwave / Millimeter wave integrated circuit research is to reduce system losses, increase compactness and reduce the power consumption level so that the RF systems can be used as a portable handheld device. A concurrent multiband system, based on hardware sharing, fulfils all above criteria. Fig. 2.7 shows the conceptual diagram of a dualband RF system for non-invasive human vital sign detection.

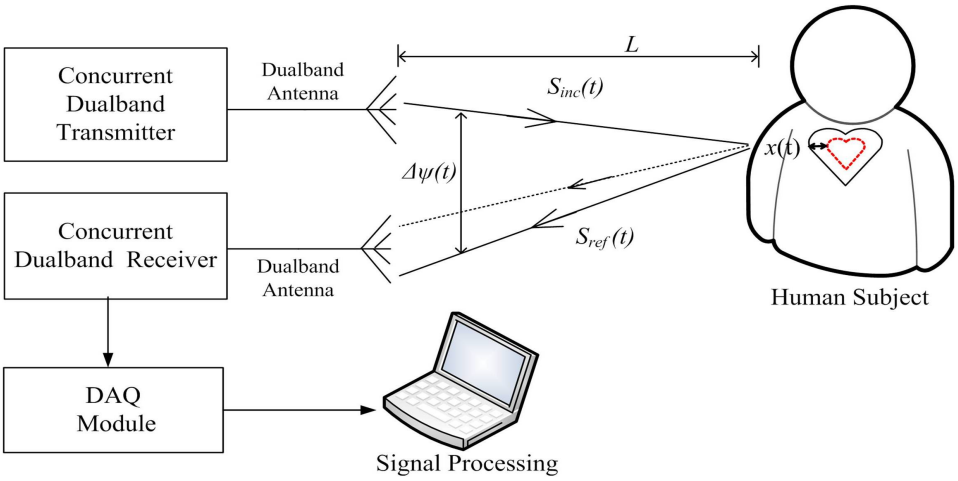

Figure 2.7: Working principle of the proposed NIVSD sensor.

Table 2.2: The State-of-the-art NIVSD System as a Sensor

Contribution	**Number of Operational band**	**Concurrent Operation**	**Size**	**Subsystem Design**	**Baseband Signal Processing**
J.C.Lin [1]	Single band	Not Reported	Bulky	Commercial devices are used	Radio meter output is used
Droitcour et.al. [62]	Single band	Not Reported	Bulky	Custom ICs and devices are used	—
K.Chen et. al. [64]	Single band	Not Reported	Bulky	Commercial devices & subsystems are used	FFT
C. Gu et. al. [73]	Dual band	Switchable operation by separate antenna for each band.	Bulky	Commercial devices are used	FFT
Chioukh et. al. [79]	Three independent band	Non-Concurrent, Individual Single-band RF Systems	Bulky	Commercial devices / subsystems are used	FFT
Proposed System	Dual band	Concurrent operation at $2.44\ GHz$ and $5.25\ GHz$ band	Compact	Indigenously designed concurrent dual-band subsystem	FFT / WT

2.4 Problem Statement

This thesis aims to design and develop of a concurrent dualband RF sensor system operating simultaneously at 2.44 GHz and 5.25 GHz frequency bands for non-invasive human vital sign detection. The implementation of the proposed sensor system requires design and characterization of concurrent dualband subsystems such as patch antenna array, low noise amplifier, Wilkinson power divider / combiner and oscillators. An efficient signal processing algorithm for accurate detection of human vital signs is also required. Application of the proposed system as an occupancy sensor can be verified by estimating the direction of arrival (DoA) so that the position of the human being can be confirmed.

2.5 Thesis Organization

Chapter 1 deals with the basic concept and theory of NIVSD system. The requirements and importance of an NIVSD system has been emphasized in detail along with its performance related issues. The chapter concludes with our motivation for carrying out the proposed thesis work.

Chapter 2 presents a literature survey on the sate-of-the-art of the proposed RF sensor system. The challenges and limitations in the design and implementation of RF sensor system for NIVSD applications are discussed. The literature review provides a pathway to arrive at a conclusion that there is a need for significant improvement in the present day technology for non-invasive detection of human vital signs.

Chapter 3 describes the design and characterization of radiating element used in the proposed NIVSD sensor. The gain and directivity are the two prime factors governing the selection of a particular antenna. Additionally, low cost, lightweight and ease in reproduction are considered as the design goals before initiating the design. Out of the several antenna structures available in the literature, a low cost concurrent dualband microstrip patch antenna array structures have been developed to operate simultane-

ously at 2.44 GHz and 5.25 GHz for the proposed sensor.

Chapter 4 of the thesis describes the design and characterization of the RF front end subsystems of the proposed sensor. As a part of the front end, two oscillators have been developed to operate at 2.44 GHz and 5.25 GHz. Further, a concurrent dualband Wilkinson power divider / combiner and an LNA which simultaneously operates at 2.44 GHz and 5.25 GHz frequency band have been designed, fabricated and characterized using Hybrid MIC technology.

Chapter 5 describes the characterization of the concurrent dualband NIVSD sensor for human vital sign detection. A unified concurrent dualband sensor system is developed using the subsystems described in *Chapter 3 and 4*. The signal processing method applied to the baseband signals to extract the desired respiration rate and heartbeat signal is discussed therein. Safety considerations, link budget and link margin analysis are also carried out in support of the proposed sensor.

Chapter 6 describes the application of the concurrent dualband sensor as an occupancy and position sensor. The detection and location of a human being inside a room is carried out with the help of the proposed sensor. The concurrent dualband operation for deciding the occupancy reduces the dead spots and false alarm in the detection process. It is found that the proposed mechanism works best upto a distance of 2 m. Further, the location of a human being is ascertained by his / her estimating the direction of arrival.

Chapter 7 concludes the thesis with a discussion on the capacity of the proposed concurrent dualband RF sensor for non-invasive human vital sign detection. Also, the future scope of the proposed work has been discussed therein.

2.6 Conclusions

In this chapter,a brief discussion on the state-of-the-art NIVSD system as an RF sensor for human VSD has been presented.The chapter begins with a review on the existing

technology for NIVSD sensor system and ended with a theoretical background for the proposed work. Problem statement and organization of the thesis is also discussed herein.

Chapter 3

Design and Characterization of The Radiating Elements

3.1 Introduction

Antenna is a device acting as a transition element between RF front end circuitry and free space. The advancement in the wireless applications and allied consumer services demonstrates the need for a low cost, compact and reliable antenna. There are many types of antennas, e.g. dipole antenna, monopole antenna, patch antenna, reflector antenna and horn antenna which are available for use in commercial as well as other specific applications. The idea of a microstrip antenna was first proposed by G. Deschamps in 1953 [82]. Since then, a large amount of research has been carried out by the researchers and academicians in search of an attractive solution in developing compact, conformal and low cost antenna for wireless applications. This chapter describes the design and characterization of a concurrent dualband microstrip patch antenna to fulfill there requirements such as low cost, light weight and reproducibility for use in NIVSD sensor applications.

3.1.1 Theory of Microstrip Antennas

The microstrip patch antenna consists of a radiating patch on one side of a dielectric substrate and a ground plane on the other side as shown in Fig. 3.1. Here, t is the thickness of the patch, L and W are the length and width of the patch respectively, and h is the height of the substrate. The patch is generally rectangular, circular, triangular or elliptical in nature. The radiation pattern of the antenna depends on the surface current distribution of the radiating patch and the feed structure. The impedance matching of the antenna is also sensitive to the feed structure. A variety of mechanisms such as waveguide feed, a microstrip line feed, coplanar waveguide feed, proximity coupling feed and aperture coupling feed have been reported in the literature [83, 84].

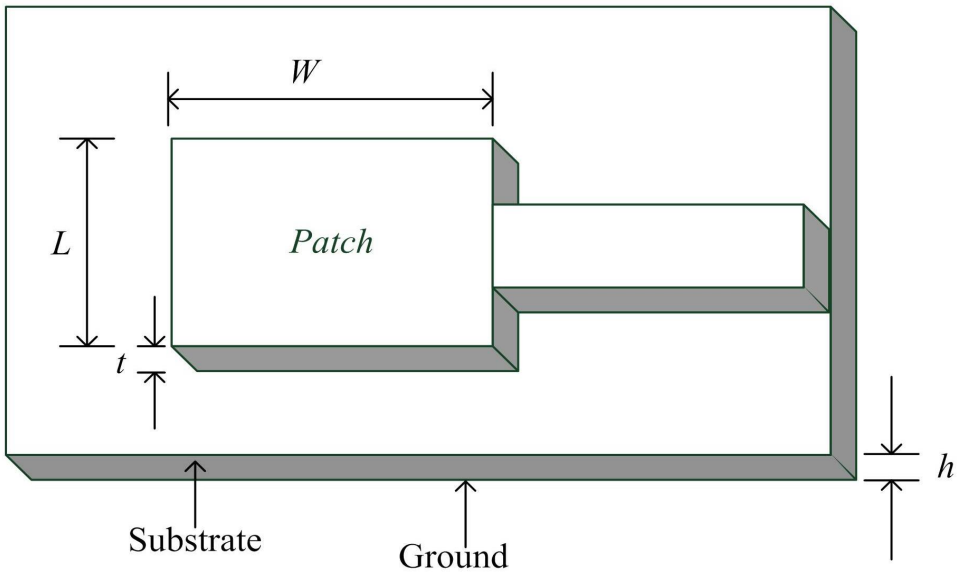

Figure 3.1: A microstrip patch structure.

A variety of substrates can be used in the design of a microstrip antenna with a dielectric constant in the range of $2.2 \leq \varepsilon_r \leq 12$. Substrates whose dielectric constants are at the lower end of this range are mostly prepared as they provide better efficiency and larger bandwidth. The design procedure of a microstrip antenna may be summarized

as followes [83] For efficient radiation, the width W is given by:

$$W = \frac{c}{2f_0\sqrt{\frac{\varepsilon_r}{2}}} \tag{3.1}$$

where, ε_r is the dielectric constant of the substrate, h is the height of dielectric substrate and W is the width of the patch. For F_0 = 2.44 GHz and ε_r = 3.2, this yields W = 42.39 mm. The the value of ε_{reff} for micro-stripline is computed for substrate height h = 0.1524 cm using the following relation.

$$\varepsilon_{reff} = \frac{(\varepsilon_r + 1)}{2}\frac{(\varepsilon_r - 1)}{2}\sqrt{(1 + 12\frac{h}{W})} \tag{3.2}$$

It is found that ε_{reff} is 2.6746. The fringe factor ΔL is calculated as

$$\Delta L = 0.412h\frac{(\varepsilon_{reff} + 0.3)(\frac{W}{h} + 0.264)}{(\varepsilon_{reff} - 0.258)(\frac{W}{h} + 0.8)} \tag{3.3}$$

The fringe factor ΔL in our design turns out to be 0.075 cm. Finally, the length of the substrate L is calculated.

$$L = L_{eff} - 2\Delta L \tag{3.4}$$

Where L_{eff} is the effective length of the patch antenna and expressed for a given resonance frequency as:

$$L_{eff} = \frac{c}{2f_0\sqrt{\varepsilon_{reff}}} \tag{3.5}$$

The length of the microstripline patch is determined to be 36.08 mm. The length and width of the patch are further optimized to obtain the desired results and is discussed in *Section 3.2.1.2*. For NIVSD system, a low power, compact and light weight antenna is desired. In addition to this, it should be very easy in fabrication with a high reproducibility. In this context, a concurrent dualband microstrip patch antenna array is designed and used in the experimentation. The reason behind the particular choice is the extra gain achievement from an array structure. The designed antenna operates simultaneously at 2.44 GHz and 5.25 GHz frequency band. The patch antenna array is designed, fabricated and characterized to have omni-directional and directional

radiation pattern for use in the proposed sensor. Furthermore, the antenna structure reported in [85] is modified and experimentally characterized so as to use it during experimentation.

One of the major factor which differentiate an antenna from other is its radiation pattern. Hypothetically, it is assumed that the isotropic antenna radiates equally in all the direction. On the other hand, an omni-directional antenna is having a non directional pattern in azimuth and a directional pattern along the direction of elevation. In contrast, a directional antenna is one, which has its radiation pattern concentrated in some specific direction only. It inherently acts as a filter for the directions other than it is intended for. The E-plane pattern is defined as the radiation pattern in a plane having the electric field vector and the direction of maximum radiation. The H-plane pattern is the radiation pattern in the plane containing the magnetic field vector and the direction of maximum radiation.

3.2 Characterization of The Concurrent Dualband Patch Antenna

For the purpose of experimentation, the concurrent dualband antenna reported in [85] is modified and optimized for a substrate of relative dielectric constant (ε_r) of 3.2. For array design, an omni-directional and a directional patch antennae have been designed and characterized. The initial patch dimensions are calculated for operation at lower frequency band and subsequently optimization has been carried out to obtain radiation in both the frequency bands. The design of the proposed antennas are simulated and verified with a computer simulation technology *(CST-2012)* platform by considering a hexahedral mesh element with 20 lines per lambda. The simulated antennae are then fabricated on a commercial *NH9320* substrate, which is a poly-tetra-fluoro -ethylene (PTFE) / glass / ceramic dielectric. It has a relative dielectric constant (ε_r) = 3.2, height (h) = 1.524 mm, thickness (t) = 18 μm and a loss tangent $(\delta) = 0.0024$. Wet

etching technique has been used in the fabrication process. The design and characterization details has are described in the following sections.

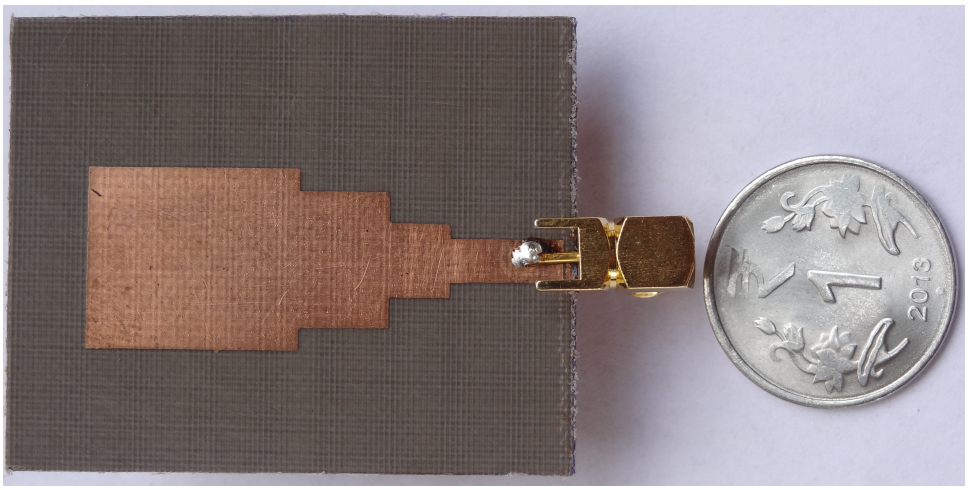

(a)

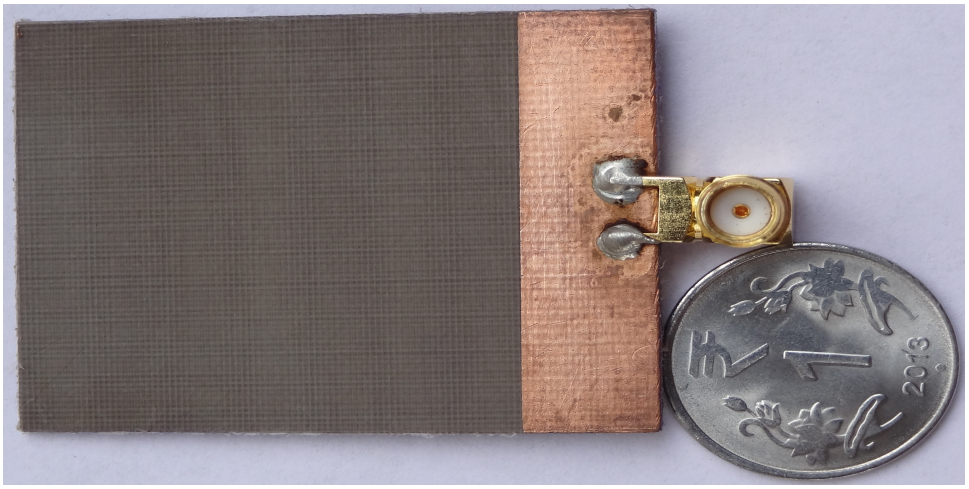

(b)

Figure 3.2: Fabricated prototype of a concurrent dualband patch antenna : (a) Patch Side (b) Ground Side [85].

3.2.1 The Directional 1×2 Patch Antenna Array

3.2.1.1 The Background

In the past, development of dualband antennae was initiated in a large extent [86–92]. Nearly all these antennae are designed for wireless applications with omni-directive radiation pattern. A non-contact vital sign detection centric approach was proposed in [93, 94]. However, these activities end with a broadband performance. Efforts were initiated by the researchers to develop a directional array antenna using planar technology. Such radiation pattern is very useful in healthcare, military and disaster management applications where the existence of a human being is to be confirmed. A 1×2 and a 1×4 antenna array were presented in [95] for operation at 3.5 GHz and 5 GHz band with separate aperture feeding. A four-element single band rectangular microstrip patch antenna for 2.4 GHz application was described in [96]. A single band slotted 2×2 microstrip patch antenna array for 5.25 GHz band was reported in [97]. A double L-slot patch antenna array was presented in [98] wherein two separate CPW feed points were used to feed the array element and with an omni-directive radiation pattern.

Owing to all these facts, a 1×2 patch antenna array is proposed in this thesis. The antenna is characterized with a simple feed geometry and use of the complementary split ring resonator (CSRR) in the ground plane. The design goals of the proposed antenna for human vital sign detection are: dimensions of the antenna should not be more than 4×4 $inch^2$, concurrent dualband operation at 2.44 GHz and 5.25 GHz range, and directive radiation pattern. Table 3.1 summarizes a brief review of the microstrip antenna.

3.2.1.2 The Geometry

Geometry of the proposed antenna is shown in Fig. 3.3. The rectangular patch is designed using the empirical relations given in [83, 84] and a CSRR is used in the

Table 3.1: The state-of-the-art microstrip antenna array

Contribution	**Operation band (in GHz)**	**Feed Mechanism**	**Directivity**	**Nature of the array**
Swelam et. al. [95]	3.5 and 5	Separate aperture feed	Omnidirectional	1×2 and 1×4 patch elements
Khraisat et. al. [96]	2.4	Microstrip line	Directional	1×4 patch elements
Ghosh and Parui [97]	5.25	Microstrip line	Directional	2×2 slotted patch
J. Chitra [98]	Wideband (2.4 to 3.5 and 4 to 5.4)	Two separate CPW feed	Omnidirectional	Two separate patch with independent feeds
K. Lau et. al. [99]	Wideband (3.4 to 4.5)	Proximity coupled feed	Omnidirectional and Unidirectional at specific bands	sandwich of three dielectric layers
R.Li et.al. [100]	2.4 to 2.5 and 5.1 to 5.9	Coaxial cable feed	Directional	A long dipole and two short dipole elements
Present Work	2.44 and 5.25	Corporate feed	Directional	1×2 patch with CSRR loading in the ground

ground plane. The CSRR used in the antenna structure behaves like an electric dipole which can be excited by an axial electric field. The electrical equivalent of CSRR is an LC tank circuit [101]. The width of CSRR slot is 0.5 mm, and the gap G is equal to 0.5 mm. The radius of the outer concentric ring of CSRR is 3.5 mm and that of inner ring is 2 mm. Length of the patch (L_P) is 32.50 mm, and width (W_P) is 33.75 mm. A substrate of dimension $(L_S \times W_S)$ 78 $mm \times$ 97 mm is used. Both L_1 and L_2 are 10 mm. A corporate feed network is designed according to [102]. The feed width W is kept at 3.6 mm and the subsequent width is decreased accordingly. The height of feed from the substrate boundary (L_3) is 12 mm. W and W_1 are kept at 1.8 mm and 3.6 mm, respectively. The patch is placed at a horizontal distance (W_3) of 10 mm from the substrate. On the ground plane, both CSRR are kept at an equal height, i.e. G_L = 40 mm. GW_1 and GW_2 are kept at 41.50 mm and 36.50 mm, respectively.

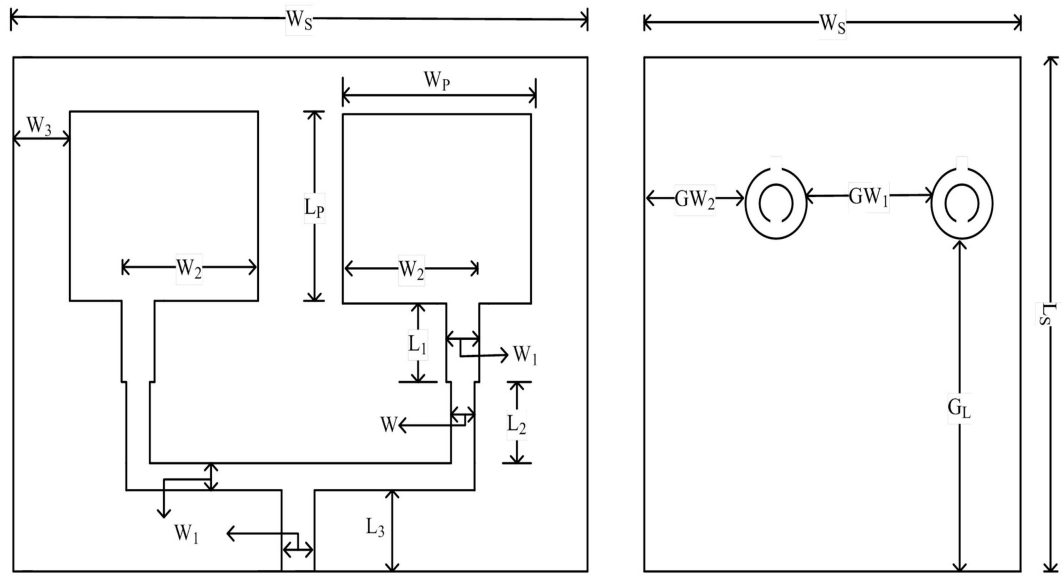

Figure 3.3: Geometry of the proposed concurrent dualband antenna.

3.2.1.3 The Parametric Study

To consolidate the functioning of the antenna, parametric studies of the effect of patch dimensions and CSRR position are carried out. Fig. 3.4 shows the parametric study of the effect of CSRR position while other dimensions are kept constant. The effects of the variation of patch dimensions are also examined. The lower frequency of the microstrip patch is sensitive to the variations in the width (W_P), while the higher frequency is sensitive to the variation in length (L_P). Also, the desired frequency bands are sensitive to variation in the CSRR position. Fig. 3.5 illustrates the parametric study of the patch dimensions. The simulated surface current at the desired bands is shown in Fig.3.6 which confirms the dualband nature of the proposed antenna. Fig. 3.7 shows the fabricated prototype of the proposed antenna.

3.2.1.4 Experimental Characterization and Discussions

The measurement setup for the proposed antenna is shown in Fig. 3.8. Fig. 3.9 shows the simulated and measured return loss characteristics of the designed antenna prototype. The result confirms the dualband characteristics of the proposed antenna. Due to slight deviation from the calculated parameter values and the errors during the fabrication process, some deviation is observed in the measured results. Another band is also present in simulation as well as in our measurement near 6 GHz. However, it may be neglected as the return loss is around -7 dB (maximum). The E-plane and H-plane radiation patterns have been measured in the anechoic chamber with the transmitting antenna, and the designed prototype (receiver) was distanced at 1.5 m.
Fig. 3.10 depicts the anechoic chamber measurement setup used in the characterization of the proposed antenna. Here, a wideband source operating between 10 MHz to 20 GHz *(R&S: SMR20)* has been used along with a wideband reference antenna *(ELMIKA: 1 GHz to 8 GHz)*. The source is operated at 2.44 GHz and 5.25 GHz frequencies with 15 dBm power output.

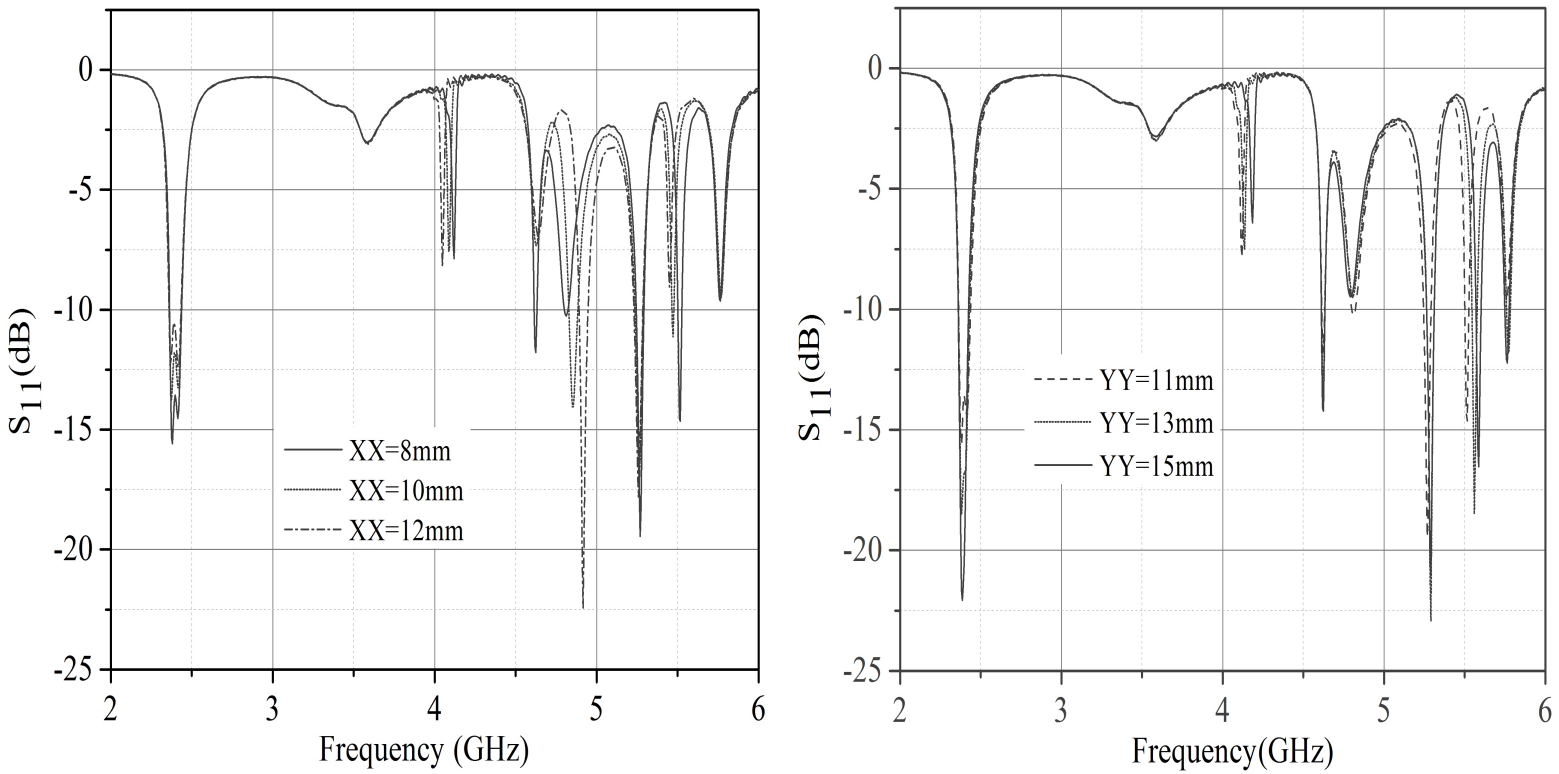

Figure 3.4: CSRR position parametric study : (a) XX = Horizontal position with YY = 11 mm, W_P = 33.75 mm, L_P = 32.50 mm (b) YY = Vertical position with XX = 8 mm, W_P = 33.75 mm, L_P = 32.50 mm.

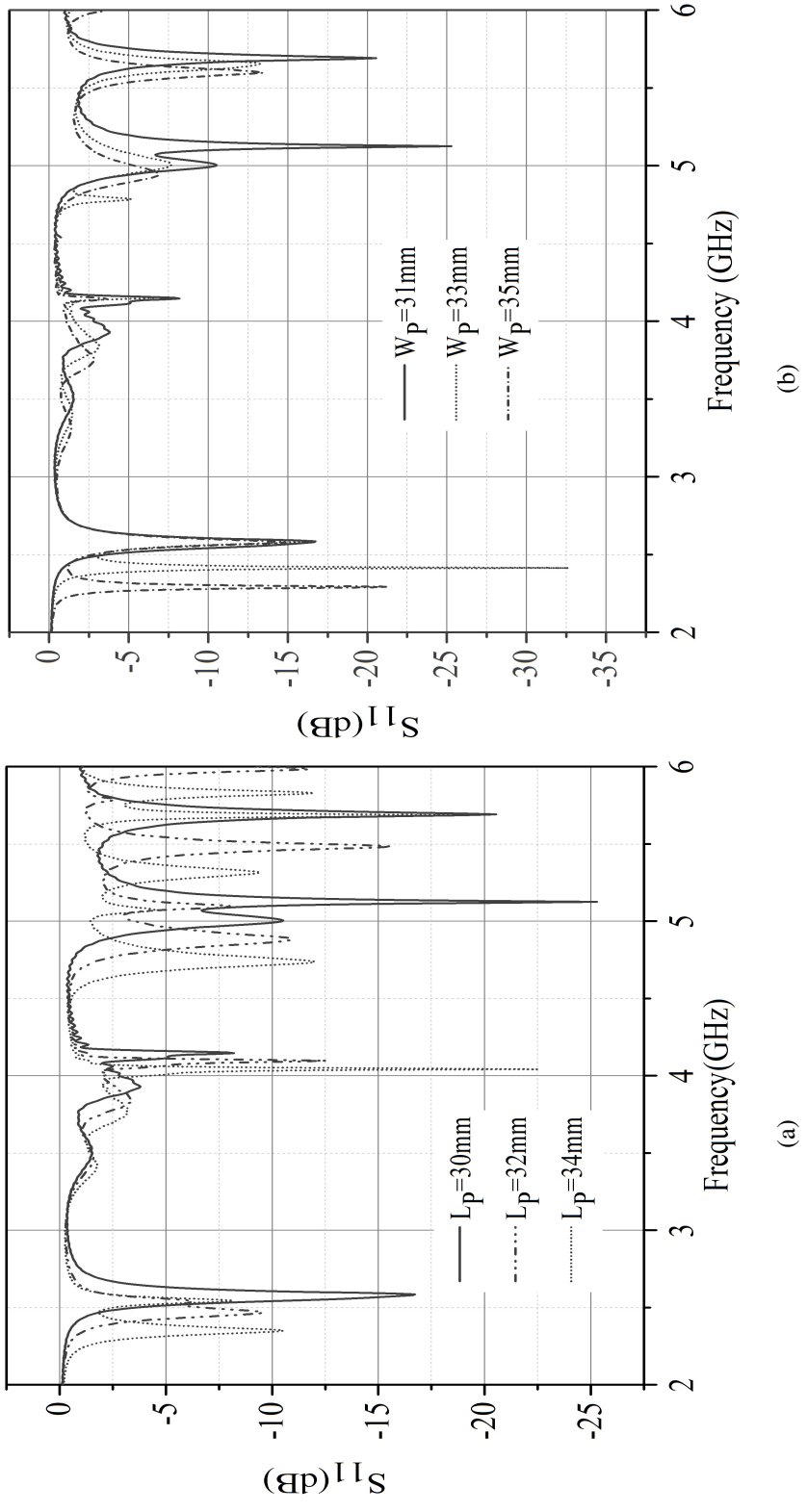

Figure 3.5: Patch dimension variation effect : (a) L_P = Patch length with W_P = 31 mm, XX = 10 mm, YY = 12 mm (b) W_P = Patch width with L_P = 32mm, XX = 10 mm, YY = 12 mm.

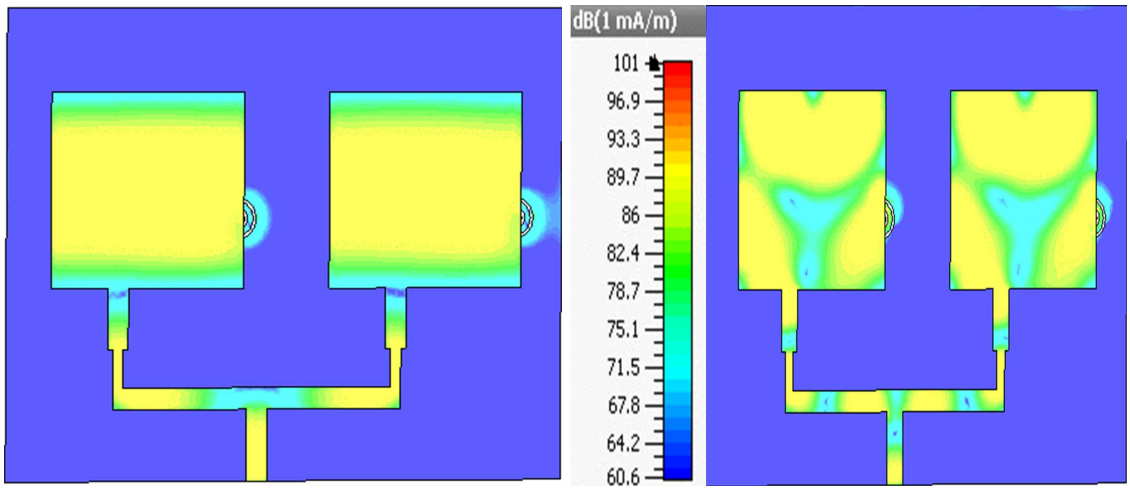

(a) (b)

Figure 3.6: Surface current distribution at : (a) 2.44 GHz and (b) 5.25 GHz.

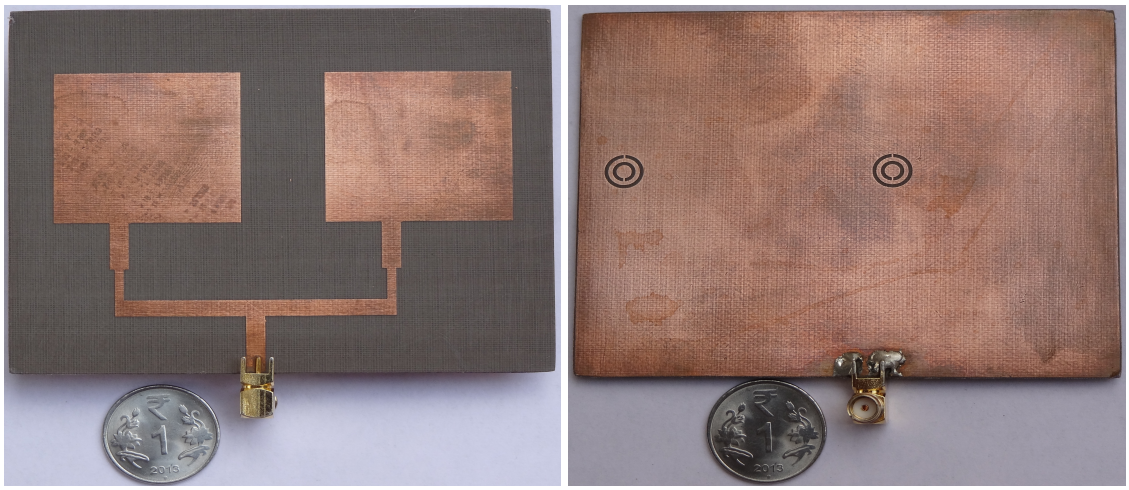

(a) (b)

Figure 3.7: Fabricated antenna prototype : (a) Patch side; (b) Ground side with L_P = 32.5 mm, W_P = 33.75 mm, XX = 1 mm, YY = 11.5 mm, L_S = 78 mm, W_S = 97 mm and L_1 = L_2 = 10 mm.

.

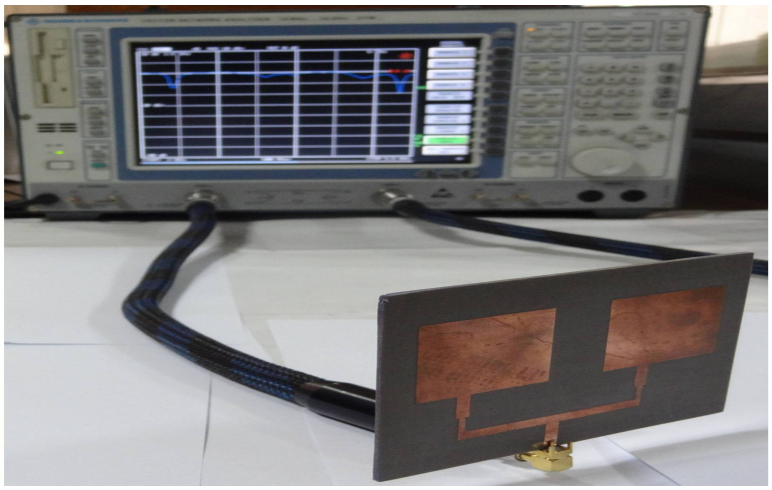

Figure 3.8: Measurement setup for antenna characterization.

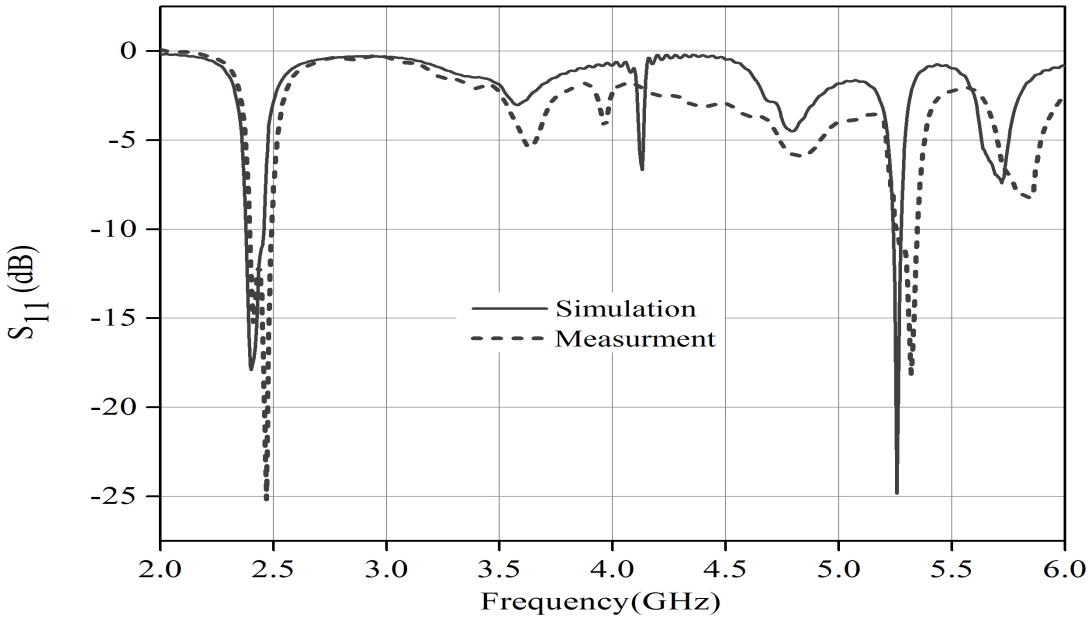

Figure 3.9: Return loss characteristics of the proposed antenna with L_P = 32.5 mm, W_P = 33.75 mm, XX = 1 mm, YY = 11.5 mm.

The antenna under test (AUT) is rotated in all directions (0^o to 360^o with a step size of 5^o) by the positioner to estimate the radiation pattern. The radiated power is measured and recorded using the power meter *(R&S NRVS1020)*. Fig. 3.12 depicts the 3D radiation pattern for the proposed antenna array. The comparisons of simulated and

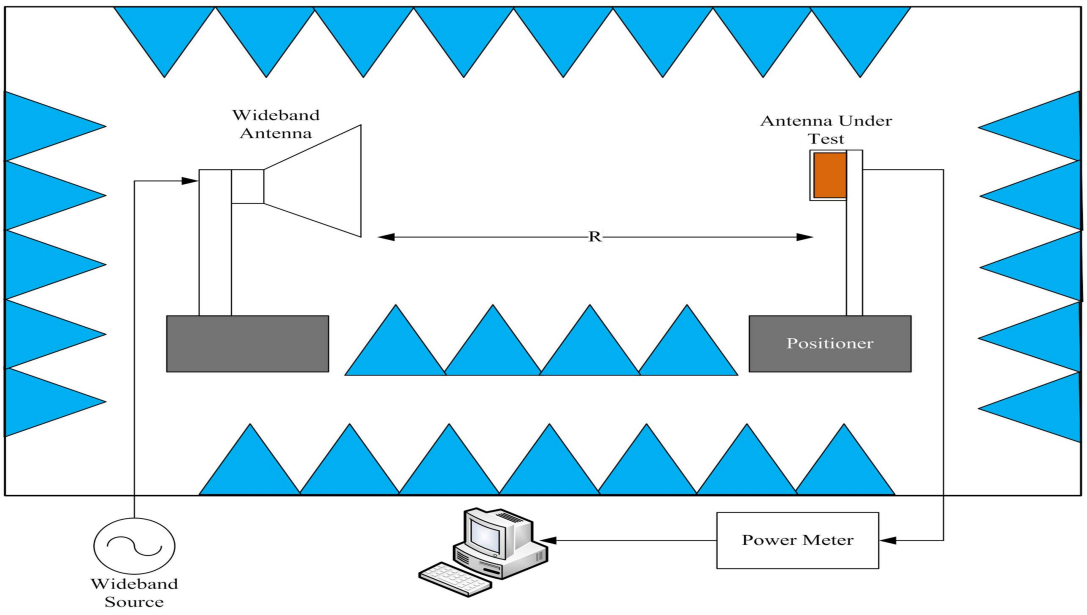

Figure 3.10: Anechoic chamber measurement setup.

the measured radiation pattern are illustrated in Fig. 3.13 and Fig. 3.14. These plots confirm the directive radiation properties of the antenna.

Measurement of gain has been carried out by the substitution method with a standard gain horn antenna (reference antenna) working in the range 900 MHz to 8 GHz. Table 3.2 summarizes the simulated and measured gain at 2.44 GHz and 5.25 GHz. A difference of average 1.2 dB in the simulated and measured gains has been observed, which may be attributed to the constraints in the fabrication process and measurement errors.

Table 3.2: Measured gain characteristics

Frequency (GHz)	Simulation Gain (dBi)	Measurement Gain (dBi)
2.44	8.577	7.21
5.25	9.302	8.12

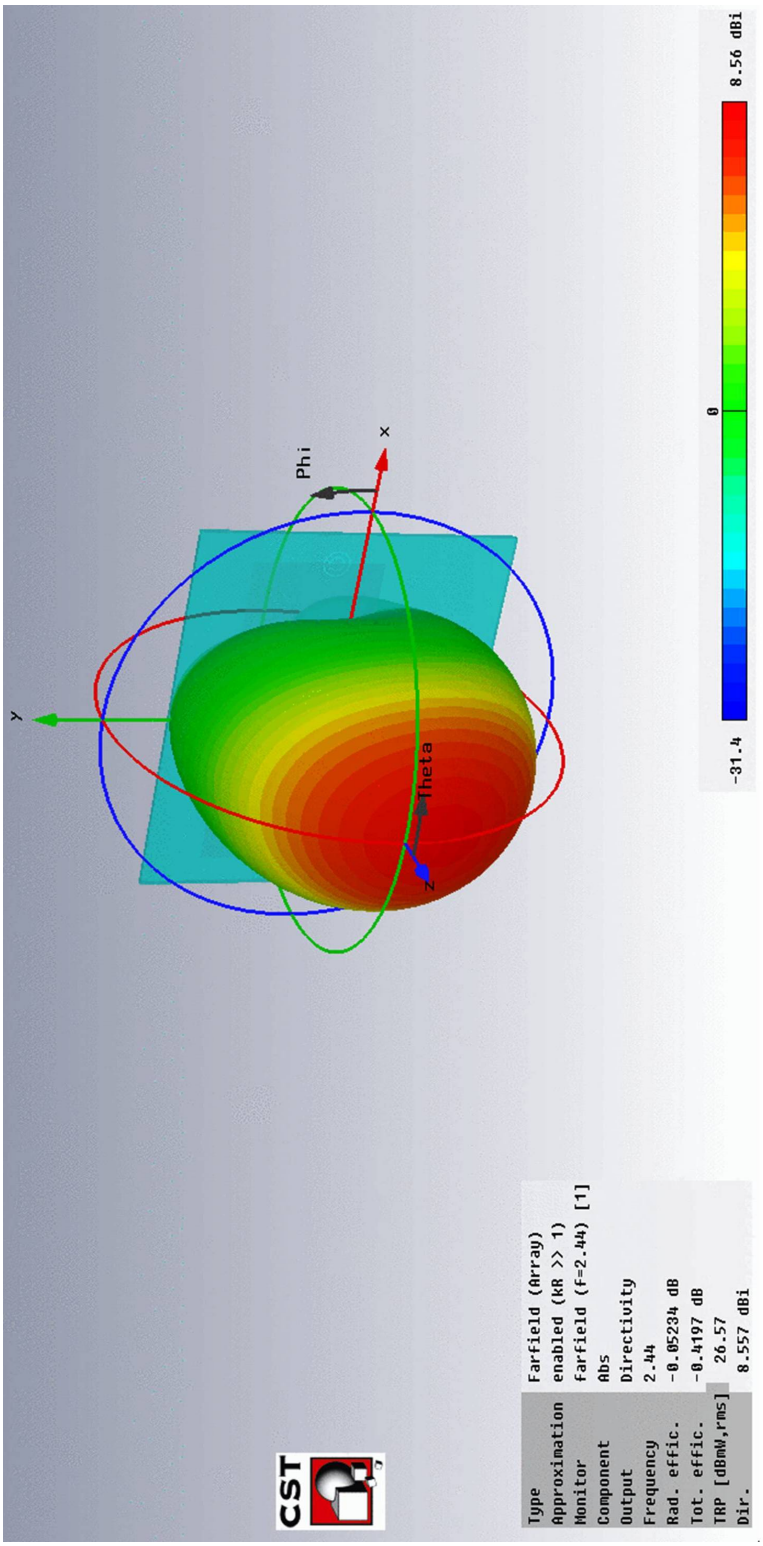

Figure 3.11: Simulated 3D radiation pattern at 2.44 GHz

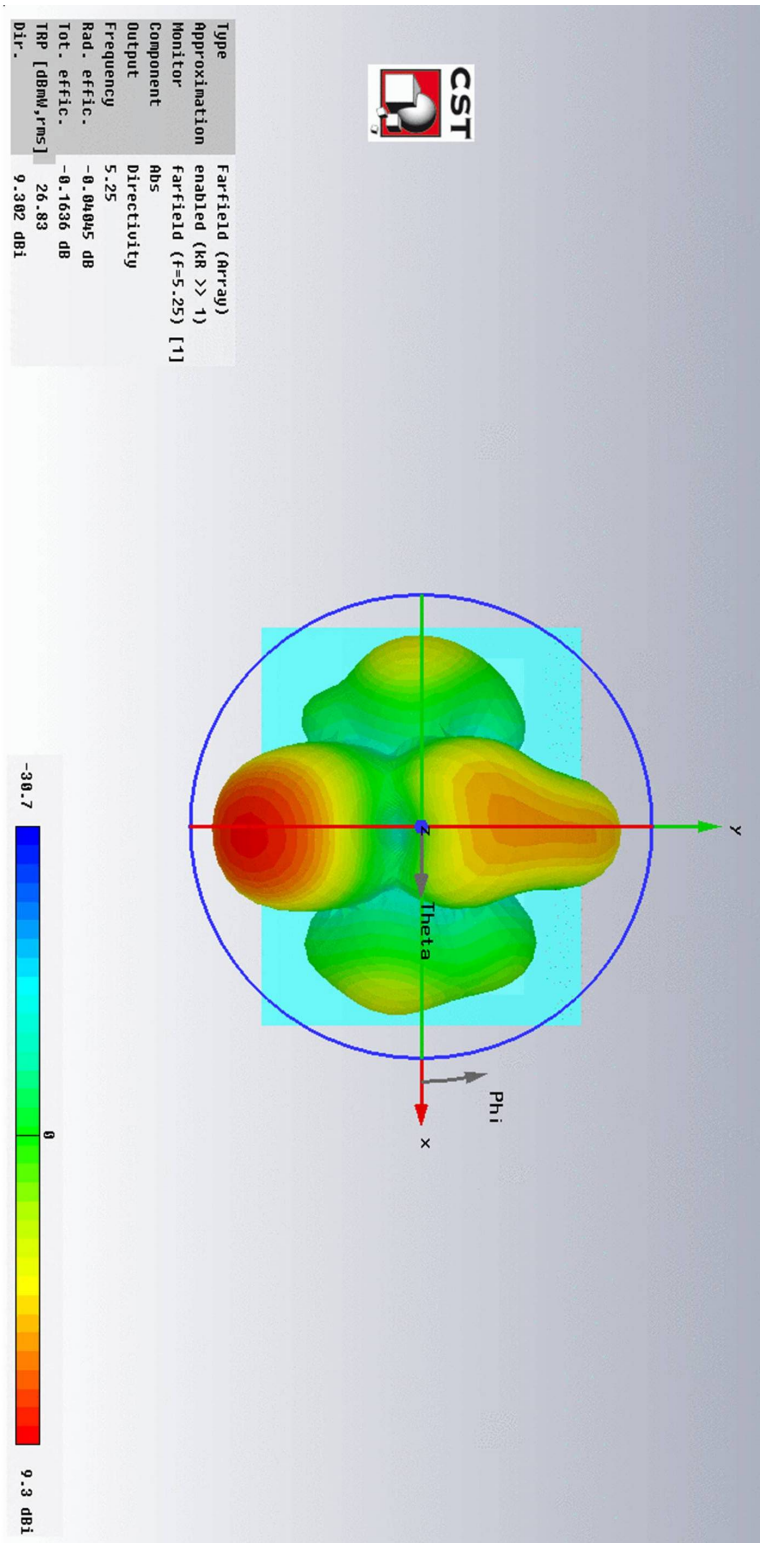

Figure 3.12: Simulated 3D radiation pattern at 5.25 GHz.

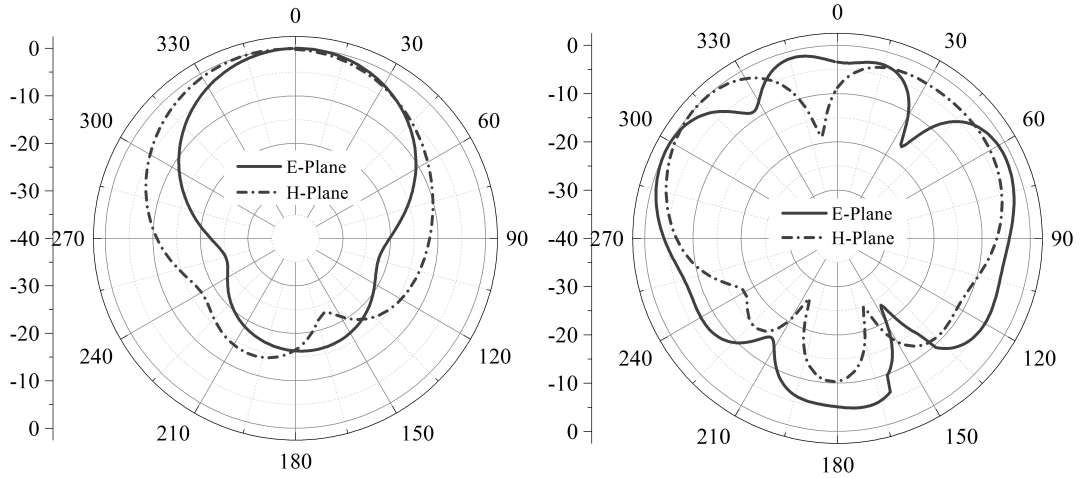

(a) (b)

Figure 3.13: Simulated radiation pattern of the directive patch antenna array at : (a) 2.44 GHz (b) 5.25 GHz

.

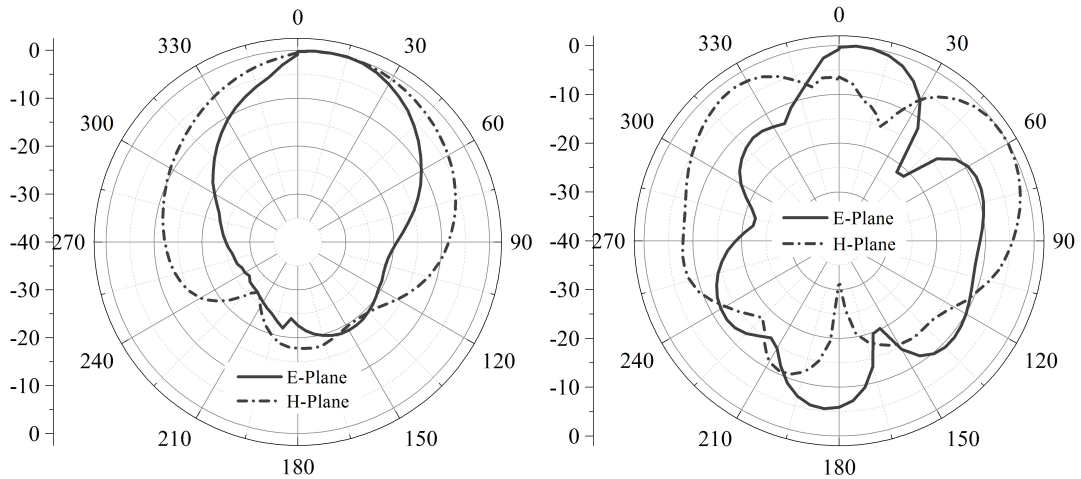

(a) (b)

Figure 3.14: Measured radiation pattern of the directive patch antenna array at : (a) 2.44 GHz (b) 5.25 GHz band.

3.2.2 The Omnidirectional 1×2 Patch Antenna Array

3.2.2.1 The Geometry

A 1×2 monopole concurrent dualband patch antenna array has been also designed and fabricated for the NIVSD analysis. The array is a combination of two identical microstrip patch fed by a single feed line. Individual patch of the designed dualband monopole antenna consists of two rectangular elements that are piled over each other. Fig. 3.15 depicts the geometry of the proposed antenna array. The smaller rectangular monopole element governs the higher frequency operation of the antenna. It has a width of 11.2 mm and length 7.1 mm. The larger rectangular monopole element controls the lower frequency operation of the antenna which is 15 mm in width and 18.5 mm in length. An additional rectangular monopole element is positioned exactly below the higher frequency monopole element having a width of 6 mm and length 5 mm along with an extra small metallic strip with width 3.5 mm and length 10 mm. This arrangement is intended to get better return loss at both frequencies of interest. Rectangular monopole elements are printed on one side of the *NH9320* substrate. The overall length and width of the substrate is 60 mm and 79 mm, respectively. The ground plane is kept on the other side of substrate with length 29.4 mm and width 79 mm. The bandwidth and operating frequency is sensitive to the ground plane dimensions. A simple corporate feed network is designed according to [102] for the proposed array antenna. It has a length of 6.3 mm and width of 38.2 mm.

3.2.2.2 The characterization

The fabricated antenna prototype is as depicted in Fig. 3.16. Fig. 3.17 indicates the simulated and measured return loss characteristics for the antenna. Mismatch in response is due to limitations of the fabrication process.

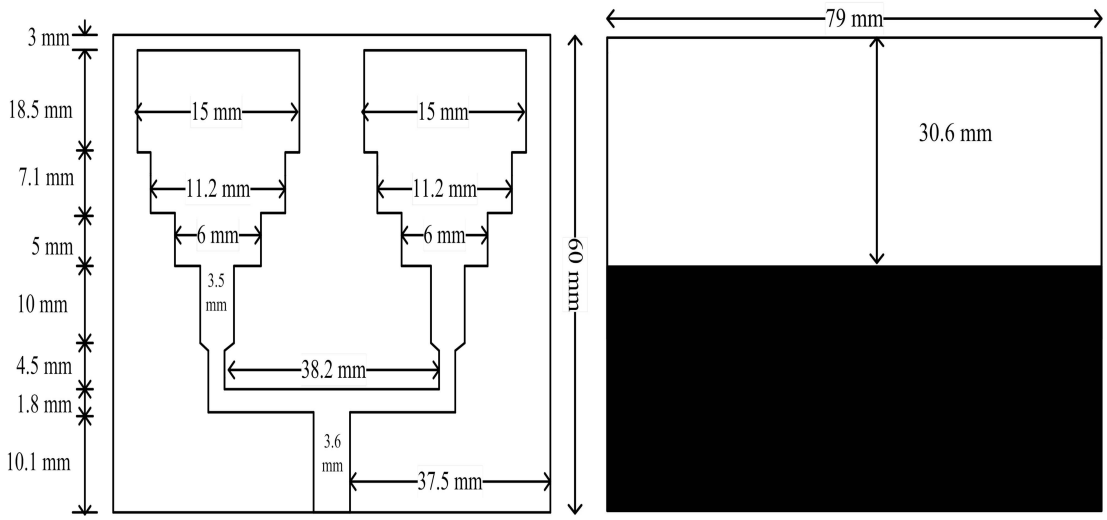

(a) (b)

Figure 3.15: Geometry of the proposed 1×2 dualband omnidirectional antenna array : (a) Patch side (b) Ground side.

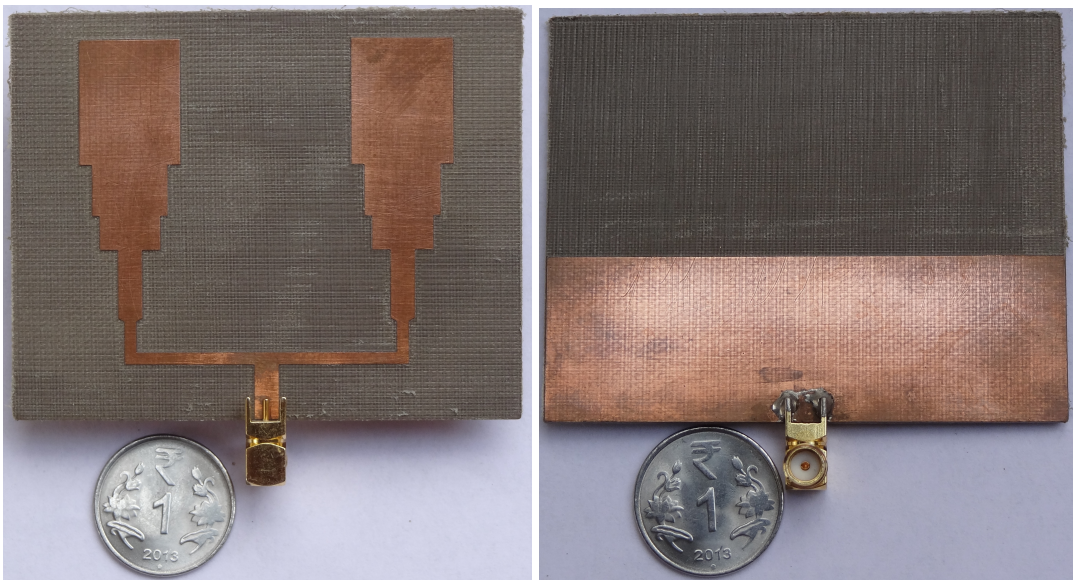

(a) (b)

Figure 3.16: Fabricated prototype of the 1×2 dualband omnidirectional antenna array : (a) Patch side (b) Ground side.

The fabricated prototype shows a considerable bandwidth achievement over the desired bands of operation. Table 3.3 compares the measured performance of the fabricated antenna with reported printed monopole single patch antenna.

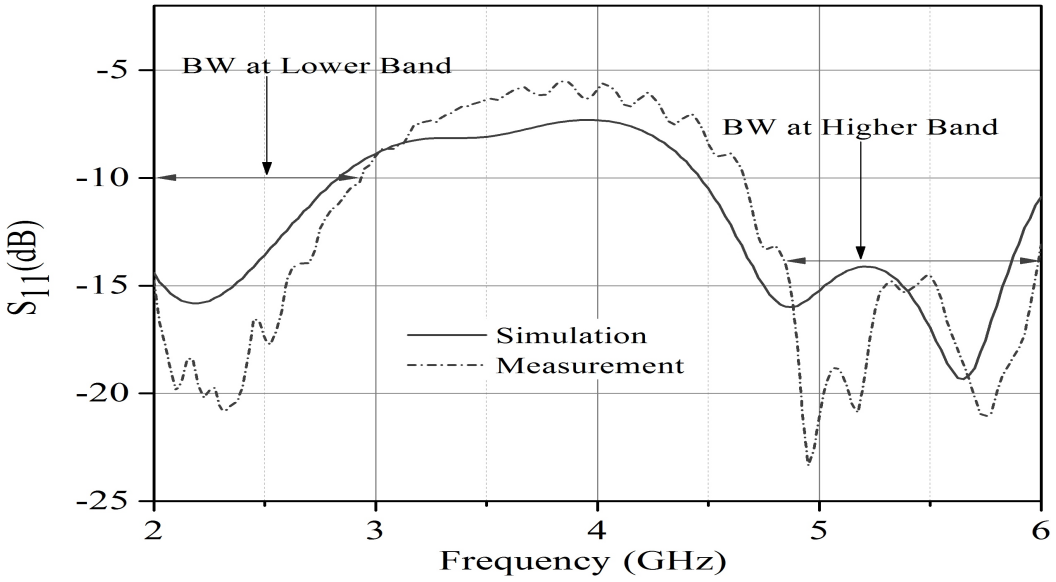

Figure 3.17: Return loss characteristics of the 1×2 dualband omnidirectional antenna array.

Table 3.3: Bandwidth comparison

Bandwidth at	Rathore et al. [85]	Proposed Work
2.44 GHz	760 MHz	975 MHz
5.25 GHz	720 MHz	1000 MHz

Fig.3.18 illustrates the 3D radiation pattern for the omni-directive patch antenna array at the two design frequencies. The simulated and the measured radiation pattern show the broadside directive nature of the antenna.

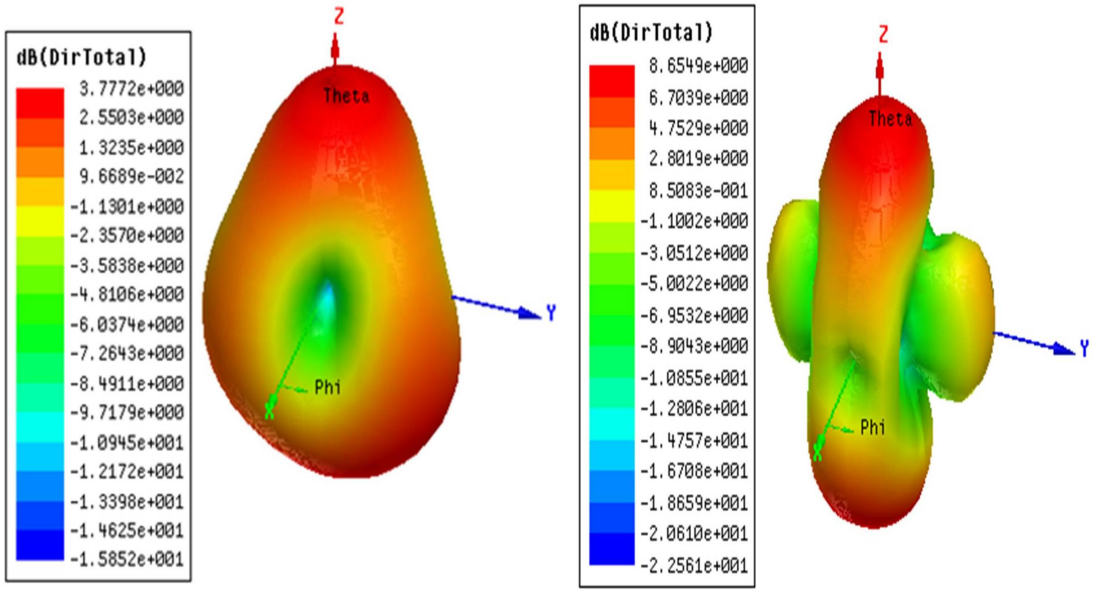

Figure 3.18: Simulated 3D radiation pattern for the omnidirectional patch antenna array at 2.44 GHz and 5.25 GHz.

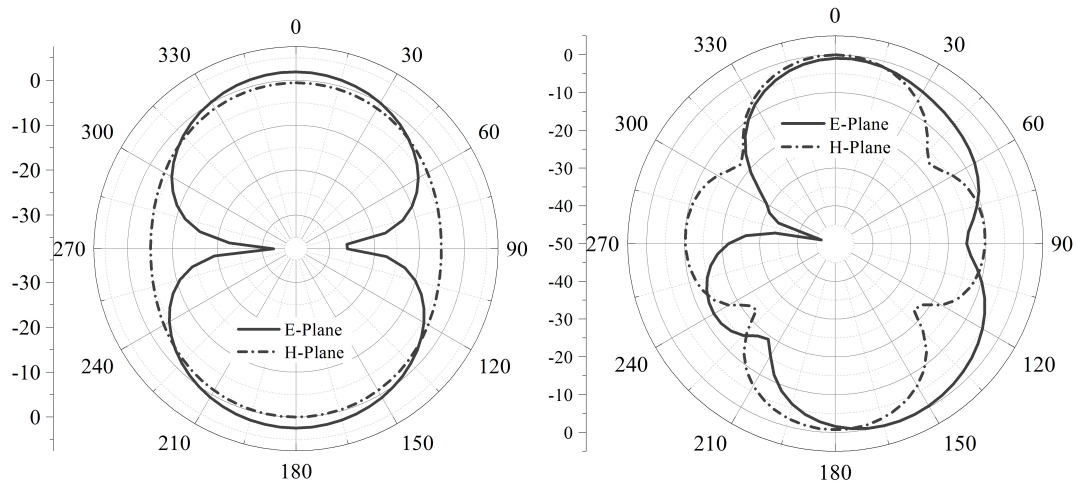

(a) (b)

Figure 3.19: Simulated radiation pattern for the omnidirectional patch antenna array at : (a) 2.44 GHz (b) 5.25 GHz.

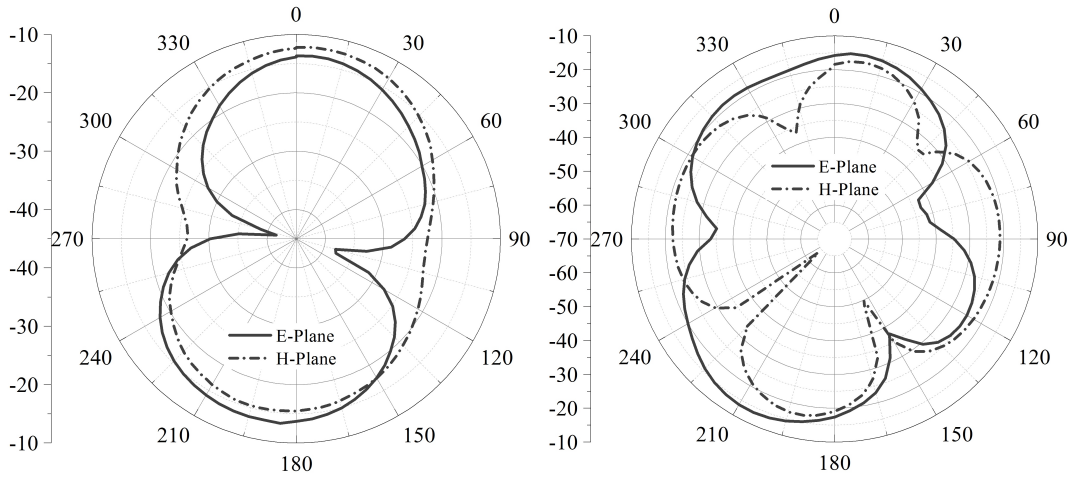

Figure 3.20: Measured radiation pattern for the omnidirectional patch antenna array at : (a) 2.44 GHz (b) 5.25 GHz.

The radiation pattern is highly omni-directive in nature which makes this antenna suitable for WLAN and Bluetooth applications. The radiation pattern and return loss characteristics confirm the dualband nature of this antenna. However, this kind of radiation pattern is suitable for applications in which the occupancy has to be predicted. The very reason is it may pick up the signals from the surroundings due to its broadside directivity. The detailed NIVSD centric utility analysis of the developed antenna prototype is given in *Chapter 5*.

3.3 Conclusions

A low cost,simple in geometry and easily reproducible, concurrent dualband patch antenna array designed and characterization has been discussed in this chapter. The proposed design is carried out to fulfil the needs of the NIVSD system. Three different configurations namely, a single patch, omni-directive array and a directive array have been incorporated in our designed for this purpose.

Chapter 4

Concurrent Dualband Frontend Elements for NIVSD Sensor

4.1 Introduction

This chapter of the thesis describes design details of the different subsystems in the proposed concurrent dualband sensor system. A concurrent dualband WPD is designed as an interconnect. In a wireless receiver design, low noise amplifier (LNA) is a critical crossing point between the antenna and baseband circuitry. As a front end of the receiver, within the bandwidth of interest, it must capture and amplify a very low power or voltage signal along with embedded random noise which the antenna feeds to it. Hence, design of a concurrent dualband LNA is carried out by using standard hybrid monolithic integrated circuit *(HMIC)* technique and by using a high mobility electron transistor *(HEMT)*.

These subsystems operate simultaneously at 2.44 GHz and 5.25 GHz frequency bands and provide a compact, power efficient and low cost solution due to its concurrent operation. Further, two oscillators are designed to operate at 2.44 GHz and 5. 25 GHz band. The proposed design is simulated and verified with advanced design system *(ADS-2009)*. The simulated design is then fabricated on a commercial

NH9320 substrate which is a *poly-tetra-fluoro-ethylene (PTFE) /glass/ceramic dielectric*. It has a dielectric constant (ε_r) = 3.2, height (h) = 1.524 mm, thickness (t) = 18 μm and a loss tangent (δ) = 0.0024. Standard wet etching technique has been used in the fabrication process. The design details and characterization are described in following sections.

4.2 The Concurrent Dualband WPD

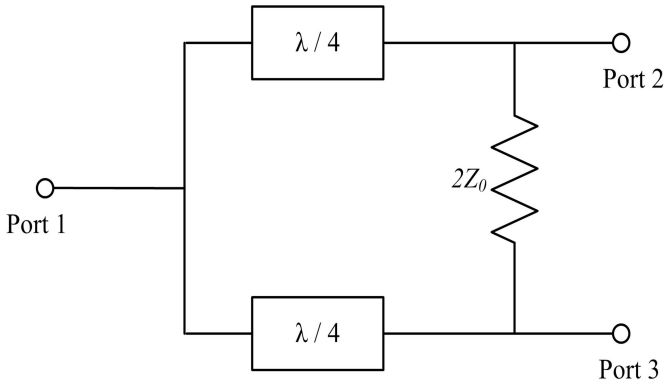

Figure 4.1: A basic three port Wilkinson power divider.

Since its first announcement by E. J. Wilkinson [103], a power combiner and divider holds the key for successful implantation of various microwave/millimeter wave systems. Power combiners are used to combine the power from several inputs whereas a power divider is necessary to distribute the input power among several outputs. In general, a power divider and combiner is a three-port network having single input and double outputs (for divider) or vice versa. The basic functionality of a power divider and combiner can be understood by its scattering parameters [104].

A simple power divider cannot fulfill properties of lossless, reciprocity, and matching at the same time. To overcome this drawback, Wilkinson power divider was developed. An isolation resistor is used between the output ports helps to achieve the above desired properties in a Wilkinson power divider. Besides isolation, this resistor pro-

tects the output ports at the working frequencies. A Wilkinson power divider can be of any number of output ports. A basic three port Wilkinson power divider is shown in Fig. 4.1. The analysis of a Wilkinson's power divider can be carried out by even and odd mode analysis method [104].

4.2.1 Related Work

Many efforts were made by the researchers to acquire the desired power division or combination characteristics with different architectures of WPD. A dualband power divider design using a simplified two section transformer was proposed in [105] but with the drawback of poor return loss and isolation. A power division thechnology was proposed in [106, 107] using inductor and capacitor connected in parallel with the isolation resistor. Topologies such as a 2-way broadband microstrip matched power divider, DGS based power divider, transmission line structure, two section impedance transformers with a parallel RLC circuit, input stub with cascaded transmission line sections, two central transmission line stubs with a low pass filter to achieve wide band operation have also been reported in the literature [108–112].

All these mechanisms have their own pros and cons such as size of the circuitry, number of operational bands, and extra circuitry to achieve dualband operation. The proposed NIVSD system requires a WPD / WPC which should be compact and must support concurrent operation at 2.44 GHz and 5.25 GHz without any additional switching mechanism. To meet these requirements, the structure reported in [110] is further modified to work with the frequency ratio a of 2.15 (f_2 / f_1 = 5.25 / 2.44). A key shaped compact WPD is proposed and used in this analysis. The values of Z_A, Z_B and Z_{OC} are estimated as a function of this frequency ratio.

Equations 4.1 to Eq. 4.3 are used to estimate the required values of Z_A, Z_B and Z_{OC}.

$$Z_A = \sqrt{2} Z_0 tan \frac{\pi}{2} \varepsilon \tag{4.1}$$

$$Z_B = \sqrt{2} Z_0 cot \frac{\pi}{2} \varepsilon \tag{4.2}$$

$$Z_{OC} = \frac{Z_0}{2} \frac{tan^2 \pi\varepsilon}{\sqrt{2}} tan \frac{\pi}{2} \varepsilon \tag{4.3}$$

4.2.2 The Geometry

Fig. 4.2 shows the schematic of the proposed concurrent dualband WPD / WPC to operate simultaneously at 2.44 GHz and 5.25 GHz. A polygon shaped conductor is used to connect Z_A and Z_B with length of 4.2 mm at an angle of 45^o with the horizontal axis. The angle between the microstrip lines of Z_A and Z_{OC} is 30^o. The isolation between *Port 2* and *Port 3* is obtained by connecting a $100\ \Omega$ resistor in between.

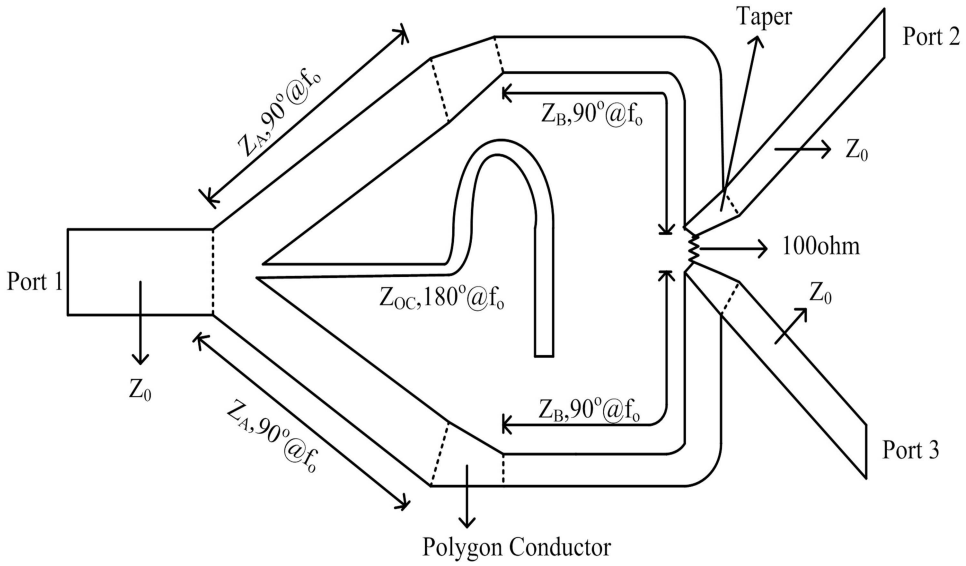

Figure 4.2: Geometry of the proposed WPD.

Due to the modification in the circuit topology and the use of polygon shaped conductors and tapers, the dimensions are further optimized to meet the frequency ratio requirement while conforming to compact size, better return and insertion loss with

Table 4.1: Dimensions of WPD

Impedance (Ω)	With Empirical Relations		With Optimization	
	$L(mm)$	$W(mm)$	$L(mm)$	$W(mm)$
$Z_A = 45.72$	12	4.2	12	3
$Z_B = 109.36$	12.78	0.74	12.78	0.9
$Z_{OC} = 56.44$	24.4	3	28.8	1.02

Table 4.2: S-parameter analysis for the proposed WPD prototype

Frequency(GHz)	$S_{11}dB$		$S_{21}dB$		$S_{23}dB$	
	SIM	$MEAS$	SIM	$MEAS$	SIM	$MEAS$
2.44	-13.45	-11.84	-3.39	-3.48	-19.05	-11.44
5.25	-9.03	-8.54	-3.88	-4.35	-13.78	-18.71

$SIM = Simulation; MEAS = Measurement$

isolation on both bands. Table 4.1 summarizes the dimensions of the proposed WPD. The length of open stub and Z_B are further miniaturized by meandering.

4.2.3 The Characterization

Fig. 4.3 shows the measurement setup and fabricated prototype of the proposed key shaped compact WPD. The overall dimensions of the WPD is 4.2 $cm \times$ 2.5 cm dimension. The effectiveness of WPD operation is further confirmed by its S-parameter values. Table 4.2 provides S-parameter analysis for the proposed WPD prototype.

Fig. 4.4 illustrates the simulated and measured return loss, insertion loss and isolation characteristics of the proposed WPD structure at the desired bands. It clearly indicates its the concurrent dualband nature of operation. A WPD can act as a power divider as

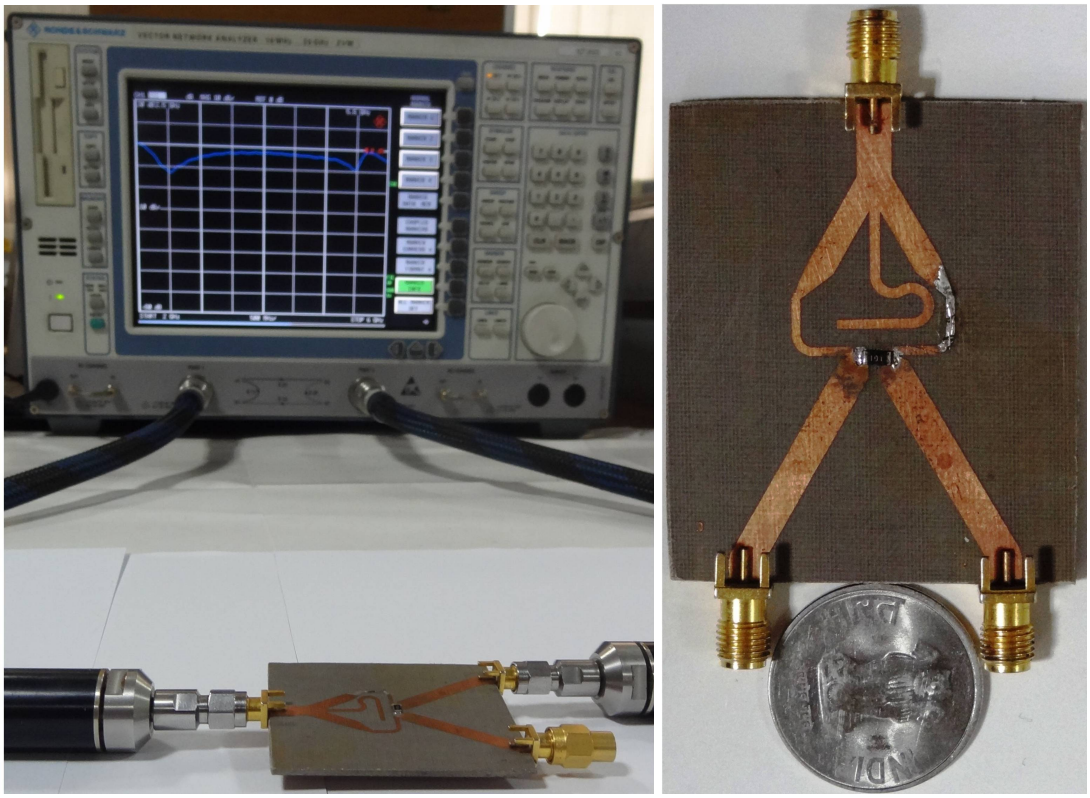

(a) (b)

Figure 4.3: Characterization of the proposed concurrent dualband WPD : (a) Measurement setup (b) The fabricated prototype.

well as a power combiner. This capability of the proposed prototype is further verified by providing a 10 dBm power at *Port-1*. Here, two independent signal source *(R&S SMR 20:10 MHz to 20 GHz and Agilent E8257D PSG: 100 kHz to 20 GHz)* are used at the two designated bands.

The WPD is connected to the source via a cable and connector. The power level is measured with the help of a power meter *(R&S NRVS1020)*. Table 4.3 provides the capacity of the proposed prototype as a power divider. The capacity of WPD as a concurrent power combiner is validated by providing 8.8 dBm input power at *Port 2* while operating at 2.44 GHz and 8 dBm of input power at *Port 3* for 5.25 GHz

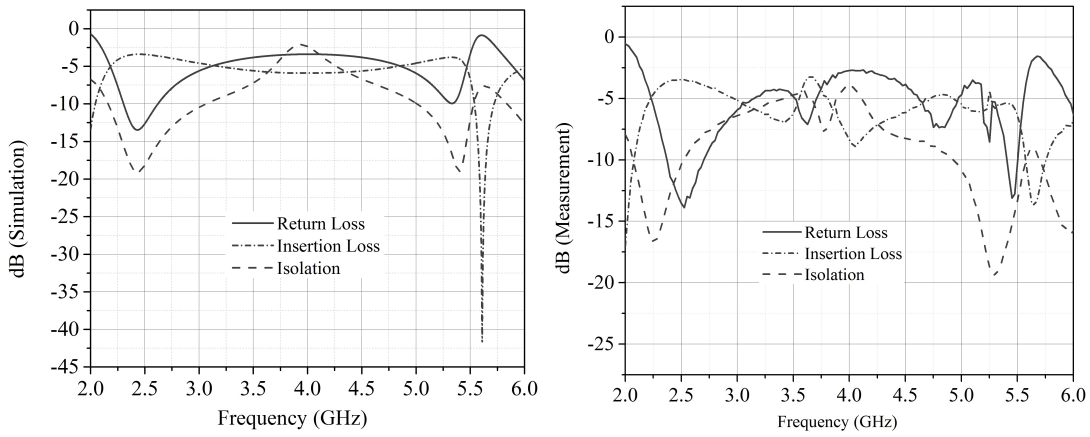

(a) (b)

Figure 4.4: S-parameter characterization of the proposed concurrent dualband WPD : (a) Simulation (b) Measurement.

via cables and connectors. Variations in the supplied power at every individual ports is due to the loss incurred in cables and connectors. At *Port 1*, the measured power is 9.20 dBm which indicates that the proposed WPD can also be used as a power combiner for concurrent dualband operation.

Table 4.3: WPD as a power combiner

Frequency (GHz)	Input Power at *port 1* (dBm)	Output Power at *port 2* (dBm)	Output Power at *port 3* (dBm)
2.44	10.90	5.83	5.94
5.25	8.06	4.30	4.45

4.3 The Concurrent Dualband LNA

4.3.1 Related Work

One of the technical bottleneck for a multistandard transceiver is the implementation of the low noise amplifier (LNA) that can operate at two distinct frequency bands. Conventional dualband architecture adopts two parallel single band LNAs [113]. This approach suffers from high implementation cost, large chip area and high power consumption. Efforts were initiated to comprehend a compact dualband LNA by switched mode operation. In this approach, capacitor and switched inductors are used to toggle between the desired bands [114, 115]. However, this approach also suffers from additional switching circuitry and associated delays with excess chip area to provide the dualband operation. The aforementioned drawbacks may be overcome by designing an LNA with concurrent operation at the desired bands. This kind of approach is based on hardware sharing, i.e. the same hardware supports simultaneous operation at the desired bands. Due to this feature, the cost, size and power consumption of the system can be decreased considerably.

Fig. 4.5 shows the different architectures of the LNA which can be used in radio receiver design. A variety of approaches have been proposed to design and develop a concurrent dualband LNA. The versatility in the design is obtained by choosing a specific set of operating frequencies, a good fabrication technology and an appropriate matching network. Table 4.4 gives a brief overview in LNA design. For the proposed system design, a concurrent dualband LNA is designed, measured and fabricated to operate at 2.44 GHz and 5.25 GHz band. A single *pseudomorphic* HEMT *(p-HEMT)* viz. $ATF-36163$ is used as an active device [*See Appendix- A*]. The proposed LNA is comprehended using standard HMIC process with major focus on maximum hardware sharing without any lumped circuitry. The conceptual diagram of the proposed dualband LNA is shown in Fig. 4.6

Table 4.4: State of the art multiband LNA

Parameter	Dao et.al. [113]*	S.Yoo and H.Yoo [114]	Martins et.al. [115]*	Hashemi and Hajimiri [116]	Proposed Work
Technology	0.18 μm CMOS	0.18 μm CMOS	0.35 μm CMOS	0.35 μm CMOS	p-HEMT
Frequency Band (in GHz)	2.4 and 5.25	2.3 to 2.5 and 5.1 to 5.9	0.9 and 1.8	2.45 and 5.25	Concurrent 2.44 and 5.25
Matching Network	using discrete component	switched inductor and capacitor	using discrete component	using discrete component	Microstrip based
Gain (dB)	11.8 / 16	15 / 15	—	14 / 15.5	7.15 / 7.80
NF (dB)	3.6 / 2.5	2.3 / 2.4	3 / 3	2.3 / 4.5	4.3 / 4.6
Return Loss (dB)	-16 / -30	-25 / -20	-10 / -10	-25 / -25	-10.54 / -15.98

$\star$ - Simulation results are reported.

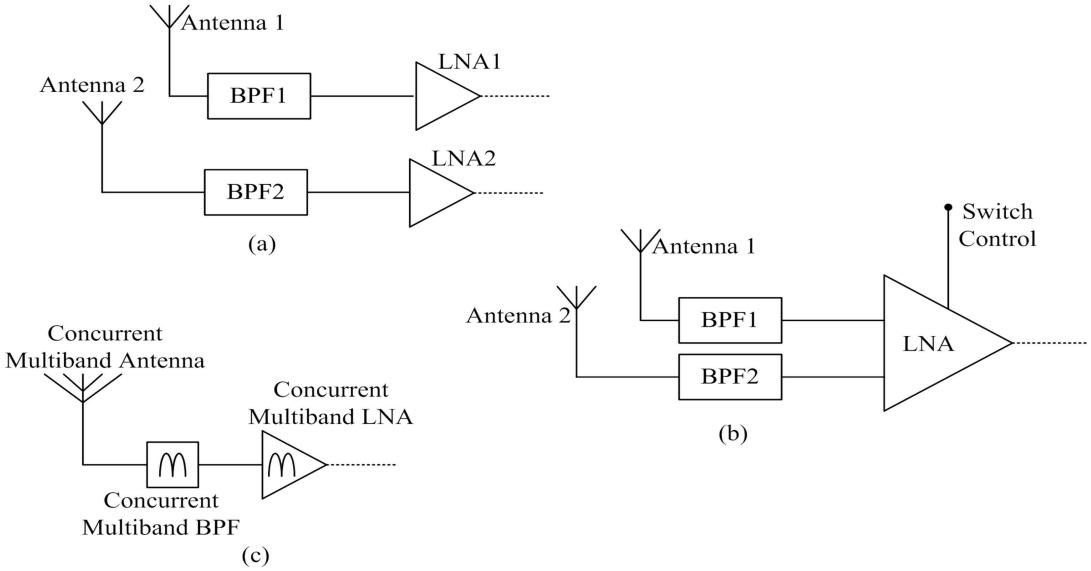

Figure 4.5: LNA Topology: (a) Parallel topology (b) Switchable topology and (c) Concurrent topology.

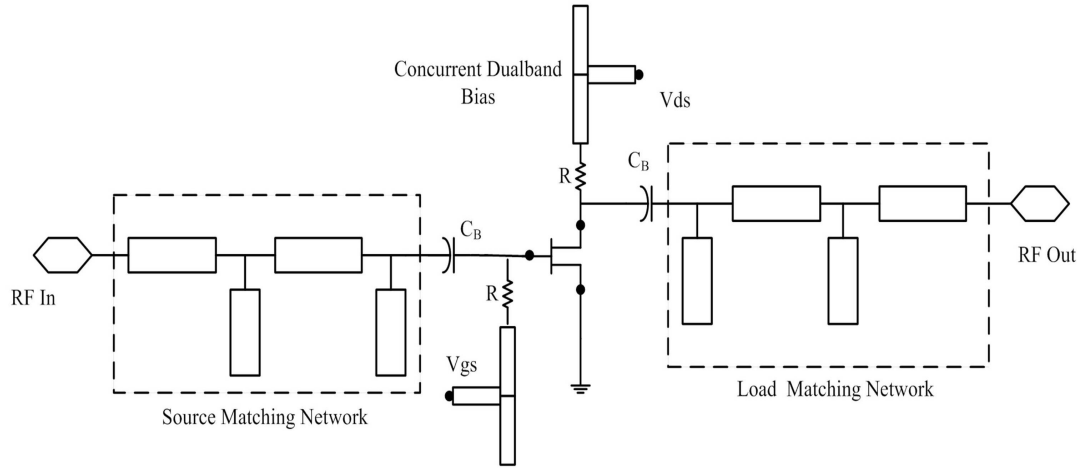

Figure 4.6: Proposed concurrent dualband LNA for non-invasive human vital sign detection.

The entire design procedure in ADS consists of the following major steps:

- DC Bias simulation and Bias Network design
- S-Parameter analysis

- Design of matching network
- Simulation and optimization of the layout using Electromagnetic design system (EMDS)
- Fabrication

4.3.2 DC Bias Point and Stability Analysis

DC Bias simulation is performed using the ADS model for $ATF-36163$ transistor. From the FET Curve Tracer template, an operating quiescent point is selected for linear operation of the transistor in the active region. The DC Bias point selected from the simulation setup is given in Table 4.5. In stability analysis, it is found that

Table 4.5: Operating quiescent point of ATF-36163 transistor

Symbol	Parameter	Value
V_{DS}	Drain to Source Voltage	$2.75\ Volt$
I_{DS}	Drain to Source Current	$13\ mA$
V_{GS}	Gate to Source Voltage	$-0.2\ Volt$

$ATF-36163$ is unconditionally stable at 5.25 GHz, but not so at 2.44 GHz. Thus, it needs to be stabilized before its use. A stabilizing resistance of suitable value may be appended either at the input or at output end of the transistor. Furthermore, this resistance may be connected either in series or in parallel. In general, appending a single stabilizing resistor at either end of a transistor stabilizes it. A shunt stabilizing resistance R_d is added at the output end of $ATF-36163$ in order to stabilize it for LNA design. From the load stability circle of the transistor, it can be stabilized at 2.44 GHz (and above) by using a stabilizing resistance greater than 17.95Ω . The required minimum value approaches 100Ω as the operating frequency tends towards

$1\ GHz$. To ensure unconditional stability upto the lowest RF of $1\ GHz$, a stabilizing shunt resistance of 100Ω is selected for connection at the output end of the DC biased $ATF-36163$. S-parameters for the transistor at the specified bias are obtained using S-parameter simulation in ADS, using the transistor's model. Initially, a DC feed (ideal) is used in the bias network for isolation of RF. The S-parameter obtained from the simulation is given in Table 4.6.

Table 4.6: S-parameters of $ATF-36163$ Transistor

Frequency(in GHz)	S_{11}	S_{12}	S_{21}	S_{22}
2.44	0.849 $\angle -52.013^o$	0.032 $\angle 41.179^o$	3.179 $\angle 118.21^o$	0.633 $\angle -12.608^o$
5.25	0.574 $\angle -108.244^o$	0.054 $\angle -3.851^o$	2.478 $\angle 58.339^o$	0.492 $\angle -10.049^o$

The transistor's stability is analyzed at the two design frequencies with the help of K-Δ and μ tests. Basic equations for stability measurement are given as [117]:

$$|\Delta| = |S_{11}S_{22} - S_{12}S_{21}| < 1 \tag{4.4}$$

$$K = \frac{1 - |S_{11}|^2 - |S_{22}|^2 + |\Delta|}{2|S_{12}S_{21}|} > 1 \tag{4.5}$$

$$\mu = \frac{1 - |S_{11}|^2}{|S_{22} - \Delta S_{11}^{\star}| + |S_{12}S_{21}|} > 1 \tag{4.6}$$

$$\mu_{prime} = \frac{1 - |S_{22}|^2}{|S_{11} - \Delta S_{22}^{\star}| + |S_{12}S_{21}|} > 1 \tag{4.7}$$

Δ, K, μ and $\mu_{\hat{A}\c{t}prime}$ values from Table 4.7 signify that the transistor is unconditionally stable at both the frequencies of interest. Further, DC feed in the bias network is replaced by a novel concurrent dual-band DC bias network design.

Table 4.7: Stability analysis of $ATF-36163$ Transistor

Frequency (in GHz)	Δ	K	μ	μ_{prime}
2.44	0.615	1.257	1.207	1.058
5.25	0.415	2.252	1.729	1.506

4.3.3 Design of Concurrent DC Bias Network

In general, a microstrip transmission line (TL) based DC bias Tee network consists of a quarter wave impedance transformer with high characteristic impedance. Such network works at the designed frequency and its odd harmonics. However, it is not useful in a multiband circuit where high input impedance is required at multiple uncorrelated frequencies. Hence, a concurrent dualband DC bias network is proposed which is realized using microstrip TL sections only. Fig. 4.7 shows the proposed DC bias network. DC bias voltage source is applied to a TL section TL_1 with characteristic impedance Z_1 and electrical length θ_1(f). TL_1 is connected in shunt at the middle of another TL section TL_2 with characteristic impedance Z_2 and electrical length $2\theta_2(f)$. One end of TL_2 is left open while its other end is connected to the main RF signal carrying TL path. The structure is designed in such a way that it exhibits high input impedance Z_{IN} at the two RF frequencies of interest f_1 and f_2. As one end of TL_2 is open Z_{IN} will be high at frequencies where TL_2's the total electrical length is an integer multiple of 180^o.

For short TL length, the electrical length of TL_2 is kept equal to 180^o at the higher operating frequency f_2. In other words

$$\theta(f) = [\frac{\pi}{2}.\frac{f}{f_2}] \tag{4.8}$$

Connecting TL_1 in shunt, exactly in the middle of this TL_2 will not affect the high Z_{IN} value at f_2. The DC bias voltage source is applied through another end of TL_1.

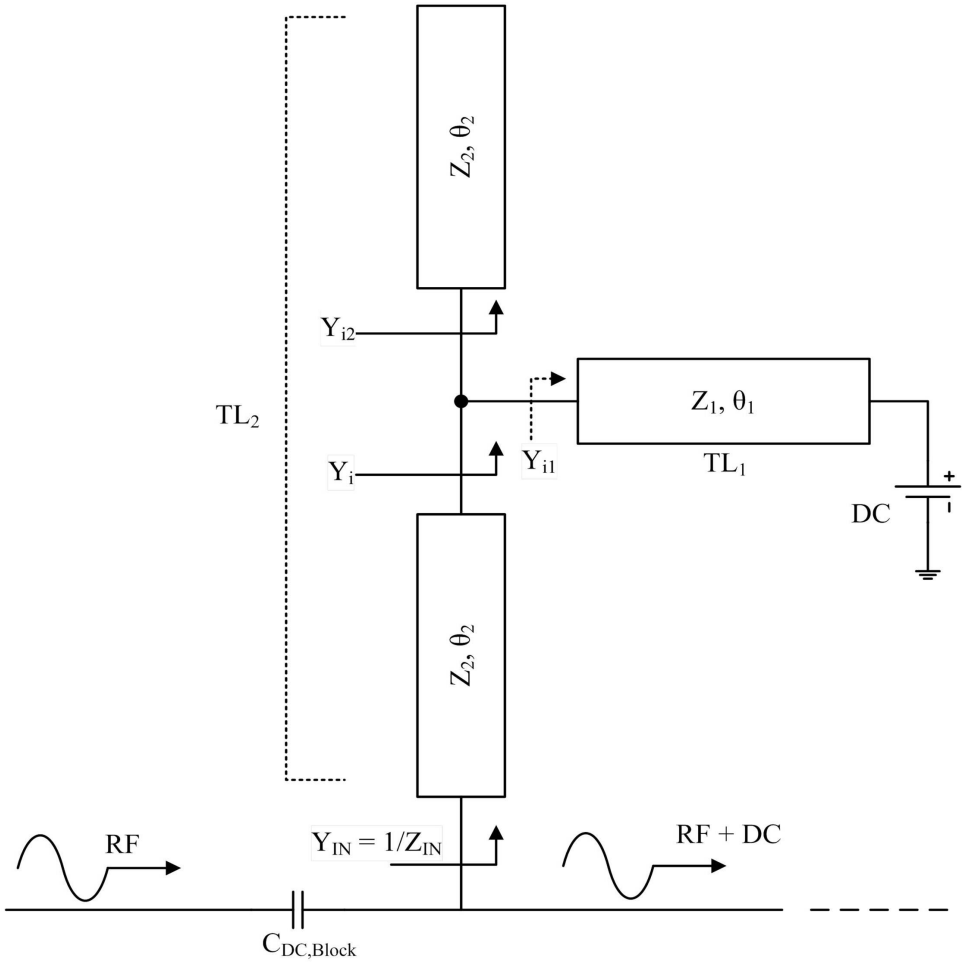

Figure 4.7: Proposed concurrent dualband DC bias network.

Design parameters of TL_1 are calculated by considering the requirement that Z_{IN} is high at the lower operating frequency f_1 also. The input admittance at half of the first open ended TL_2 sections are

$$Y_{i2}(f) = j\frac{tan\theta_2(f)}{Z_2} = jY_2tan[\frac{\pi}{2}.\frac{f}{f_2}] \tag{4.9}$$

During RF analysis, DC connection is considered as analog ground. Therefore, input admittance of the AC grounded TL_1 is given as

$$Y_{i1}(f) = \frac{1}{jZ_1tan\theta_1(f)} = -jY_1cot\theta_1(f) \tag{4.10}$$

Overall admittance seen at the edge of the second half of TL_2 is given as

$$Y_i(f) = Y_{i1}(f) + Y_{i2}(f) = j[(Y_2 tan\theta_2(f)) - (Y_1 cot\theta_1(f)) \tag{4.11}$$

Final input admittance shown by the whole structure at any frequency is then calculated as

$$Y_{IN}(f) = Y_2 \frac{Y_i(f) + jY_2 tan\theta_2(f)}{Y_2 + jY_i(f) tan\theta_2(f)} \tag{4.12}$$

With $Z_{IN}(f_1) = \infty$ or, equivalently, $Y_{IN}(f_1) = 0$, the numerator is required to be zero. Thus

$$Y_i(f_1) + jY_2 tan\theta_2(f_1) = j[(2Y_2 tan\theta_2(f_1)(Y_1 cot\theta_1(f_1))] = 0 \tag{4.13}$$

$$\Rightarrow \theta_1(f_1) = tan^{-1}[\frac{Z_2}{2Z_1 tan\theta_2(f_1)}] = tan^{-1}[\frac{Z_2}{2Z_1 tan(\frac{\pi}{2} \cdot \frac{f_1}{f_2})}] \tag{4.14}$$

Eq.4.8 and Eq. 4.14 indicates that the characteristic impedances of both the TL sections can be chosen arbitrarily ensuring fabrication feasibility. With the aforementioned design relations, the proposed DC bias network will exhibit high input impedance at any two uncorrelated desired frequencies f_1 and f_2. Here, f_1 and f_2 are 2.44 GHz and 5.25 GHz, respectively. S-parameters and corresponding stability measures are unaffected by the introduction of this bias network and are same as that with DC feed (ideal). Furthermore, the electromagnetic simulation using EMDS shows that the proposed dualband DC bias network offers very high input impedance. Fig. 4.8 shows the EMDS response of the proposed DC bias network.

A high characteristic impedance value, within feasible fabrication limits, is chosen for all TL sections in the bias network which further increases input impedance at the two RF frequencies. For instance, in the current scenario, widths of all TL sections are kept at 1 mm, leading to high characteristic impedance. Table 4.8 tabulates dimensions of the proposed concurrent dualband DC bias network for ideal and EMDS simulations.

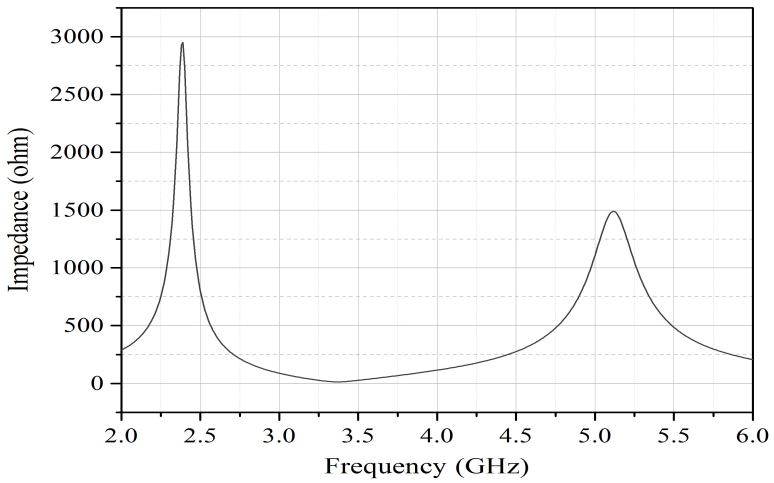

Figure 4.8: EMDS response of the proposed concurrent dualband DC bias network.

Table 4.8: Dimensions of the proposed concurrent dualband bias network

Frequency(in GHz)	Ideal Simulation		EMD Simulation	
	Length (mm)	Width (mm)	Length (mm)	Width (mm)
2.44	6.52	1	6.46	1
5.25	9.25	1	9.26	1

4.3.4 Concurrent Dualband Matching Network

The dualband matching network is designed using microstrip lines by calculating reflection coefficients at source and load ends of the transistor with the proposed DC bias network. The matching network employs series TL sections and stubs to transfer complex impedance seen at the terminals of the transistor to $50\ \Omega$ at the port. Two stubs are connected in shunt to the main line and are open circuited.

Fig. 4.9 shows the impedance transformer structure that is used for dualband matching. The problem of infeasible characteristic impedances is mitigated by considering four physical lengths of series TL sections and stubs as design parameters. Hence, designer can arbitrarily set characteristic impedances of all TL sections. Such consid-

eration not only allows dualband matching of unequal complex impedances, but also admits feasible fabrication of microstrip transmission-line sections.

Consider the network shown in Fig. 4.9. Let Y_L be the load admittance which is converted to Y_B by the first series TL section of length L_2 and an open circuit shunt stub of length S_2. This admittance is further transformed into standard admittance Y_0 by another series TL section of length L_1 and an open ended shunt stub of length S_1. For ease of analysis and feasible fabrication, characteristic impedance of all TL sections and stubs are set to standard $50\ \Omega$. Considering the normalized admittance with respect to Y_0 as y_L, y_B and y_A the transmission line theory leads to the following design relations

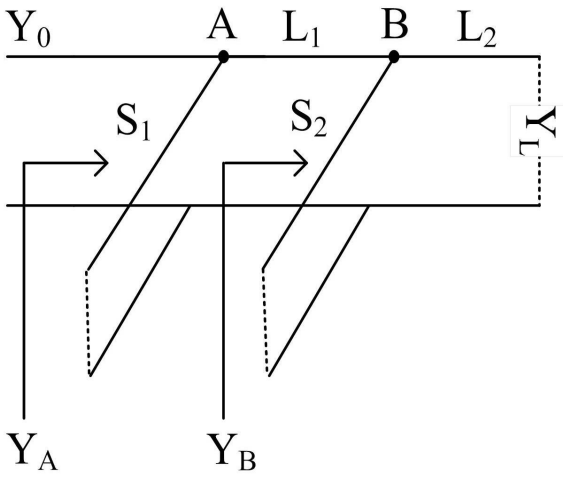

Figure 4.9: Concurrent dualband matching network.

$$y_B = [\frac{(y_L + jtan\beta L_2)}{1 + jy_L tan\beta L_2}] + jtan\beta S_2 \tag{4.15}$$

$$y_A = [\frac{(y_B + jtan\beta L_1)}{1 + jy_B tan\beta L_1}] + jtan\beta S_1 \tag{4.16}$$

$$y_L = g_L + j\beta_L \tag{4.17}$$

Further, consider the two frequencies of interest as f_1 and f_2. Consequently, two different load admittance Y_{L1} and Y_{L2} need to be matched at the two frequencies f_1 and

f_2 respectively. Moreover, the propagation constant, γ also varies with the operating frequency. Accordingly, six equations are obtained for simultaneous impedance matching at the two design frequencies. Given the values for y_{L1} and y_{L2} the lengths L_1, L_2, S_1 and S_2 are adjusted such that all these equations are satisfied simultaneously, i.e., load impedances at f_1 and f_2 are simultaneously matched to $50\ \Omega$.

Table 4.9: Reflection coefficients

Frequency (in GHz)	At Source (Γ_S)	At Load (Γ_L)
2.44	$-0.708 + j0.662$	$-0.180 - j0.116$
5.25	$-0.926 - j0.265$	$-2.10 \times 10^{-3} - j0.398$

Based on the derived equations, a MATLAB code is developed to provide all possible solutions for feasible length parameters for dualband impedance matching *[See Appendix : B]*. Table 4.9 lists the required reflection coefficients at both ends of the biased transistor at the two frequencies of interest. Required impedances can be calculated from the reflection co-efficient values. Considering the complex impedances as target load, design parameters for the input and the output matching networks are obtained using the MATLAB code. The code is written to solve the design equations 4.15 to 4.17 for concurrent dualband complex impedance matching through the conventional double open ended shunt stub structure. Inputs to the program are the two design frequencies along with the corresponding source and load refection coefficients. Moreover, substrate parameters, such as dielectric constant, height, etc., are also provided in order to consider their effects while performing computations at the two frequencies of interest. The program provides all possible solutions in terms of physical lengths of the series, TL sections and the open circuited shunt stubs. Based on the reflection coefficients, corresponding electrical lengths and physical lengths of the matching networks are given in Table 4.10.

Table 4.10: Electrical and Physical length of the matching network

Matching Network	L_1		L_2		S_1		S_2	
	ELE	PHY	ELE	PHY	ELE	PHY	ELE	PHY
Input	63.19	13.44	59.03	12.55	55.56	11.81	67.01	14.25
Output	91.51	19.46	140.54	29.89	53.41	11.36	22.56	4.8

$ELE = ElectricalLength(degree); PHY = PhysicalLength(mm)$

Physical lengths, obtained from ADS '*Line Calc tool*' are used for creation of layout. These dimensions are further optimized using EMDS simulation to obtain the desired results. Table 4.11 gives these optimized dimensions for the matching network. A layout is created including the input and the output matching networks, with the help of the physical lengths that are obtained from ideal simulation in ADS. Ports are placed at the input and the output of the network, as well as at every point where an external lumped device interfaces with the network. The matching network in ADS circuit is then replaced with this layout and EMDS co-simulations are performed.

Table 4.11: Optimized dimensions of the matching network

Matching Network	$L_1(mm)$	$L_2(mm)$	$S_1(mm)$	$S_2(mm)$
Input	6.73	41.44	14.91	13.88
Output	5.88	12.37	13.3	15.82

While designing the layout, width of all microstrip lines are kept constant at 3.64 mm, which corresponds to the characteristic impedance $50\ \Omega$ of the chosen substrate. In addition, $50\ \Omega$ microstrip line and a taper are used at both ends of the matching network.

It helps to mitigate the effect of evanescent modes caused due to junctions, transitions and port connections.

4.3.5 Measurement and Analysis

Fig. 4.10 depicts the measurement setup and the fabricated prototype of the proposed concurrent dualband LNA. For analysis purpose, S-Parameters are calculated from measurement setup. Fig. 4.11 provides the plot of the measured and simulated S_{11} and S_{21} and is summarized in Table 5.7.

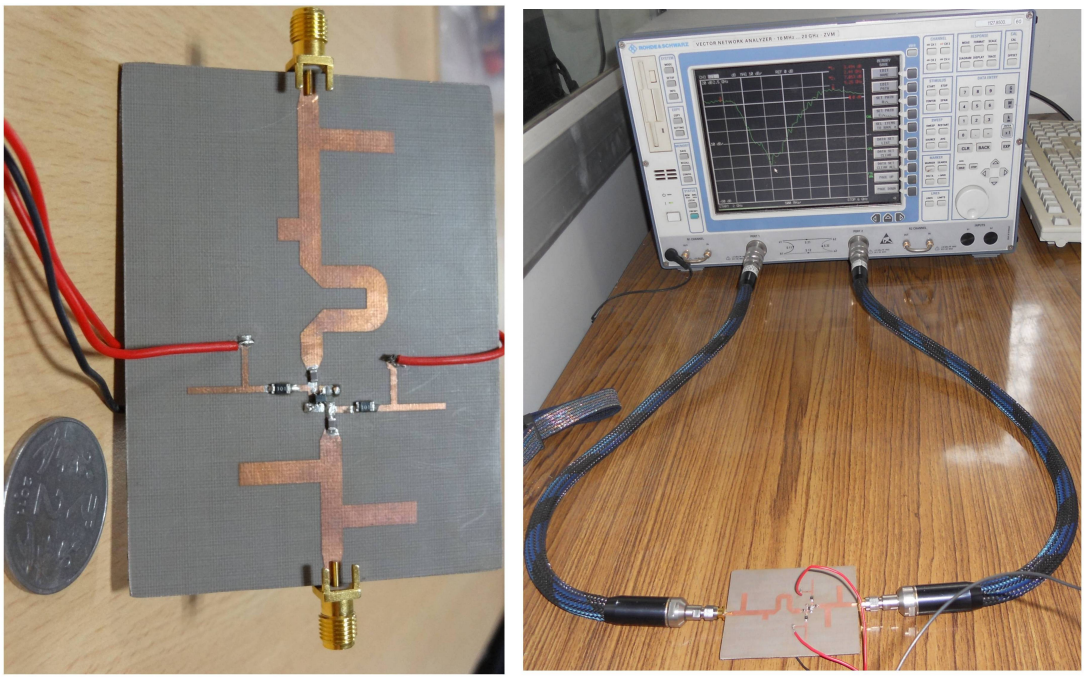

(a) (b)

Figure 4.10: Characterization of the proposed concurrent dualband LNA: (a) Fabricated prototype (b) Measurement setup.

The noise figure(NF) is measured with the help of Agilent noise figure meter setup. Fig. 4.12 shows the measurement setup and the plot of simulation and measured NF

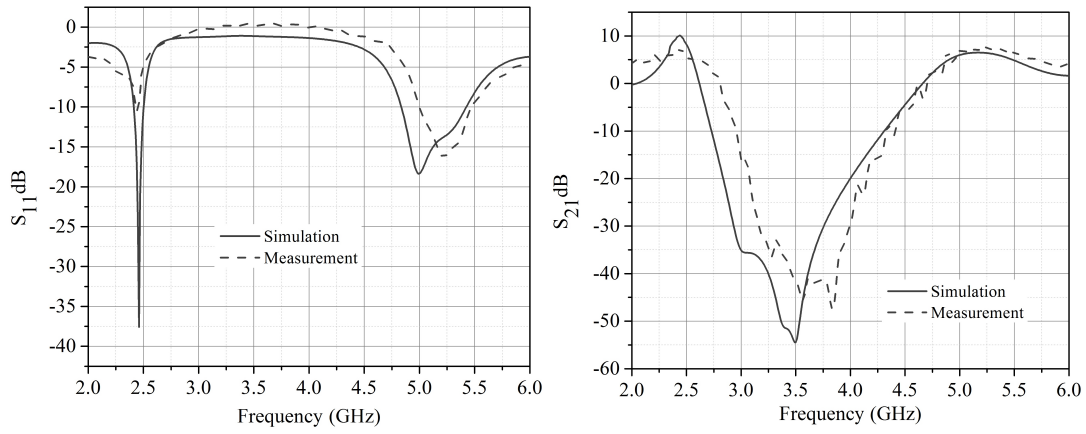

(a) (b)

Figure 4.11: S-parameter performance of the proposed concurrent dualband LNA: (a) S_{11} (b) S_{21}.

of the proposed concurrent dualband LNA and is summarized in Table 4.13. The proposed concurrent dualband LNA exihibitsNF at par with LNA's reported in [116,118]. Hence the amplifier passes the preferred frequencies while rejecting the undesired frequencies with a reasonable NF. All the aforementioned characteristics make the proposed concurrent dualband LNA suitable to be used as a subsystem in an RF Sensor system for NIVSD.

Table 4.12: Gain analysis of the proposed dualband LNA

Frequency(in GHz)	$S_{11}(dB)$		$S_{21}(dB)$	
	Simulation	Measurement	Simulation	Measurement
2.44	-17.24	-10.54	10.11	7.16
5.25	-13.48	-15.98	6.40	7.80

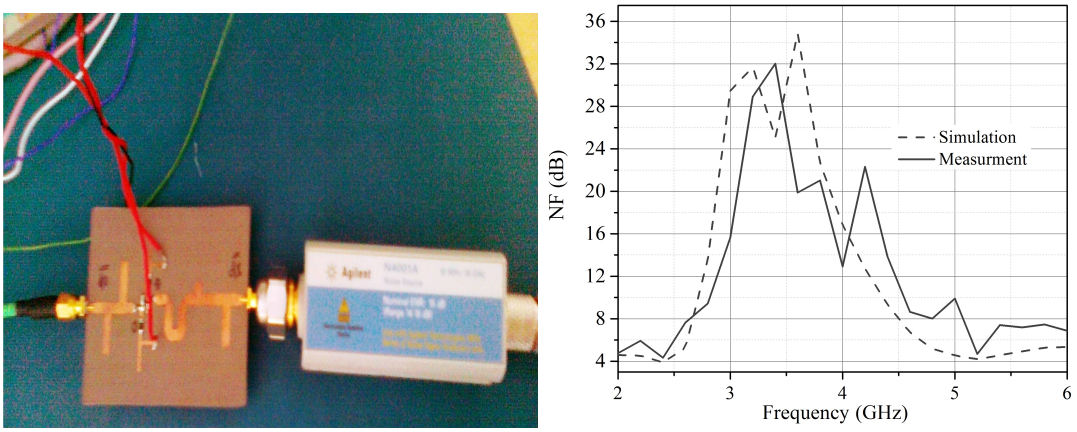

(a) (b)

Figure 4.12: Noise Figure Analysis of the proposed concurrent dualband LNA: (a) Measurement setup (b) Simulated and Measurement performance.

Table 4.13: Noise figure analysis

Frequency(in GHz)	Simulation	Measurement
2.44	3.90	4.30
5.25	4.20	4.60

4.4 The Oscillators

To cater the need of a source, two oscillators are designed to operate at 2.44 GHz and 5.25 GHz. A microwave oscillator consists of frequency selective circuit (resonator), negative resistance cell (transistor with positive feedback and biasing circuit) and output matching circuit as shown in Fig. 4.13. The Barkhausen criterion for sustainable oscillation states that

- Amplitude Condition - The cascaded gain and loss through the amplifier / feedback network must be greater than unity.

- Phase Condition - The frequency of oscillation will be at the point where loop phase shift totals 360 (or zero) degrees.

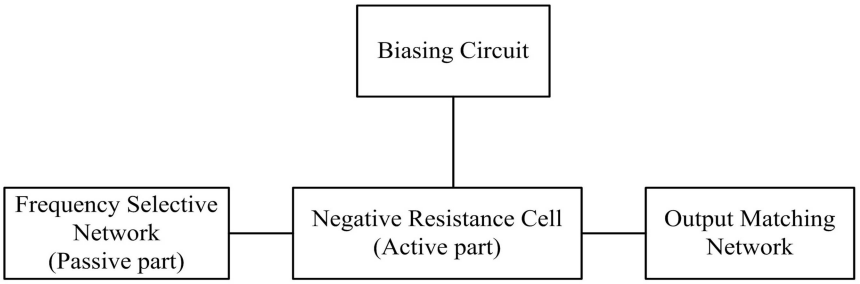

Figure 4.13: Block diagram of negative resistance based typical oscillator.

Fig. 4.14 indicates the basic equivalent circuit for an oscillator. The input impedance is current (or voltage) dependent as well as frequency dependent and can be written as

$$Z_{in}(V,\omega) = R_{IN}(V,\omega) + jX_{IN}(V,\omega) \tag{4.18}$$

The device is terminated with passive load impedance Z_L, defined as

$$Z_L(\omega) = R_L(\omega) + jX_L(\omega) \tag{4.19}$$

Applying Kirchhoff's voltage law (KVL) we get

$$Z_{in}(V,\omega) + Z_L(\omega) = 0 \tag{4.20}$$

The one port network is stable if

$$Re[Z_{in}(V,\omega) + Z_L(\omega)] > 0 \tag{4.21}$$

For the oscillation to start, negative resistance of the active device in a series circuit must exceed the load resistance by about 20% (i.e.$R_{in} = -1.2R_L$).

$$R_{in}(V,\omega) + R_L(\omega) = 0 \tag{4.22}$$

$$X_{in}(V,\omega) + X_L(\omega) = 0 \tag{4.23}$$

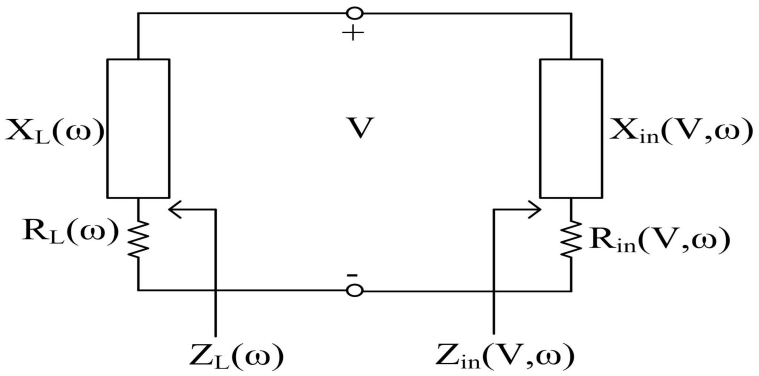

Figure 4.14: Equivalent circuit for one port negative resistance microwave oscillators.

Initially, it is necessary for the overall circuit to be unstable at a certain frequency (i.e.,the sum of R_L and R_{in} be a negative number).

$$|R_{in}(V,\omega)| > R_L(\omega) \tag{4.24}$$

Any transient excitation or noise then causes the oscillation to build up at a frequency ω. The load is passive, $R_L > 0$ and Eq. 4.22 indicates that $R_{in} < 0$. Thus, a positive resistance implies energy dissipation, a negative resistance implies an energy source. The condition of Eq. 4.24 controls the frequency of oscillation. For the stability of an oscillator, high-Q resonant circuits such as cavities and dielectric resonators are used.

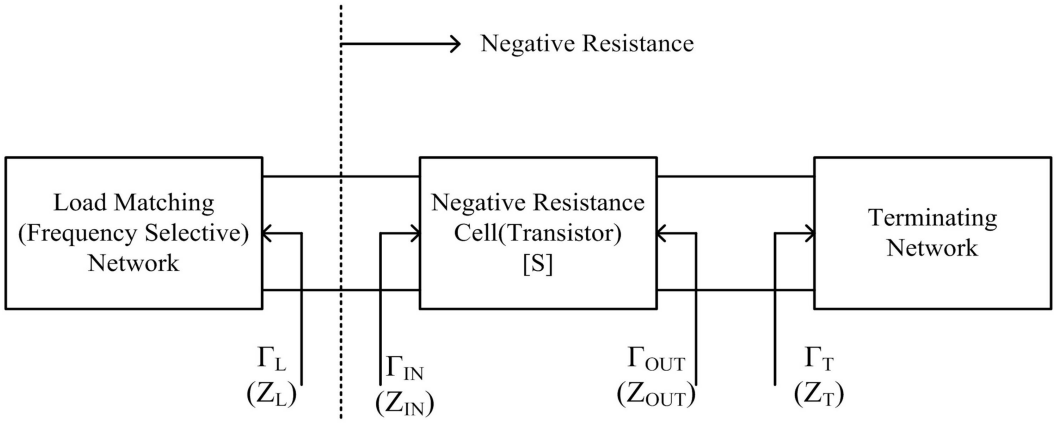

Figure 4.15: Block diagram of microwave transistor based oscillator.

The design procedure described here is general and applies to any transistor circuit configuration as long as its S-parameters are known. Unlike the amplifier circuit, the transistor for an oscillator design must be unstable. In a transistor oscillator, a negative resistance is effectively created by terminating a potentially unstable transistor with impedance designed to drive the device in an unstable region. Fig. 4.15 depicts the block diagram of a transistor based oscillator. The following section describes the design procedure of an oscillator.

4.4.1 DC Bias Simulations and Bias Network Design

A *Si*-doped *AIGaAs* FET *NE4210S01* is selected for this design since its operating frequency is from 2 GHz to 18 GHz *[See Appendix-C]*. DC Bias simulation is performed in ADS-2009 using the transistor model. DC bias point for oscillator design was selected as $V_{DS} = 2\,V$ and $I_{DS} = 10\,mA$ and $V_{GS} = 0.69\,V$. A microstrip line biasing circuitry is selected for the DC bias *NE4210S01*. Fig. 4.16 shows a microstripline bias network.

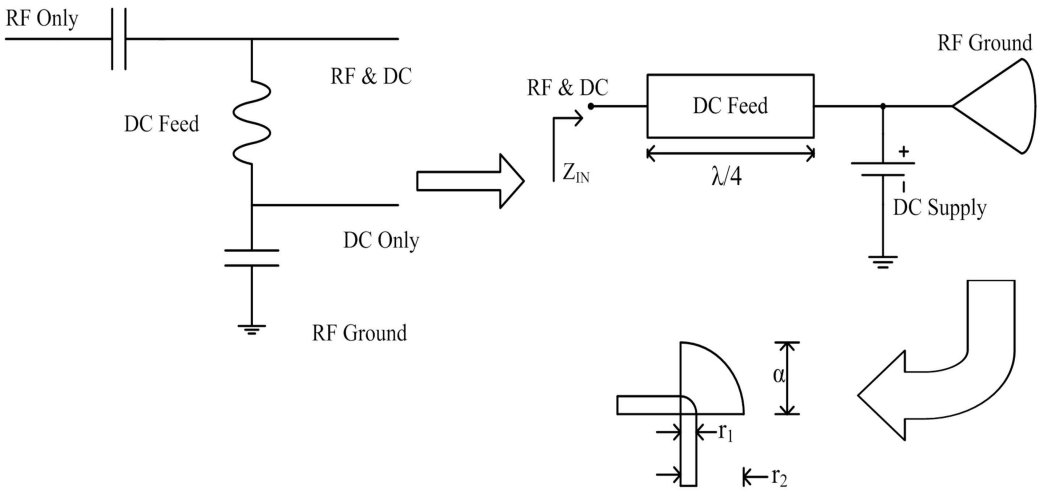

Figure 4.16: A microstripline bias network.

In microstrip implementation, the inductor may be substitute by a high impedance line and the capacitor can be realized as an open or a radial stub. A radial stub is used to provide a broadly resonant RF short circuit. When cascaded with high impedance quarter wavelength transmission lines the radial stub provides an effective decoupling network for microwave amplifiers and other active components [119]. The high impedance (selected as $130\ \Omega$) quarter wavelength (with electrical length 90^0) microstrip line is followed by a radial stub. The dimensions are calculated using *'line calc'* tool in *ADS 2009*. The bias network design is similar for 2.44 GHz and 5.25 GHz band except for the variation in the dimensions. Table 4.14 and 4.15 provides the dimensions of the bias network.

Table 4.14: Dimensions for bias network

$Z_0(\Omega)$	Frequency(GHz)	W(mm)	L(mm)
130	2.44	0.43	20.39
130	5.25	0.43	9.44

Table 4.15: Dimensions of the radial stub

Frequency(GHz)	r_1 (mm)	α ($degree$)	$r_2(mm)$
2.44	0.43	60	12.89
5.25	0.43	60	6.86

4.4.2 Stability Analysis and S-parameter Simulation

S-Parameter simulation is performed with the DC bias network. Table 4.16 provides the S-parameters for the proposed oscillator design. Using the S-Parameters, transistor's stability is analyzed at the two design frequencies with the help of K-Δ and μ

Table 4.16: S-parameters of *NE4210S01* Transistor

Frequency (GHz)	S_{11}	S_{12}	S_{21}	S_{22}
2.44	1.208 $\angle -8.201^o$	0.075 $\angle 83.818^o$	2.311 $\angle -128.844^o$	1.110 $\angle -14.797^o$
5.25	1.960 $\angle -48.895^o$	0.256 $\angle 50.711^o$	6.814 $\angle 168.060^o$	1.490 $\angle -54.867^o$

tests as per Eq. 4.4 to Eq. 4.7. Table 4.17 summarizes the stability analysis for the proposed oscillators. It is observed that the transistor is unconditionally unstable at the desired frequencies.

Table 4.17: Stability analysis of NE4210S01 Transistor

Frequency (GHz)	Δ	K	μ	μ_{prime}
2.44	1.184	-0.847	-0.921	-0.779
5.25	1.866	-0.452	-0.657	-0.363

4.4.3 Design of Matching Network

Based on the S-parameters, an impedance matching network design is initiated. It can be designed either analytically or with Smith chart as a graphical design tool. For the common source with series capacitive feedback S-parameters, the input and the output stability circles are drawn on the Smith chart using Smith chart utility in *ADS-2009*, as shown in Fig. 4.17 and 4.18. The input stability circle is a contour in the source plane

that indicates source termination values that makes the output reflection coefficient to have unity magnitude. An output reflection coefficient less than unity indicates a stable device, while an output reflection coefficient greater than unity indicates a potentially unstable device.

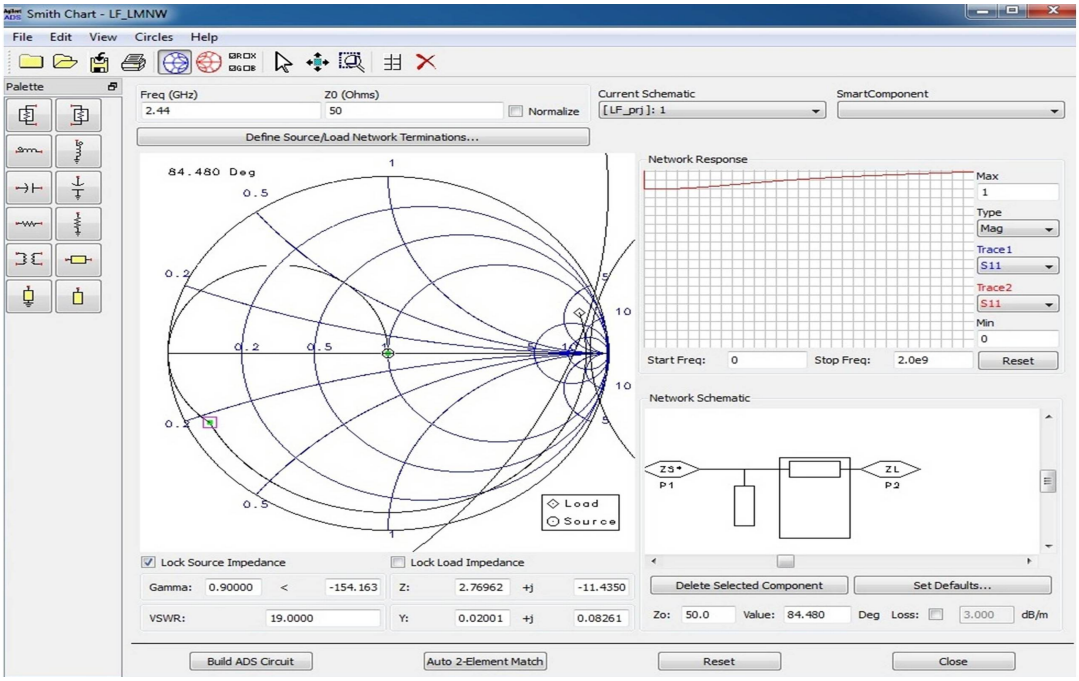

Figure 4.17: Matching network design using smith chart utility in ADS for 2.44 GHz.

As seen from Fig. 4.17 and 4.18, a great deal of flexibility is available in the selection of the reflection coefficient for the input matching network. Theoretically, any Γ_S residing inside of the stability circle should satisfy our requirements because S_{11} and S_{22} are greater than unity. In practice, however one has to choose Γ_S in such a way that it maximizes the output reflection coefficient. Values of reflection coefficients are calculated in such a way that it satisfies oscillation condition. Table 4.18 provides the calculated value of reflection coefficients.

$$\Gamma_T = S_{22}^{-1} \tag{4.25}$$

The conversion of the electrical parameters of the transmission lines into physical

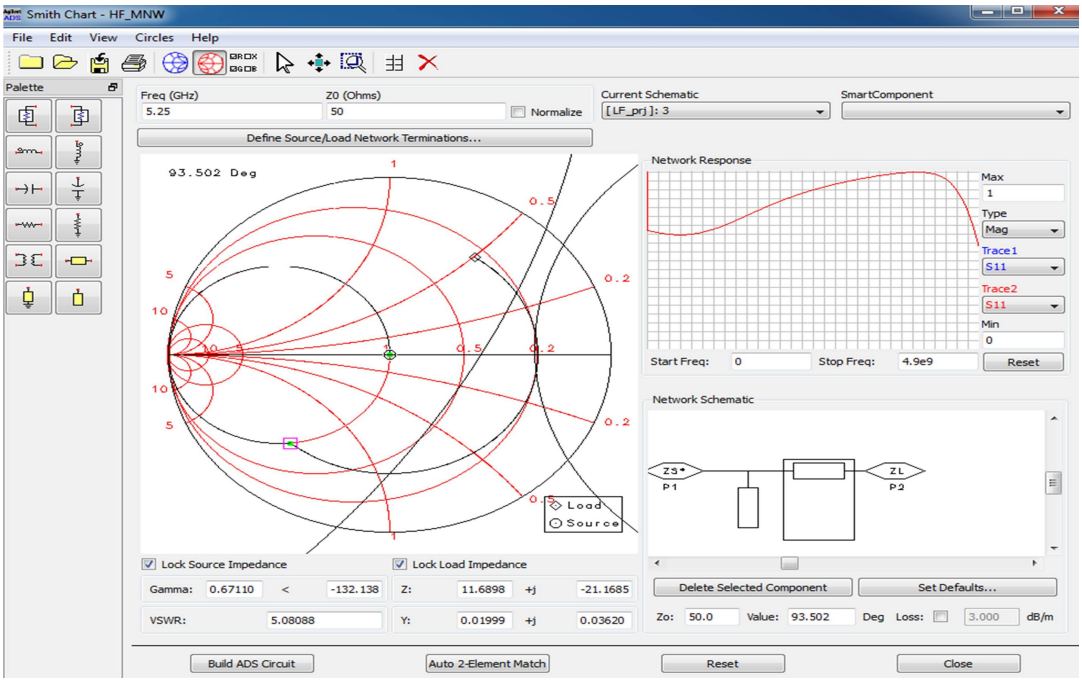

Figure 4.18: Matching network design using smith chart utility in ADS for 5.25 GHz.

dimensions is acomplished using *Linecal* tool in the *ADS-2009*. The dimensions of the TLs are computed for a *NH9320* substrate and are summarized in Table 4.19. A $50\ \Omega$ microstrip of 5 mm length and a taper of 1.5 mm length are connected to the output port side to minimize the fringing field effect.

Table 4.18: Reflection coefficients for matching network design

Frequency (GHz)	Γ_T
2.44	$0.90\angle 14.797$
5.25	$0.671\angle 54.867$

Table 4.19: Dimensions of the matching network

Frequency (GHz)	Z_0	Effect	Electrical Length	Width (mm)	Length (mm)	Optimized Length(mm)
2.44	50Ω	Inductive	84.480^o	3.64	18.05	10.12
		Capacitive	103.610^o		22.05	21.38
5.25	50Ω	Inductive	93.502^o	3.68	9.16	5.92
		Capacitive	118.920^o		11.66	15

4.4.4 Design of Resonator Network

As the oscillator design uses the small signal S-parameters and Z_{IN} becomes less negative with building up of oscillator output, it is necessary to choose Z_L so that $Z_L + Z_{IN} < 0$. Otherwise, the oscillations will cease when the increasing power increases Z_{IN} to a point where $Z_L + Z_{IN} > 0$. In general, a value of Z_L is chosen such that

$$Z_L = \frac{-Z_{IN}}{3}; \quad X_L = -X_{IN} \tag{4.26}$$

The resonators are realized by using open stub TL and estimated on the basis of Equations 4.27 and 4.28 as

$$\theta = tan^{-1}[\frac{X_S}{Z_0}] + 90.....ForPossitiveReactivePart \tag{4.27}$$

$$\theta = tan^{-1}[\frac{Z_0}{X_S}].....ForNegativeReactivePart \tag{4.28}$$

The reactive part of Z_L is chosen to resonate the circuit. Table 4.20 summarizes the details of the resonator design.

Table 4.20: Details of resonator Design

Parameter	$2.44\ GHz$	$5.25\ GHz$
$Z_{IN}(\Omega)$	$-43.912 - j260.9$	$-23.296 - j107.945$
$Z_L(\Omega)$	$14.637 + j260.9$	$7.765 + j107.945$
Electrical Length	169.15^0	155.146^0
Physical Length (mm)	36	15.65
Physical Width (mm)	3.64	3.68
Optimised Length (mm)	33	9

4.4.5 Harmonic Balance Simulation

The next step is to perform a harmonic balance simulation to predict oscillator characteristics, i.e. the output power spectrum and phase noise performance at both the frequencies. *OscPort* is an ADS probe component is used to calculate the oscillator waveform using a harmonic balance simulation. It calculates the large signal steady state form of the oscillatory signal. The resulting frequency spectrum and corresponding phase noise is shown in Fig. 4.19, 4.20 and 4.21.

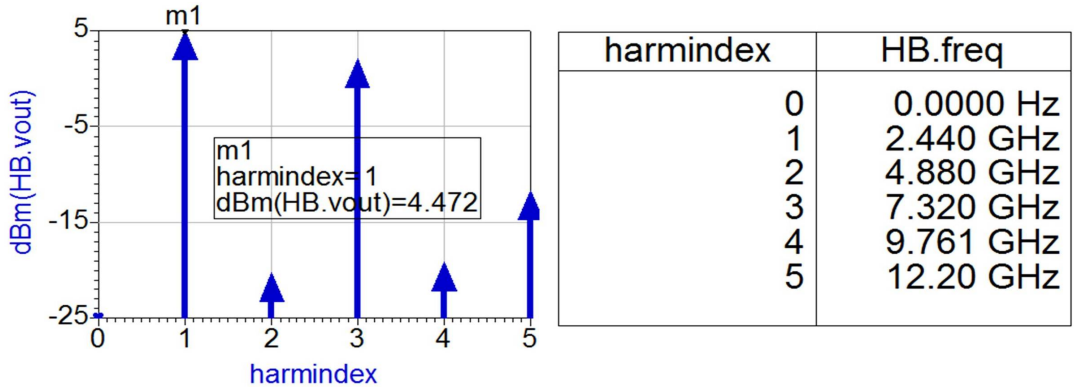

harmindex	HB.freq
0	0.0000 Hz
1	2.440 GHz
2	4.880 GHz
3	7.320 GHz
4	9.761 GHz
5	12.20 GHz

Figure 4.19: Simulation performance of the oscillators at 2.44 GHz.

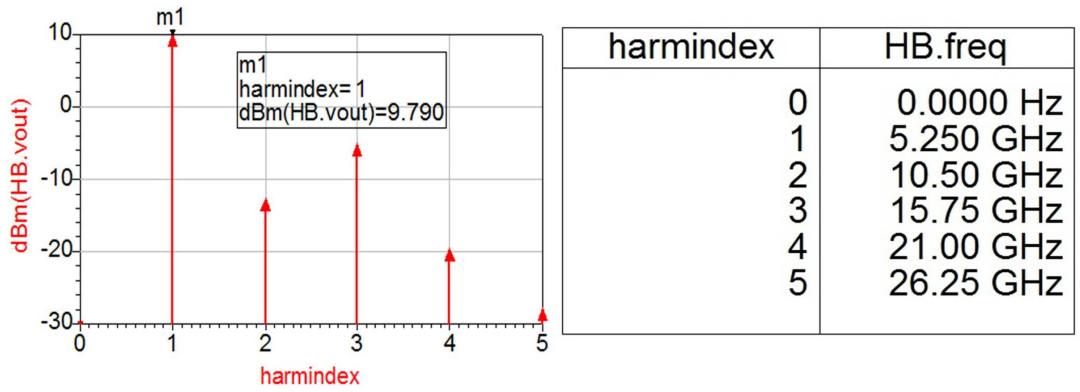

harmindex	HB.freq
0	0.0000 Hz
1	5.250 GHz
2	10.50 GHz
3	15.75 GHz
4	21.00 GHz
5	26.25 GHz

Figure 4.20: Simulation performance of the oscillators at 5.25 GHz.

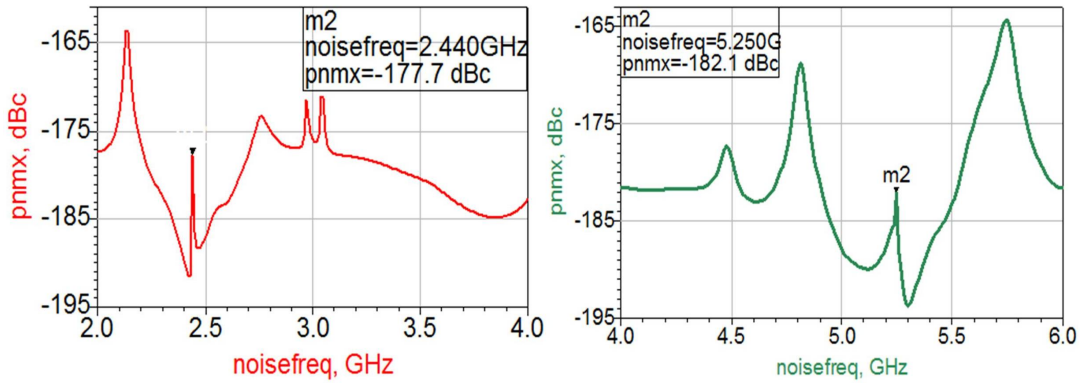

Figure 4.21: Simulation Phase noise response of the oscillators.

4.4.6 Measurement Results

Based on the analysis from section 4.4.1 to 4.4.5, a fabricated prototype of the proposed oscillators is devised. Further, measurement of these oscillators is carried out with *Agilent Filedfox Spectrum Analyzer (100 MHz to 6 GHz)*. Fig. 4.22 depicts the measurement setup. The fabricated prototype of the proposed oscillators are shown in 4.23 and 4.24. The measured power spectrum of the oscillators is depicted in Fig. 4.25.

Figure 4.22: Measurement setup.

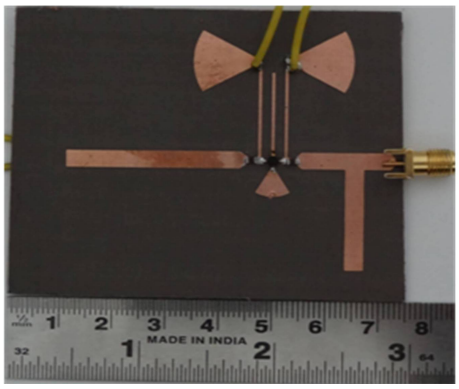

Figure 4.23: Fabricated prototype for 2.44 GHz band.

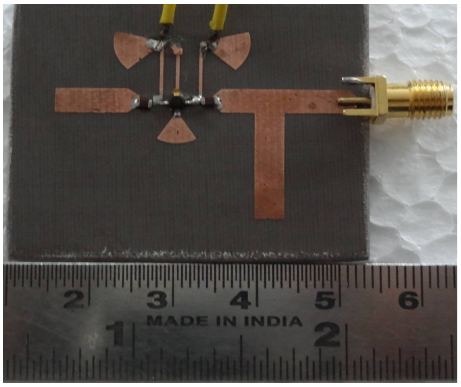

Figure 4.24: Fabricated prototype for 5.25 GHz band.

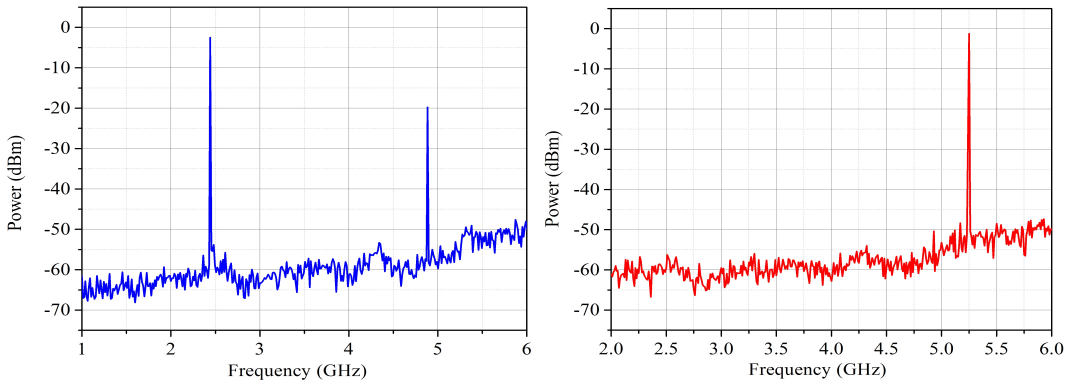

(a) (b)

Figure 4.25: Measurement power spectrum at : (a) 2.44 GHz (b) 5.25 GHz.

The phase noise of the oscillators had been calculated by using the relation [120]:

$$P_{NOISE} = P_{SB} - P_C - 10.log_{10}(RBW)dBc \tag{4.29}$$

where P_{SB} = Sideband power in dB at an offset of 100 KHz, P_C = Carrier Power in dB; and RBW = Resolution bandwidth of the spectrum analyzer in MHz. Considering the losses incurred due to the measurement setup and tolerance of the fabrication process, the carrier power is assumed to be 0 dBm along with a RBW of 200 MHz. Table 4.21 summarizes the simulated and measured phase noise of the oscillators at 2.44 GHz and 5.25 GHz.

Table 4.21: Phase noise calculation

Frequency (GHz)	P_{SB} dB	Simulated phase noise(dBc)	Measured phase noise (dBc)
2.44	-46	-177.7	-109
5.25	-43	-182.1	-106

4.5 Conclusions

This part of the thesis describes the design of a concurrent dualband WPD to operate simultaneously at 2.44 GHz and 5. 25 GHz. The aim is to have a compact low loss circuit as WPD which is a critical element in the front end design as an interconnect. Further, a concurrent dualband LNA is designed to operate at 2.44 GHz and 5.25 GHz. The design is incorporated with a standard HMIC technique and using *ATF-36163* (*p*-HEMT) active device. Measured performance of the fabricated LNA exhibits the required dualband response with a wideband rejection in between the desired band. A 2.44 GHz and 5.25 GHz oscillator is also designed to have a compact source for the proposed NIVSD sensor to be handheld.

Chapter 5

Characterization of a Concurrent Dualband NIVSD Sensor

This chapter presents details of experimental validation of the proposed concept. In this direction, the proposed concept is first verified using a Vector Network Analyzer (VNA) as a transceiver element. Then, the measurement setup is operated simultaneously at the designated operational bands. Finally, a PCB is devised from indigenously comprehended concurrent dualband components and commercial ICs such as SMD GaLi-24+ power amplifier (PA) *[See Appendix-D]* and SMD SYH 63LH+ mixer *[See Appendix-E]*. The baseband signal processing is carried out to extract the desired signal. The block diagram of the proposed non-invasive vital sign detection sensor is shown in Fig 5.1. The proposed sensor works on the Doppler principle. It transmits

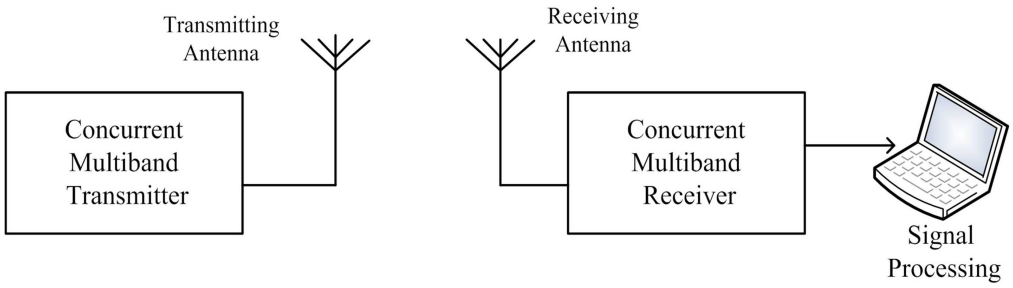

Figure 5.1: Block diagram of the proposed NIVSD sensor.

a 2.44 GHz and 5.25 GHz carrier signal simultaneously directed towards the human subject under test. The received signal consists of the additional information of human chest disarticulation modulated onto the carrier. The desired information of the human respiration and heartbeats can then be obtained from the baseband signal via proper signal processing.

5.1 The Design Considerations

To design a successful NIVSD sensor system, criteria such as transmitted power, null point consideration, radar range, safety factor, should be taken into account.

5.1.1 Safety Factor (S)

Since the proposed sensor is used in the detection of human vital signs using RF signals, in many applications it is necessary to ensure that the RF exposure is within a safe limit. Excessive RF exposure may be hazardous to the human being [121]. According to the IEEE RF safety standards [122], at the designated operational bands of the proposed system, the maximum EM radiation density levels up to 10 W/m^2 is considered as safe. The safety factor(S) is estimated as

$$S[\frac{W}{m^2}] = [\frac{P_T G_T}{4\pi L^2}] \tag{5.1}$$

where P_T = Radiating power in dBm, G_T = Antenna gain in dBi, L = Distance between the antenna and the human subject in meters.

5.1.2 Transmitted Power

The proposed system may be employed for human vital sign detection for continuous and longer duration such as patient monitoring in hospitals and for shorter duration in applications such as identifying life under debris. In the first case, the use of PA is

not advised because it is the most power consuming element whereas for such applications, the power level must be as low as possible. In the second case, the detection sensitivity is the primary goal. Moreover, the monitoring and detection process is carried out for a shorter duration. Hence, use of a power amplifier will be beneficial in such applications. In addition, the EM radiation must satisfy the safety considerations narrated in *Section 5.1.1* above.

5.1.3 Optimum and Null Point consideration

Direct conversion architecture is adopted to realise the proposed system. It is often adopted in the Doppler radar detection system due to its simple architecture with single tone transmission and one step conversion [1, 7, 53, 62–64]. As discussed in *Section 1.2.2.3*, the null point problem may severely degrade the detection reliability at high frequency in a single band system used for vital sign sensor application. With concurrent dualband operation, it is guaranteed that an optimal point in the detection process always exist for at least one band. Further, the effect of null point detection can be minimised by incorporating reconfigurability or in-band tunability to select an optimum frequency ratio for the detection process. *(Ref. Section 5.2.1).*

5.1.4 Radar Range Equation

In radar operations, the detection range of radar is related to the transmitter, receiver, antenna, the operational environment and the target characteristics. This is also the best tool to understand and study the factors affecting the performance of the system. The radar range equation is given as

$$P_R = P_T[A\frac{G_T G_R}{4\pi}(\frac{\lambda}{4\pi R^2})] \tag{5.2}$$

where P_t is the transmitted power (dB); A is the radar cross section area (m^2), λ is the wavelength of the signal to be transmitted (m). G_T and G_R are the gains of the transmit / receive antennae (dBi). From this equation, one can easily infer that for

long range of transmission, the transmitted power should be large and the antenna must be highly directive.

5.1.5 Receiver Noise Figure

For cascaded subsystem stages of the receiver, the overall noise figure (NF) is calculated by *Friis* equation is given below

$$NF = 1 + (NF_1 - 1) + \frac{NF_2 - 1}{A_1} + \frac{NF_2 - 1}{A_1 A_2}..... \tag{5.3}$$

Here, A_1 and A_2 are the gains of two stages, NF_1 and NF_2 are the noise figures of the subsequent stage.

5.1.6 Link Budget

Link budget calculation is an effective cost function which provides the ability of the system to detect signals over a distance. For estimation of the link budget over a particular distance, free space path loss *(FSPL)* plays a pivotal role and may be estimated as

$$FSPL = 20log_{10}[\frac{4\pi L}{\lambda}] \tag{5.4}$$

where L is the distance from the transmitter(in meter) and $\lambda(c/f)$ is the wavelength of the signal. Based on the *FSPL*, the link budget or link sensitivity may be estimated as

$$P_{RX} = P_{TX} + G_{TX} - L_{TX} - L_{FS} + G_{RX} - L_{RX} \tag{5.5}$$

where P_{TX} = Transmitted output power in dBm, G_{TX} = Transmitter antenna gain in dBi, L_{TX} = Transmitter losses in dB, L_{FS} = Free space losses in dB, G_{RX} = Receiver antenna gain in dBi, L_{RX} = Receiver losses in dB.

5.1.7 Receiver Sensitivity

It is the minimum signal level within the acceptable signal-to-noise ratio (SNR) that can be detected by the system.

$$R_S = -174dBm/Hz + NF + 10logB + SNR \tag{5.6}$$

where NF is the noise figure obtained in Eq. 5.3 and B is the system bandwidth.

5.2 The Measurement Setup

To validate the proposed concurrent dualband NIVSD, an ADS simulation has been carried out using the measured S-parameters of the subsystems and standard ADS library components. Fig. 5.2 shows the simulation setup to decide the validity of the proposed concept. Here, the human being under test is modeled with the *'RESP*' and *'HB*' signals and two-phase modulators, operating at 2.44 GHz and 5.25 GHz. The *'RESP*' and *'HB*' signals are obtained by the standard available source with ADS and were kept at 0.33 Hz and 1.2 Hz, respectively. Individual RF sources have been used from the ADS library. Fig. 5.3 shows the received signals at individual band along with the standard human vital sign signal. From Fig. 5.3, it is clear that though the detection is carried out at different bands, the position of desired signal peak doesnot change due to concurrent multiband operation. This is the significant advantage of the proposed system. Hence, without varying the measurement conditions, the advantages of lower and higher band operation can be achieved.

Following the simulation validation, an initial measurement has been carried out using a VNA and two concurrent dualband microstrip patch antennae in a noisy environment. *Agilent Fieldfox RF Analyzer (N9912A: 2 MHz - 6 GHz)* has been used as a transceiver element. Fig. 5.4. shows the initial measurement setup using a VNA. The human subject is positioned at a distance of 1 m away from the antennae. The two antennae are distanced 17 cm apart. The samples are taken for 52 $seconds$ from

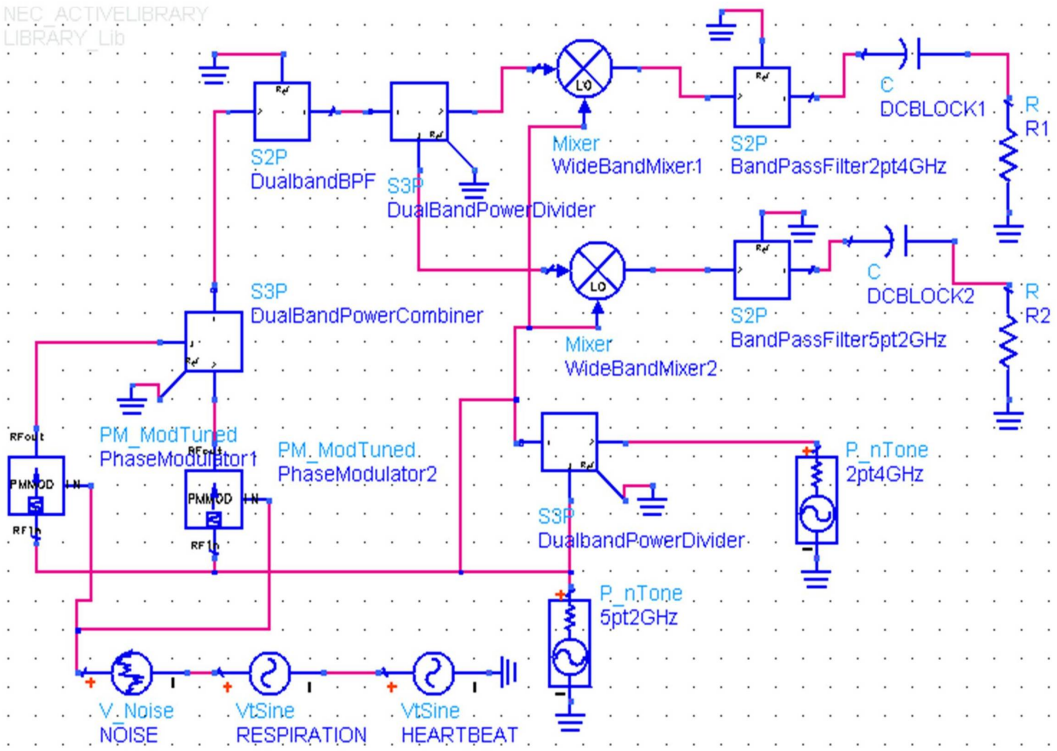

Figure 5.2: ADS simulation setup for proposed NIVSD sensor [123].

a human subject with normal physique. Real time readings of heartbeat and respiration rates from the VNA are captured and processed using a MatLab program. The sampling frequency is kept at 3.2 Hz since the maximum frequency of heartbeat is generally 1.5 Hz.

The phase information in forward transfer gain S_{21} is captured from the VNA. The phase variation frequencies can be interpreted as the heartbeat and respiration rate. FFT and WT are applied on these signals to detect the desired frequency components of the heartbeat and the respiration rate. Fig. 5.5 and Fig. 5.6 shows the FFT and WT spectrum respectively for the desired signal. It is observed that at lower frequency, i.e. at 2.44 GHz, the noise aspect is less but at the cost of detection sensitivity. On the other hand, at higher frequency i.e. at 5.25 GHz, the detection sensitivity is increased but with the tag of noise.

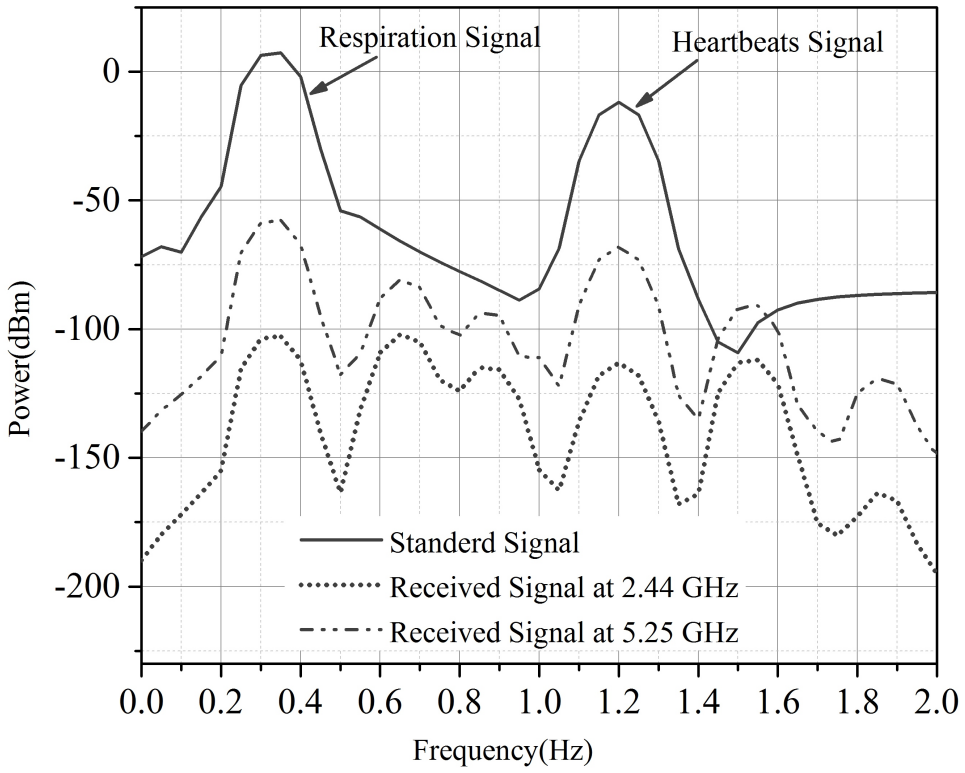

Figure 5.3: ADS simulation setup result.

From Fig.5.5 and Fig.5.6, it is clear that even though the measurement is carried out at different bands, the detected respiration and heartbeat signals are not distorted. This is because the measurements are carried out concurrently at two bands. The resultant FFT spectrum shows that the desired signals are present along with their harmonics and noise components. Furthermore, many frequency components lie in the allowable heartbeat range. This may be because the third, and the fourth order harmonics of the respiration signal overlap with the heartbeat signal. Here, it is impossible to sense the exact heartbeat signal. This difficulty may be overcome by applying the correlation between the signals obtained from the two bands. With WT, it is easier to detect the human vital signs [124]. Fig. 5.7 shows the correlation spectrum for FFT and WT signals.

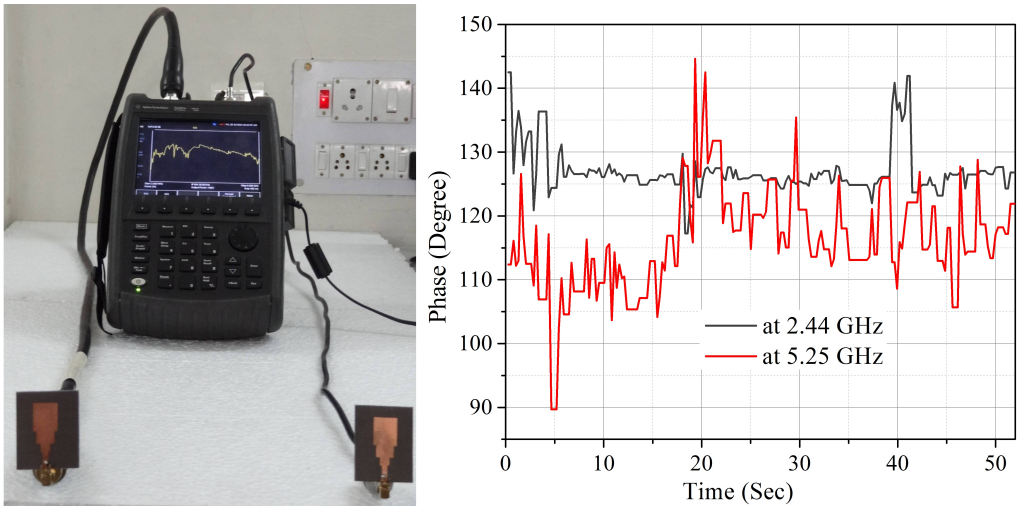

(a) (b)

Figure 5.4: VNA characterization of the proposed concept : (a) Measurement setup (b) Measured phase variation information.

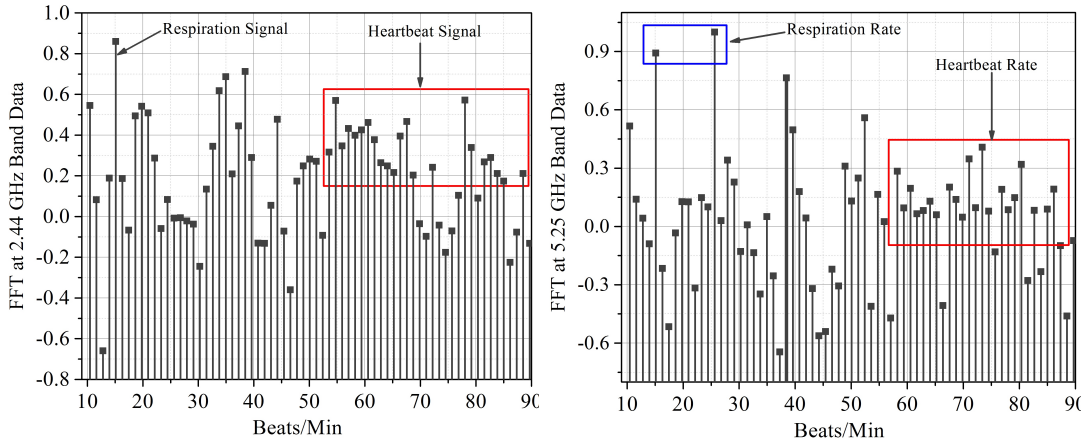

(a) (b)

Figure 5.5: FFT spectrum of heartbeats and respiration at (a) 2.44 GHz and (b) 5.25 GHz.

After application of correlation between the individual band signals, it is seen that the estimation of the desired signals can be carried out effectively. FFT correlated spectrum shows that the respiration rate is 15 beats per minute, and the heartbeats are at the rate of 61 beats per minute.

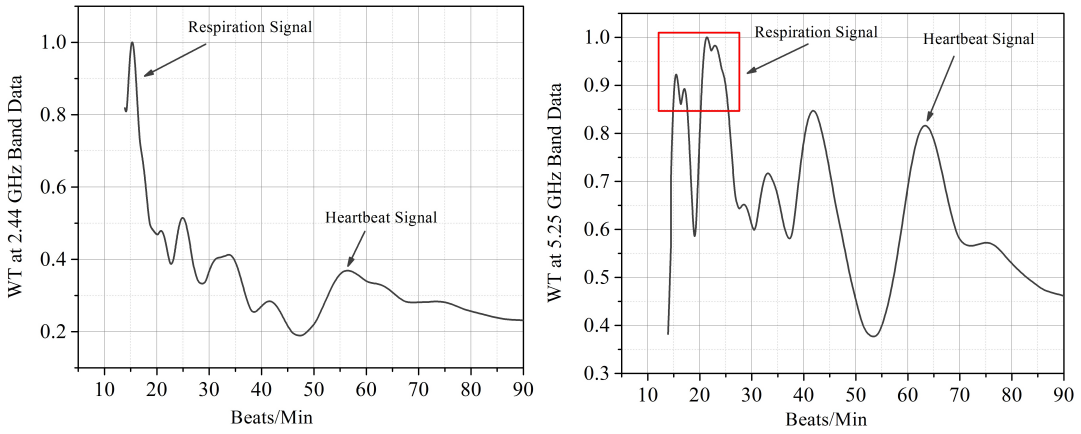

(a) (b)

Figure 5.6: WT spectrum of heartbeats and respiration at (a) 2.44 GHz and (b) 5.25 GHz.

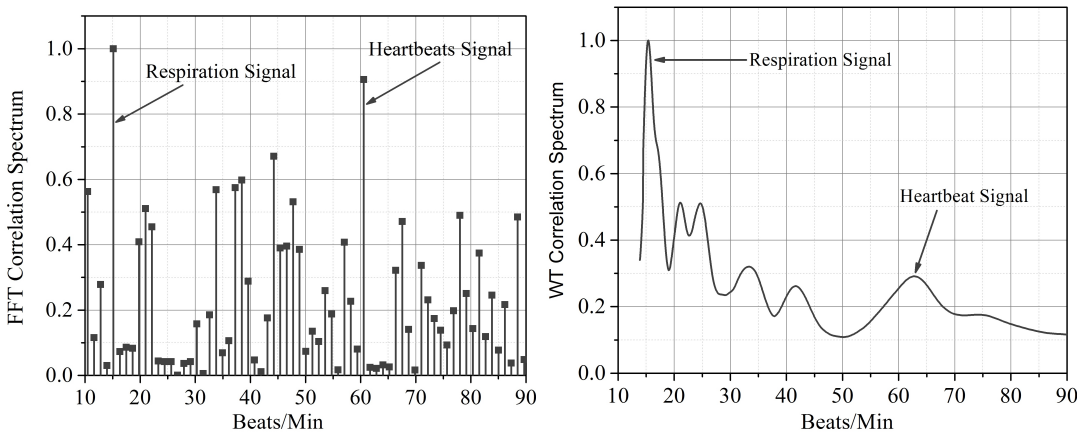

(a) (b)

Figure 5.7: Correlation spectrum for human vital sign detection: (a) FFT (b) WT.

The ambiguity in heartbeat detection from individual FFT and WT spectrum is visibly eliminated in the correlated spectrum. In the single band RF systems, switching is required to extract the advantage of multiband operations. Due to this, some delay is incorporated between the two consecutive measurements.

It is the normal tendency for heartbeats and respiration rate of a human being to change over time. Hence, it is possible that inconsistent respiration rate and heartbeat signals

be obtained after correlating the signals obtained from the switched mode operation. However, the measurements carried out by our proposed concurrent dualband setup have shown a uniform detection of signals at both the bands. This is the significant advantage of a concurrent dualband RF system over the existing single band systems for vital sign detection. Additionally, the individual subsystems can be customized to operate at dualband concurrently via hardware sharing. This will minimize the hardware requirement as compared to the parallel mode of multiband operation.

With these initial confirmations, a more comprehensive measurement setup has been devised for the further analysis. The setup was made up of indigenously developed dualband subsystem to operate at 2.44 GHz and 5.25 GHz band and few of-the-self-laboratory equipments. Fig.5.8 shows the conceptual diagram of the proposed system.

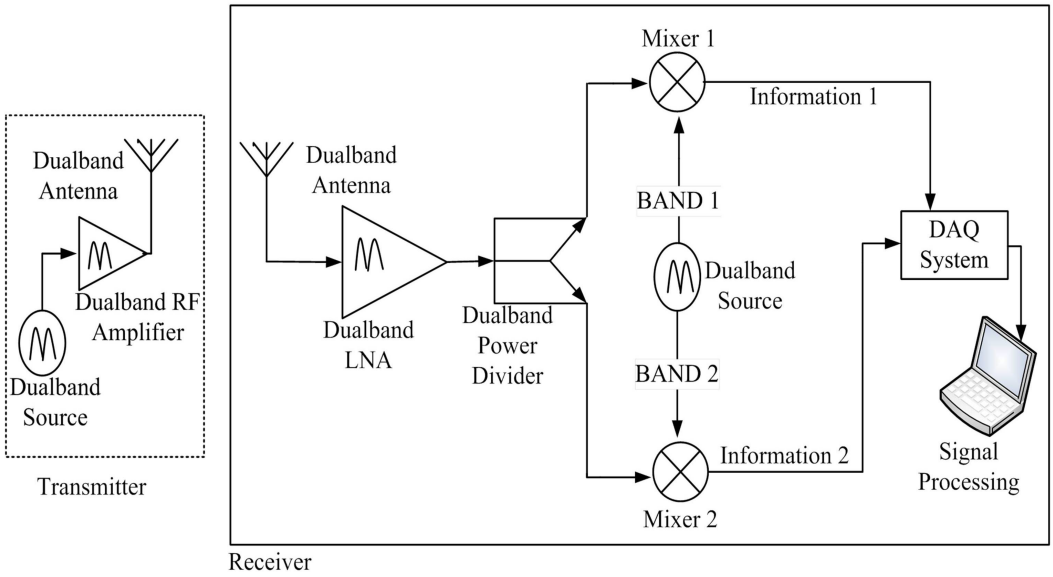

Figure 5.8: Conceptual diagram of proposed NIVSD system [125].

The measurement setup shown in Fig.5.9 consists of the laboratory equipments and our own custom designed dualband subsystems. Here, two RF source *(R&S SMR20:10 MHz to 20 GHz)* are used to provide the required RF signal in the transmitter section. The power level is kept at 10 dBm. A dualband signal is fed to the transmit-

ting antenna with the help of fabricated dualband Wilkinson power combiner/divider (WPD) [126]. Measured result shows that it introduces an approximate insertion loss of $-3.4dB$ and $-3.8dB$ at 2.44 GHz and 5.25 GHz band, respectively. Note that two identical dualband patch antennae are used for transmission and reception purpose.

Figure 5.9: Measurement setup for NIVSD using indigenous and laboratory equipment [125].

Further, on the receiver side, a 2.44 GHz and 5.25 GHz concurrent dualband LNA [127] is used to boost the received signal level. For the purpose of down conversion, two single band mixers from *'Mini circuits'* have been used to operate at individual bands. *'ZEM-4300MH'* mixer is used at 2.44 GHz. It has 8.5 dB conversion loss and 13 dBm power level. For 5.25 GHz, a *'ZMX-7GR'* mixer with 8.5 dB conversion loss and 17 dBm power level has been used. The individual mixers have been fed with the local oscillator frequencies, i.e. 2.44 GHz and 5.25 GHz to obtain the baseband signal. This baseband signal has been applied to the data acquisition (DAQ) system. An *'IoTECH DAQ-54'* system has been used with a sampling rate of 37 Hz for digitizing the baseband signal. The digitized baseband signal has been further processed using MATLAB to retrieve the required knowledge about the heartbeat and respiration sig-

nals. The losses due to cables and connectors have an average value of 6.55 dBm and 5 dBm at the transmitter and receiver, respectively.

The samples are taken for 120 seconds at the aforementioned sampling rate. The observations are carried out on a human being with normal health. The human subject is positioned at a distance 0.5 m. [Fig. 5.10(a)] and 1 m [Fig. 5.10(b)] from the transceiver. It is evidenced from Fig.5.10 that after FFT of the desired band signals, multiple peaks are found to be present around 20 Hz and 70 Hz. These peaks are due to the noise and environmental interference. Hence, it becomes difficult to identify the exact respiration and heartbeat signals using a particular single band and may lead to the incorrect detection of human life. This ambiguity is out weighted by applying correlation between the two signals. The cross-correlation plot clearly predicts the respiration and heartbeat signals. The signals at 22 Hz and 72 Hz are the required respiration and heartbeat signals. It is also apparent that though the measurements are carried out at different bands, the detection sensitivity is not altered. This is due to the concurrent multiband operation. In addition, the correlated signal is more sensitive in comparison to the individual bands and provides better accuracy.

When the distance between the human subject and the transceiver is increased, the detection sensitivity decreases. This is due to reduced received power strength. In the current measurement setup, the PA and intermediate frequency amplifier (IFA) were not used. The detection sensitivity can be easily improved by employing a PA at the transmitter end and an IFA at the receiver end. With increased detection sensitivity, it is possible to detect life even under metal structures or other impediments.

Further, the detection of human respiration and heartbeat signal was also carriedout by using an omni-directional patch antenna array, as described in *Section (3.2.2)*. Fig. 5.11 shows the FFT spectrum for NIVSD, using an omni-directive concurrent dual-band patch antenna array, with human subject was at a distance of $0.5m$ from the measurement setup.

Comparing Fig. 5.10(a) and Fig. 5.11, it is confirmed that the noise content in the

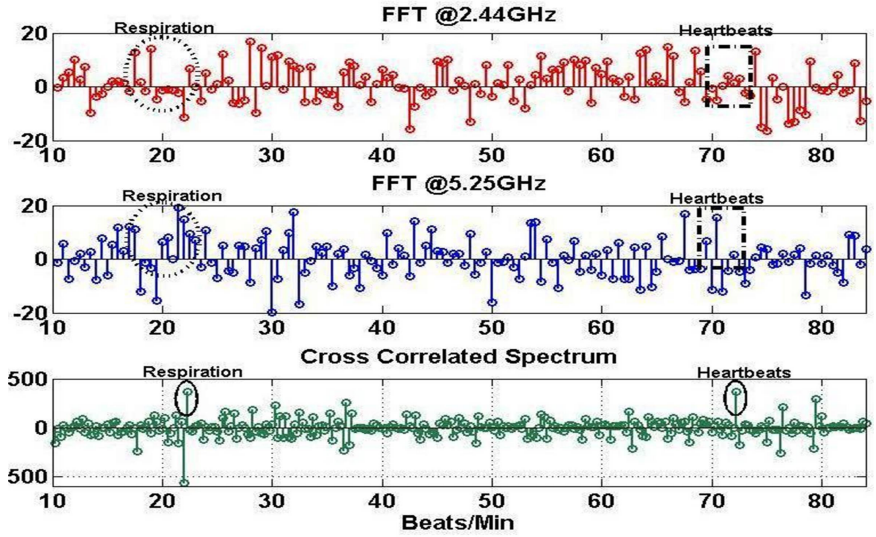

(a)

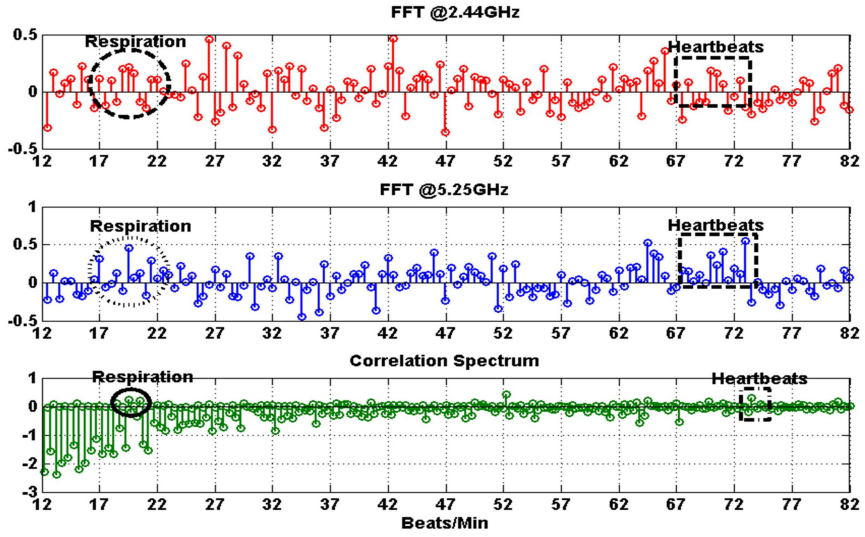

(b)

Figure 5.10: FFT spectrum from measurement setup at: (a) 0.5 m (b) 1 m.

detected signal is more when an broad-side directive antenna configuration is used. Hence, in order to improve the detection range and sensitivity, a directive antenna with high gain is recommended. The performance of the proposed measurement setup may be analyzed by the link budget as a cost function.

The power levels have been measured by using power meter *(R&S NRVS1020)* at each

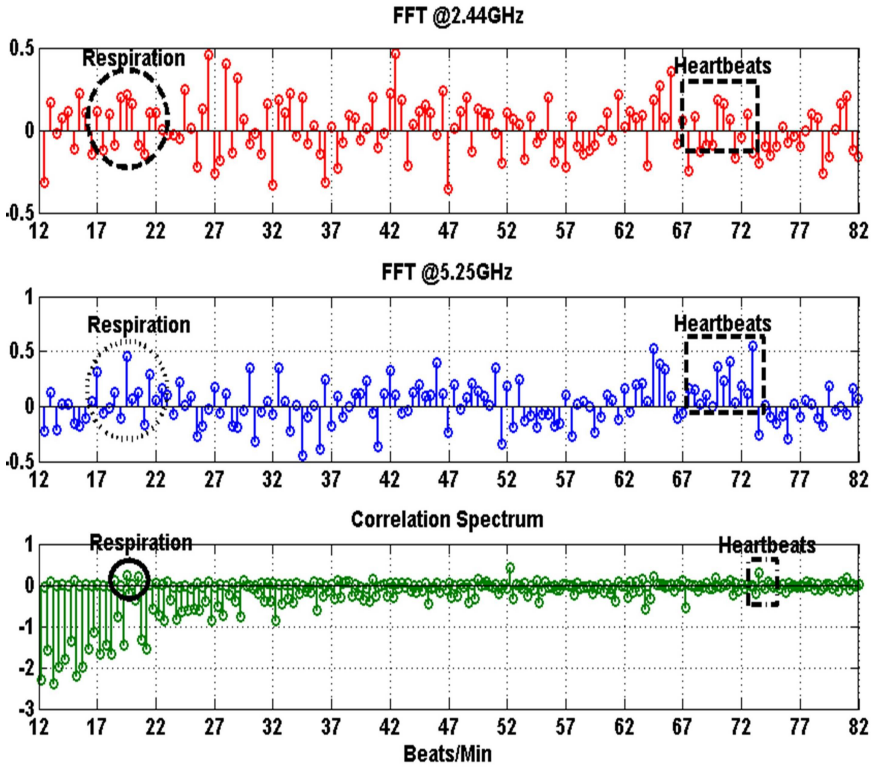

Figure 5.11: FFT spectrum for NIVSD using an omni-directive concurrent dualband patch antenna array at $0.5m$ distance.

Table 5.1: Measured output power level

Frequency (GHz)	At WPD (dBm)	At transmitter Antenna (dBm)	At Receiver Antenna (dBm)
2.44	5.18	5.5	-25.5
5.25	3.42		

stage of the setup. Table 5.1 summarizes the power levels measured at the different stages of the RF system. From the empirical relations, it is estimated that the minimum free space loss at the centre frequency is 44.2 dBm. From Eq. 5.7,the link

budget analysis of the measurement setup is given as

$$P_{RX} = P_{TX} + G_{TX} - L_{TX} - L_{FS} + G_{RX} - L_{RX} = -25.7dBm \quad (5.7)$$

The safety factor (S) related to EM radiation for the proposed RF system may be estimated with the help of Eq. 5.1. For the measurement setup it is estimated as 87 $\mu W/m^2$. The estimated electromagnetic radiation (EMR) value is much lower than the maximum density level provided by IEEE Standards (10 W/m^2) [122]. With this analysis, our own customized PCB for the proposed sensor had been fabricated and further analyzed in the following Sections.

5.2.1 Effect of Reconfigurability

Table 5.2: Effect of reconfigurability

Sample No.	Band 1 (GHz)	Band 2 (GHz)	T_x Power (dBm)	R_x Power (dBm)	EMR (mW/m^2)
1	2.4	5.15	11.90	-42.54	35.66
2	2.4	5.25	12.36	-43.91	39.63
3	2.4	5.35	12.90	-31.62	44.86
4	2.44	5.15	11.62	-37.20	33.40
5	2.44	5.25	12.15	-32.70	37.68
6	2.44	5.35	12.71	-30.75	42.95
7	2.48	5.15	11.34	-36.10	31.33
8	2.48	5.25	11.85	-36.50	35.23
9	2.48	5.35	12.41	-29.15	40.80

The selection of proper frequency ratio plays a key role for the accuracy and sensitivity of a concurrent multiband RF system employed for NIVSD. The performance

of such concurrent multiband RF systems can be further improved by incorporating the concept of reconfigurability. It is advantageous in selecting optimum frequency ratio for minimum EMR; which is essential for the safety of human subject under test as well as the operator of the instrument. This novelty can be achieved by designing the individual reconfigurable subsystems. The proper selection of frequency ratio provides two fold advantage over the static multiband RF radios. Firstly, the noise performance and sensitivity can be improved and secondly the improved accuracy can be obtained in the detection of tiny human vital sign signals. Also, the problem of null point detection can be eliminated by selection of an optimal frequency ratio for the specific application. All these features can be obtained via multiband RF systems with the incorporation of a varactor diode as a tuning element. By controlling the bias voltage of the varactor diode desired tuning can be achieved. To study the effect of reconfigurability, the output power at various stages is measured with the help of a power meter (R&S NRVS1020). Table 5.2 provides the measured performance of the effect of frequency reconfigurability. It clearly shows that the performance can be improved by the reconfigurable operation as the user can decide the best frequency ratio in terms of transmitted power or EMR for a particular situation or operation.

5.3 The Sensor Characterization as an Integrated System

The proposed sensor is further validated on a single substrate with relative dielectric constant of 3.2 and height of *60 mil* with a loss tangent of 0.0024 with substrate height of $18\mu m$. The sensor is made up of indigenously fabricated concurrent dualband subsystems and some commercial components and laboratory equipments. Table 5.3 summarizes the classification of the subsystems used in the proposed sensor. Fig.5.12 shows the fabricated prototype of the proposed concurrent dualband RF sensor for NIVSD application.

Table 5.3: Subsystems of the proposed RF sensor

Sr.	Subsystem	Manufacturer	Specification
1	Source I & II	Indigenous Design	Operation at 2.44 GHz and 5.25 GHz
2	Power Amplifier (GaLi-24+)	Minicircuits	Operation from DC to 6 GHz
3	WPC/WPD	Indigenous Design	Concurrent dualband at 2.44 GHz and 5.25 GHz
4	Antenna	Indigenous Design	Concurrent dual-band operation at 2.44 GHz and 5.25 GHz with directive pattern
5	LNA	Indigenous Design	Concurrent dualband operation at 2.44 GHz and 5.25 GHz
6	Mixer I & II (SYM-63LH+)	Minicircuits	IF response from DC to 1000 MHz
7	DAQ-54	IoTECH	22 bit resolution,Input Voltage = -10 VDC to 20 VDC

5.3.1 Link Budget Calculation

The measurements were carried out in an indoor conditions with the distance between the antenna and the human subject varying between $0.5\ m$ and $3\ m$. The experiment is carried out with three different antenna configurations such as concurrent dualband with a single patch, omni-directional patch antenna array and a direction patch antenna array. The transmitter and receiver losses are estimated by considering the contribution of individual subsystem, in terms of its gain or NF, in the system. Table 5.4 gives the detail parametric analysis data in each of these case.

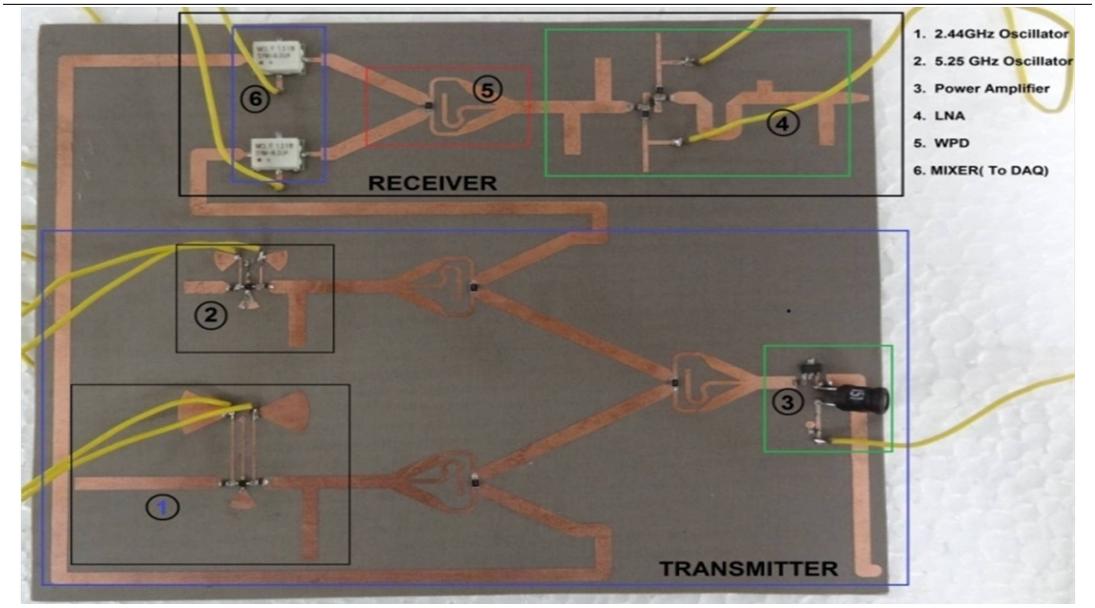

(a)

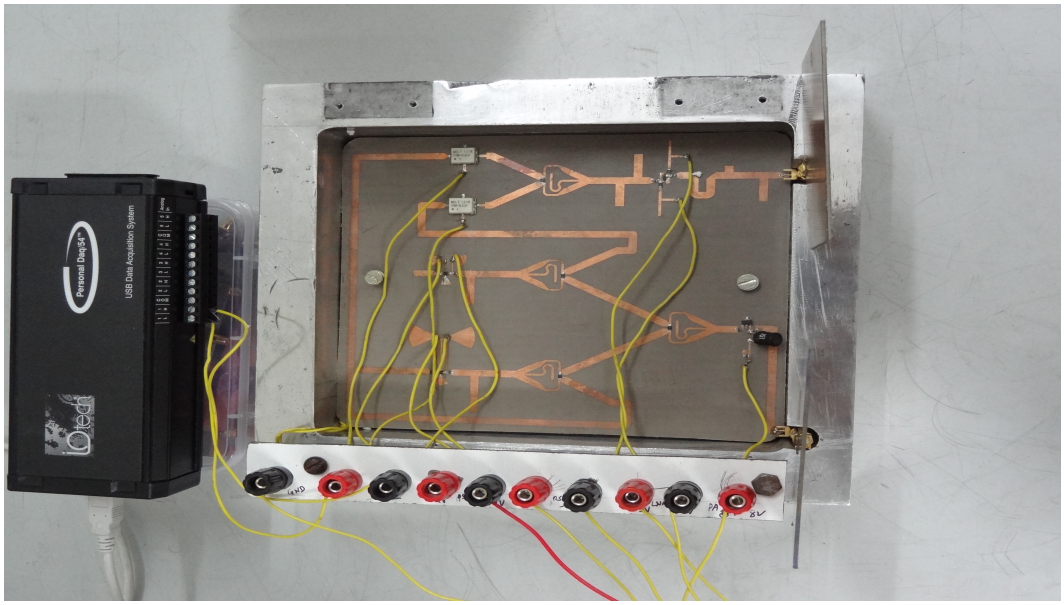

(b)

Figure 5.12: Characterization of the proposed concurrent dualband RF NIVSD sensor (a) Fabricated PCB prototype (b) Prototype with casing.

Table 5.4: Link budget performance of the proposed NIVSD sensor

Parameter		Antenna array (Directive)	Antenna array (Omni-directive)	Single patch
Antenna Gain (dBi)		7.5	5.5	2.5
Transmitter losses (dBm)		10.41		
Receiver losses (dBm)		8.81		
Path Loss (dBm)	At 0.5 m	44.13		
	At 1 m	50.15		
	At 2 m	56.17		
	At 3 m	59.70		
link Budget (dBm)	At 0.5 m	-38.35	-42.35	-49.05
	At 1 m	-44.37	-48.37	-55.07
	At 2 m	-50.39	-54.39	-61.09
	At 3 m	-53.92	-57.92	-64.62

5.3.2 Link Margin Calculation

To ensure proper working of the proposed NIVSD, its sensitivity analysis is very important. Fig. 5.13 shows the block diagram of the RF section of the proposed NIVSD system for sensitivity analysis. The diagram depicts the individual subsystems gain and NF contribution. With this measurement setup, it is observed that as the distance between the transceiver and the human subject under test increases the signal strength at the receiver end decreases considerably. The sensitivity analysis is carried out for a bandwidth of 3 Hz. The maximum heart rate varies significantly with the age [128] which is given by

$$HR_{MAX} = 205.8 - (0.685 \times age) \tag{5.8}$$

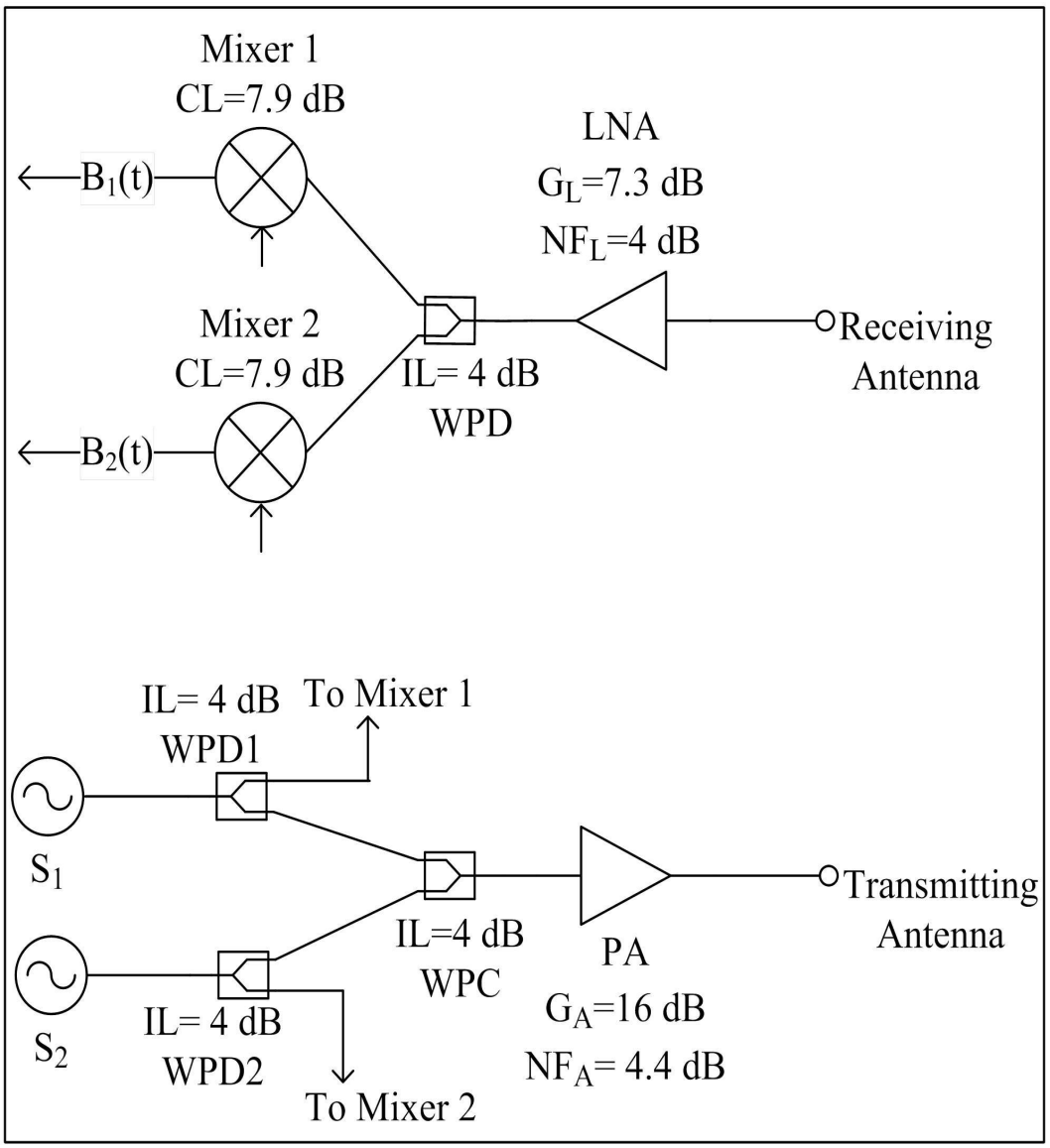

Figure 5.13: Block diagram of RF section of the proposed NIVSD system for sensitivity analysis.

A male with 33 years of age and normal physique has been kept under test. According to Eq. 5.8, the HR_{MAX} is $183BPM$ which is approximately 3 Hz. Table 5.5 provides the performance of the proposed system under different measurement conditions. With an output SNR of value as high as 20 dB, detection of very weak human vital sign is guaranteed. The link margin of the proposed system attain a minimum

value of 74dB with the help of a single patch antenna. This indicates that the proposed NIVSD can detect the human target accurately at considerable distance if the required link budget is less than 74 dB.

Table 5.5: Link margin analysis of the proposed NIVSD sensor

Parameter		Antenna array (Directive)	Antenna array (Omni-directive)	Single patch
Thermal Noise		$-174dBm/Hz$		
SNR		20 dB		
Sensitivity		$-138.62dBm$		
Received Power (dBm)	$At0.5m$	-38.35	-42.35	-49.05
	$At1\ m$	-44.37	-48.37	-55.07
	$At2\ m$	-50.39	-54.39	-61.09
	$At3\ m$	-53.92	-57.92	-64.62
Link Margin (dBm)	$At0.5\ m$	100.27	96.27	89.57
	$At1\ m$	94.25	90.25	83.55
	$At2\ m$	88.23	84.23	77.53
	$At3\ m$	84.70	80.70	74

5.3.3 Detection Range Analysis

The range of detection for this RF occupancy sensor is estimated with the help of the RADAR range equation as given in Eq. 5.2. Here, P_T = 10 dB, λ = 0.078 m and RADAR cross section (σ) = 0.01 [129]. The range is estimated with different antenna configurations. Substituting the gain *(G)* values in Eq. 5.2, the maximum distance of detection under free space condition and without any obstacle was calculated. Table 5.6 summarizes the detection range for the proposed sensor. the range may be further increased by using high gain antenna and LNA in the design architecture.

Table 5.6: Detection range of the proposed sensor

Antenna Configuration	Gain (dBi)	Detection Range ($meters$)
Concurrent dualband Single Patch	2.3	2.8
Concurrent Dualband Omnidirectional array	5.5	4
Concurrent Dualband Directional array	7.5	5

5.3.4 Safety Factor Analysis

From Eq. 5.1, the level of electromagnetic radiation (EMR) to which the human subject under test was exposed during the measurements with this sensor may be estimated. Table 5.7 summarizes the safety factor analysis with different types of antenna. It is evident from the values tabulated in Table 5.7 that this sensor is safe enough to be used for the detection of human vital signs since the amount of EMR is quite small and will never turnout to be hazardous to the human subject under test.

Table 5.7: Safety factor analysis*

Distance(Lm)	Antenna Configuration		
	Concurrent dualband single patch	Concurrent dualband omni-directive array	Concurrent dualband directive array
0.5	1.78×10^{-5}	1.11×10^{-5}	5.41×10^{-6}
1	4.45×10^{-6}	2.78×10^{-6}	1.35×10^{-6}
2	1.11×10^{-6}	6.95×10^{-7}	3.37×10^{-7}
3	4.49×10^{-7}	3.08×10^{-7}	1.5×10^{-7}

*: Measured in W/m^2

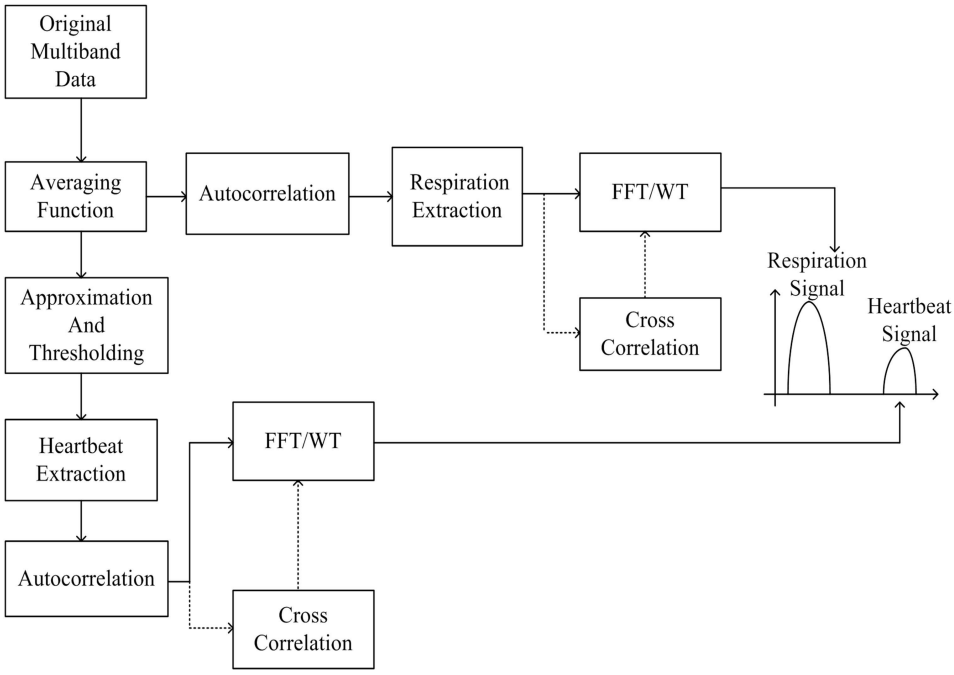

Figure 5.14: Proposed algorithm for baseband signal processing.

5.4 The Signal Processing

The performance efficiency of the baseband signal processing is the key for the success of an NIVSD system. As discussed in *Section 1.2.2.5*, many approaches had been reported in the literature and applied for the baseband signal processing. For the proposed NIVSD sensor, an algorithm for baseband signal processing is developed which is capable of retrieving the heartbeat and respiration rate accurately, even in a noisy environment. Fig. 5.14 shows the flow chart for the proposed algorithm. The simple FFT based signal processing method will no longer be useful when long distance measurement is to be carried out. The main constraint in the signal processing is the presence of enormous noise. Among the desired signals, respiration signal is strong as compared to the heartbeat.

The extraction of heartbeat is very important as it is weak in comparison to the respiration signal. Hence, special care needs to be taken while processing it. Initially,

individual dualband data has been averaged which helps to identify the central tendency of the data being processed. The averaging may be carried out as

$$y(t) = \frac{1}{T}\int_{t-T}^{t} x(t)dt \tag{5.9}$$

where *x(t)* is the input signal, *y(t)* is the averaged signal and T is the averaging interval. A two prong strategy is adopted to extract the respiration and heartbeat signals. First, the extraction of the respiration rate signal from the individual dual band data is carried out and the averaged time domain data is autocorrelated to minimize the noise content. Next, a frequency domain transformation is carried out to extract the respiration signal. Smoothening of this signal is achieved with the help of a BPF with pass band 0.1 Hz to 0.4 Hz. Finally, the individual dualband data is correlated to achieve a correct identification of the respiration signal. In the next stage, the averaged signal is processed for approximation to extract the heartbeats. Here, a linear approximation function is used for approximation and it is defined as

$$y_L(t) = x(t) - [a(t).x(t) + b(t)]dt \tag{5.10}$$

where a(t) and b(t) may be estimated using the relations

$$a(t) = \frac{E[xy] - E[X].E[Y]}{E[X^2] - (E[X])^2} \tag{5.11}$$

$$B(t) = \frac{E[Y]E[X^2] - E[XY]E[X]}{E[X^2] - (E[X])^2} \tag{5.12}$$

where $E[X], E[Y], E[XY]$ and $E[X]^2$ are the statistical moments calculated over the interval [(t -$\frac{T}{2}$)< t < (t + $\frac{T}{2}$ +1)]. By observing the approximated data, a threshold is selected to decide the heartbeat signals. The individual band data is autocorrelated to minimize the effect of the noise content. The individual band data is then passed through a BPF with a passband from 1 Hz to 3 Hz. A frequency-domain transformation is applied to the signals to analyze the individual band data. Further, a cross correlation is carried out on the dualband data to predict the exact heartbeats. It cancels out the uncorrelated signals from the individual dual band signals and retains only

the correlated signals. It provides the accurate prediction of human vital signs. The cross correlation may be obtained as

$$(fxg)(\tau) = \int_{-\infty}^{\infty} f^*(t)g(t+\tau)dt \tag{5.13}$$

In the entire analysis, along with the FFT, wavelet transform (WT) with *'morlet'* kernel is used to reinforce the detection result. According to the Eq. Eq.5.8,the bandwidth of the filter for the heartbeat detection is kept from 1 Hz to 3 Hz and that of respiration is kept from 0.1 Hz to 0.4 Hz. The wide range of the passband is selected to ensure the functionality of the system remain within a tolerable range. Fig. 5.15 demonstrates the FFT analysis of detected signals with the proposed sensor at a distance of $2meters$. Further, WT has been applied on the detected signals for analysis purpose. A similar response has been obtained which validate the proposed concept. Fig. 5.16 depicts the WT spectrum of the detected signals.

Table 5.8: Summary of NIVSD of the proposed RF sensor

Signal Processing Method	Respiration rate(BPM)	Heartbeat(BPM)
FFT	12	72.02
WT	12.04	72.24

5.5 Conclusions

RF system based on the Doppler principle for NIVSD is gaining popularity in recent years due to its applicability in day to day life. A simple and cost effective answer to meet the tradeoff between the detection sensitivity and the noise content of the base-band signal is provided herein for detection of signals due to heartbeat and respiration in a living human being. Concurrent dualband systems lead to a very compact design with low power consumption. Such system may be very useful in post disaster rescue

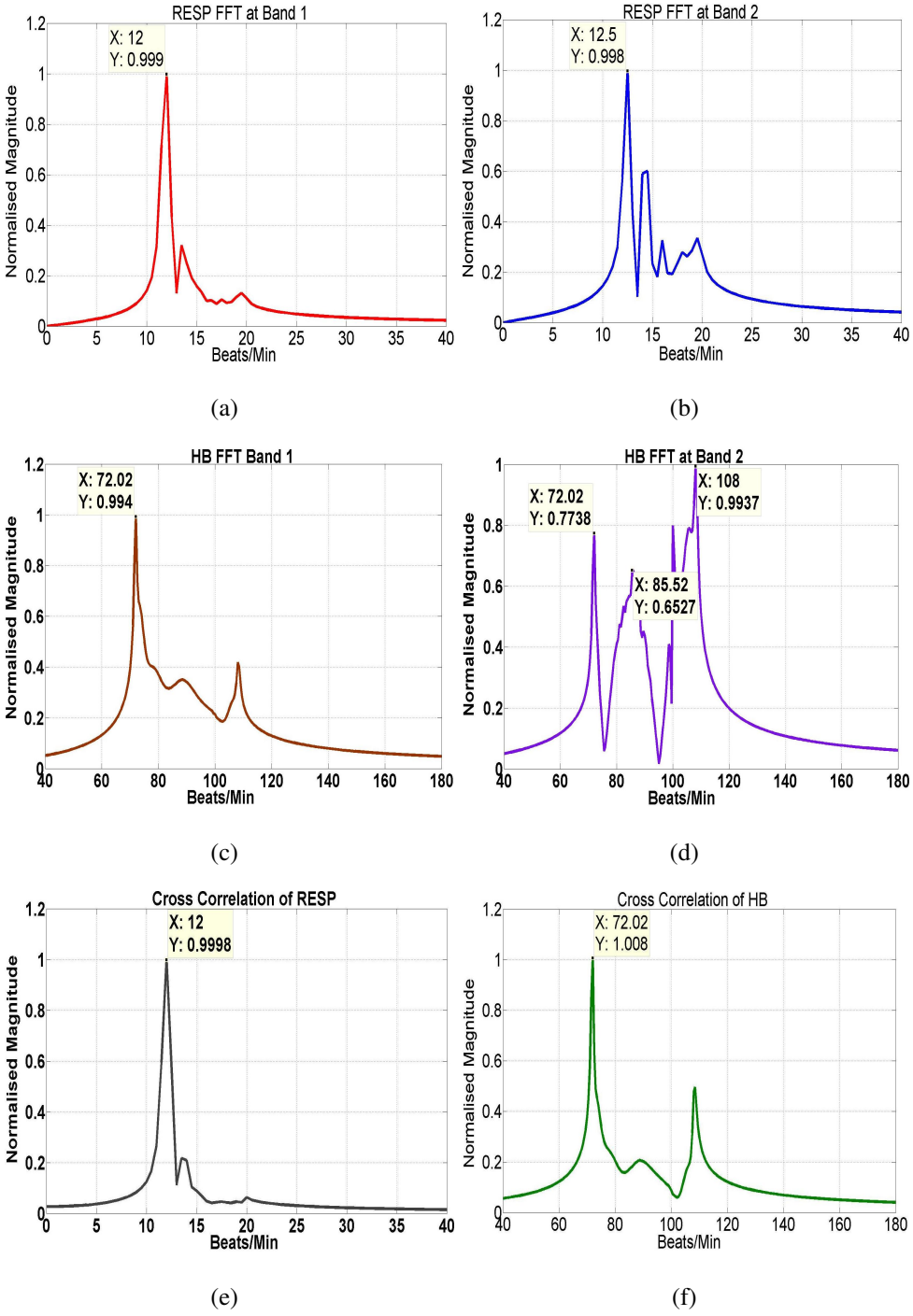

Figure 5.15: FFT analysis of the detected signal at desired band of operation.

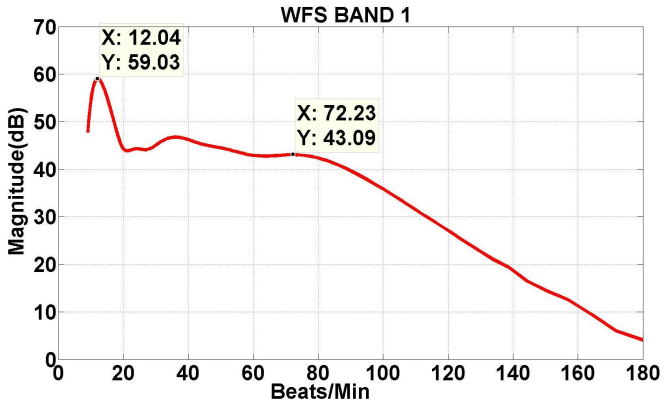

(a)

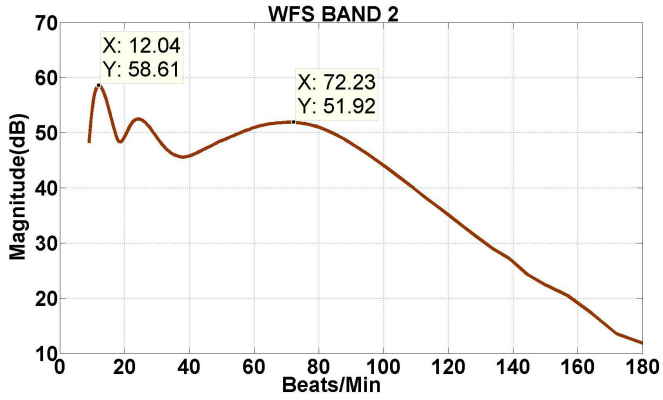

(b)

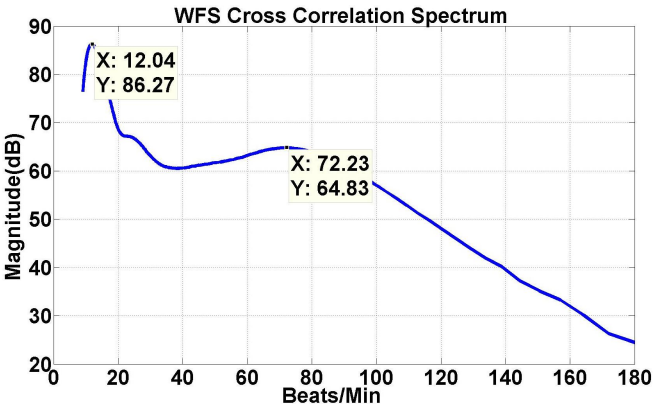

(c)

Figure 5.16: WT analysis of the detected signal at desired band of operation.

operations, battlefields, and health care applications. Due to the non-invasive nature with minimal hardware requirement, a concurrent multiband NIVSD is expected to rapidly acquire importance in day to day activities for many people despite their social or financial strata.

Chapter 6

The Occupancy Sensor

6.1 Introduction and Related work

Ascertaining accurate occupancy of a human being inside a room or in a closed space is vital in many day to day applications. This chapter describes the application of the proposed concurrent dualband RF sensor as an occupancy sensor. The occupancy is decided by the analysis of baseband signals at individual band and the correlation between them. The notable advantage of the proposed sensor is the reduction of false alarm due to its concurrent multiband operation.

Occupancy sensors have been used in a variety of daily life applications to manage air conditioning, home lighting, heating and determining the presence of human beings in residential or commercial avenues [130]. Initially limited only to security applications the occupancy sensors have drawn much attention of researchers and practitioners these days due to its wide range of applications in the modern era of 'smart homes and avenues' [131]. In the past decades, the ultrasonic sensors [133] and passive infrared sensors [132] were the two most commonly used devices for the occupancy sensing. However, these sensors were stuck up due to their limitations like higher false alarm rate, cost and failure in detection of the stationary subject, etc.

Respiration and heartbeat are the two predominant characteristics by virtue of which

the existence of human being can be ascertained. With the help of a Doppler based RF sensor, these vital signs can easily be detected and analyzed non-invasively and continuously over a distance. Hence, this methodology acquired a hot-spot in the research arena as compared to its counterparts. With these characteristics, the Doppler radar based RF sensors had emerged as a promising alternative to the existing sensors to minimize the false alarm.

Many efforts were initiated towards the development of a low-cost RF occupancy sensor. A 5.8 GHz radar was reported and used as an occupancy sensor. However, the method did not consider the heartbeats and respiration rate to confirm the factual presence of human beings. The effort in [135] had been limited only to the detection of heartbeat signal and never considered the respiration signal for the analysis. The approach in [136,137] employed a single band RF to detect the presence of the human beings. In [137], authors considered the heartbeat as well as the respiration rate for the confirmation of occupancy of a human being. All the reported methodologies had a limitation of either using either Thus, the existing RF based occupancy sensors can be characterized based on a single operational band and / or a specific vital sign detection for deciding the occupancy.

The basic purpose of an occupancy sensor is to confirm the true presence discerning non human periodic motion, which may result into a false alarm. The confirmation of the occupancy will be more accurate if it has been ascertained by the detection of respiration rate and heartbeat rather than a single vital sign. This will help out to reduce the false alarm and dead zones in the sensing operation. As the nature of these human vital signs are very weak in nature, the detection must be robust to noise with high sensitivity. Change in the rate of vital signs over the period due to irregular body movement and anxiety is the basic tendency of the human beings. Due to this feature, with a single band RF sensor, there is an enormous possibility that the sensor may generate a false alarm treating it as a human periodic motion. This is the prime disadvantage of the existing single band RF sensors. This drawback may be overcome

by using a multiband operation.

With our proposed concurrent multiband operation, the individual band detection may be carried out simultaneously. Such operation does not suffer from variable measuring conditions. Furthermore, the overall size of the circuit is very compact as a single circuit caters the need of multiband operation. Additionally, it provides a low-cost and less power hungry option for the occupancy sensing operation [123–125]. Hence, a concurrent multiband RF occupancy sensor is the best alternative to the existing ones. Table 6.1 briefly summarizes the state-of-the-art of occupancy sensor.

6.2 The Characterization of the Occupancy Sensor

The working principle of the occupancy sensor is similar to the proposed sensor as described in *Section 1.2.1.* Fig. 6.1 depicts the basic working principle of the proposed concurrent multiband RF occupancy sensor.

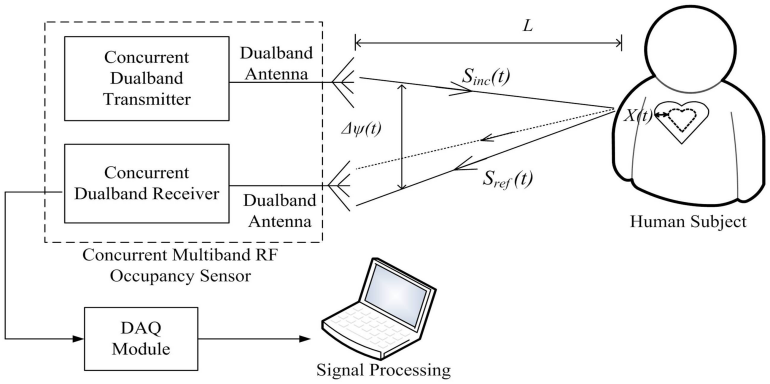

Figure 6.1: Working principle of the proposed sensor.

Fig. 6.2 shows Setup used in the characterization and performance evaluation of the proposed occupancy sensor. Human subject may breathe at a constant rate. However, heart rate variability will reveal the truth about one's existence as it cannot be periodic. Owing to this fact, in the present work, heartbeat along with respiration rate is selected to decide the occupancy.

Table 6.1: The State-of-the-art occupancy sensor

Contribution	**Methodology Operation**	**No. of Operational Band**	**Concurrent Operation**	**Subsystem Design**	**Baseband Signal Processing**
Zappi et al. [132]	Infrared	—	NO	Commercial ICs were used	—
Caicedo et.al. [133]	Ultrasonic	—	NO	Custom ICs and were used	—
Reyes et al. [134]	RF based	Single band at $5.8\ GHz$	NO	Customised circuit & were used	—
Song et al. [136]	RF based	Single band at $2.4\ GHz$	NO	Commercial ICs were used	FFT
Yavari et al. [137]	RF based	Single band at $2.405\ GHz$	NO	Commercial ICs were used	FFT
Proposed System	RF based	Concurrent operation at $2.44\ GHz$ and $5.25\ GHz$ band	YES	Indigenously designed concurrent dualband subsystem	FFT / WT

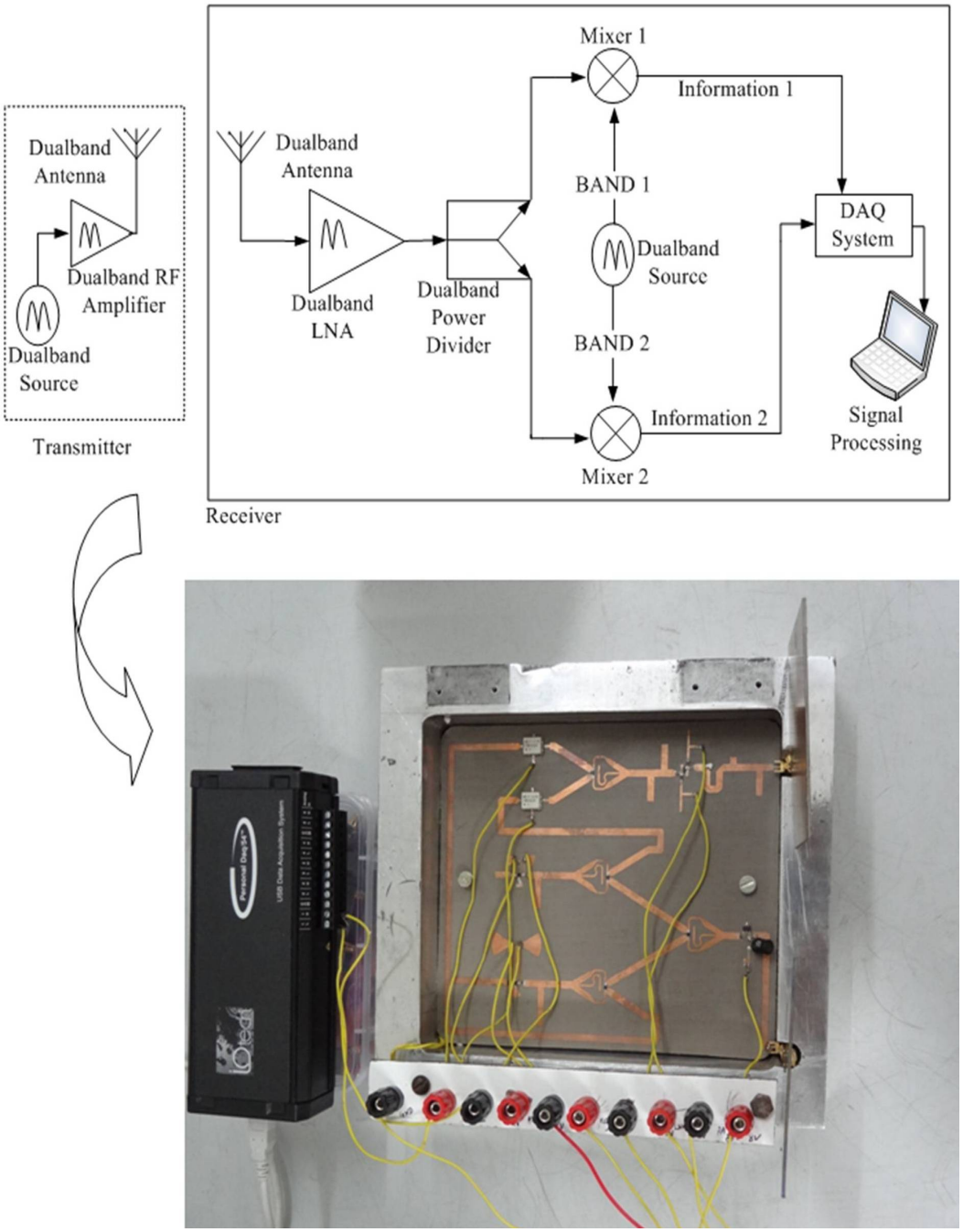

Figure 6.2: Setup used in characterization and performance evaluation of the proposed occupancy sensor.

For experimentation purpose, a 33 year male subject was stationed in an indoor environment. The baseband signals were fed to the DAQ module operating at a sampling rate of 37 Hz. The samples were taken for a 10 minute duration. In this analysis, the respiration rate and heartbeat were considered for the confirmation of the occupancy in a particular premise. The occupancy is confirmed only after exact detection of heartbeat and respiration rate. This approach reduces the false alarm rate as with the conventional sensors or the single band RF sensors.
Initially, the sensor was operated for a duration of 5 minutes without any human subject in the vicinity of the sensor. At the end of the fifth minute, a human subject was made to sit in front of the sensor. The data was recorded continuously for the next five minutes.

6.2.1 Baseband Signal Processing

Instead of infrared or ultrasonic signals, the operation of the proposed sensor is based on the detection and measurement of the back scattered EM signals from the human subject. Hence, the usual limitations associated with the conventional sensors are eradicated to confirm the true presence of the human subject. For the first initial 5 minutes, the room was kept empty and the signals were captured. At the end of the fifth minute, the human subject is made to enter the room and placed at a distance of 2 m distance from the transceiver antenna. Fig. 6.3(a) and Fig. 6.3(b) depicts received signal at individual band of operation. The required bandpass filter(BPF) is employed using MatLab. This approach helped to overcome the additional hardware and the insertion loss therein. The human respiration rate is generally in the range of $10 - 22$ (0.16 Hz to 0.36 Hz) beats per minutes with the corresponding heartbeat of $60 - 90$ (1 Hz-1.5 Hz) beats per minute in normal conditions [30]. The pass band of the BPF is set accordingly. As it is seen from the received signal at both bands for the first 5 minutes, there is no evidence of human vital signs since the room is empty. It indicates that the sensor did not capture any non human motion during the measurements.

At the end of the fifth minute, a human being was made to enter into the room. The output spectrum clearly shows the ripples around the fifth minute for about 30 seconds till the human being settles down in front of the measurement setup. Signal spectrum obtained in the following time duration shows the human vital sign.

This signal has been further frequency transferred using FFT to retrieve the human vital sign signals. Fig.6.3(c) and Fig. 6.3(d) shows the FFT spectrum of the detected signal.FFT spectrum of signals received with 2.44 GHz band does not reveal the clear understanding of the human vital sign. This kind of response may lead to generate the false alarm. However, distinct human vital signs are achieved from the signals received at 5.25 GHz. The correlation between the individual band signals[Fig.6.3(e)] eliminates the ambiguity and provides distinct signals of human respiration and heartbeat signal. As a result, a more accurate alarm regarding the existence of human being may be expected. This is the notable advantage of the concurrent multiband RF operation.

Further, the capacity of the proposed sensor has been verified by applying WT over the detected Signal. A similar response, as that with FFT method, has been achieved with the use of WT [Fig.6.4].

Table 6.2 sumarises the detection rate of human vital sign using FFT and WT methods. It is found that a fair agreement in detection of human vital sign is observed by these two methods. The detected signals are further utilised for angle of arrival estimation.

Table 6.2: Summary of VSD detection rate of the proposed sensor

Methodology	Respiration Rate (BPM)	Heartbeat) (BPM)
FFT	17.8	73.7
WT	17.17	73.71

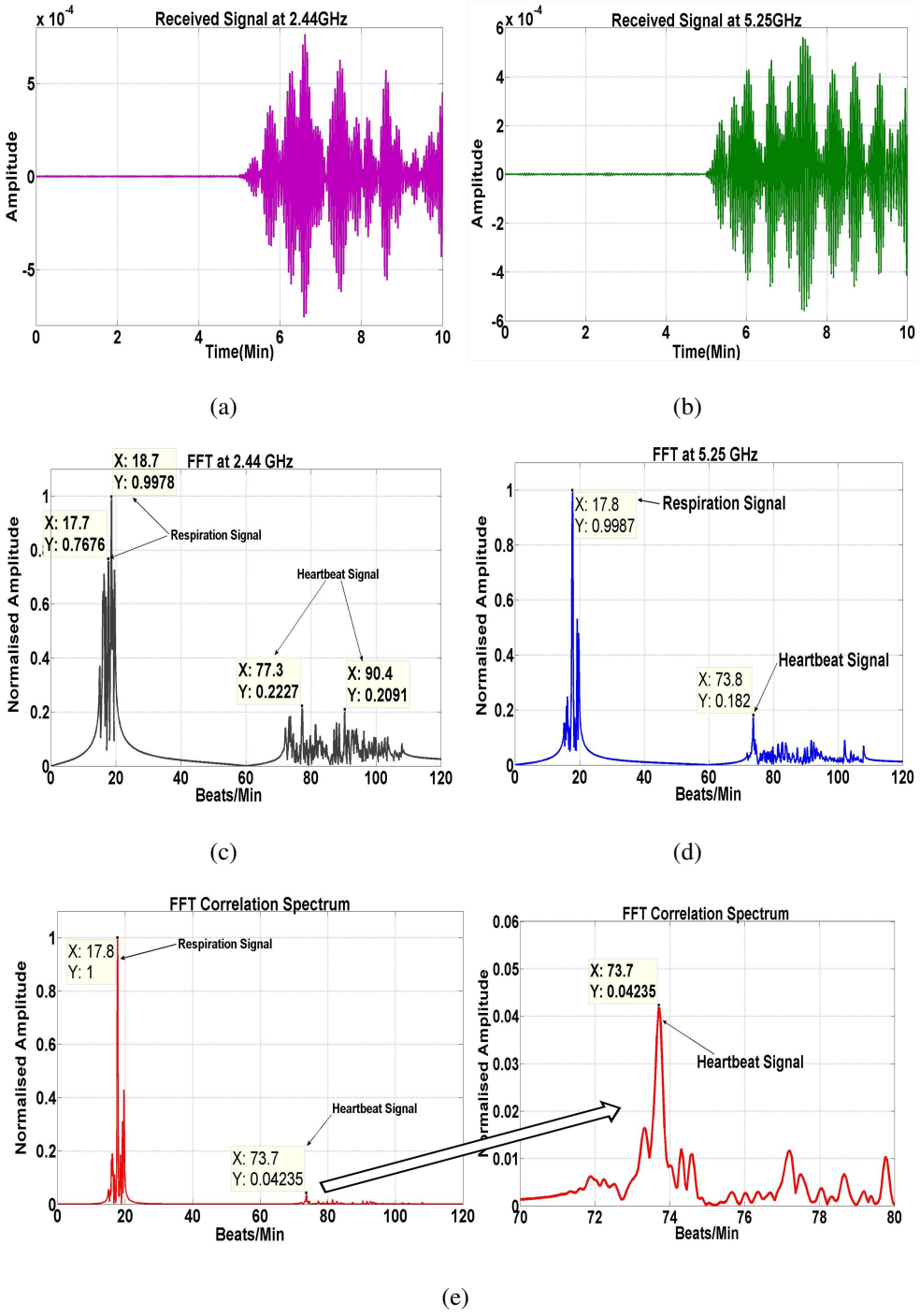

Figure 6.3: Received signal at: (a) 2.44 GHz band and (b) 5.25 GHz band, FFT spectrum of the Received signal at: (c) 2.44 GHz band and (d) 5.25 GHz band and (e) Correlation of FFT spectrum.

(a)

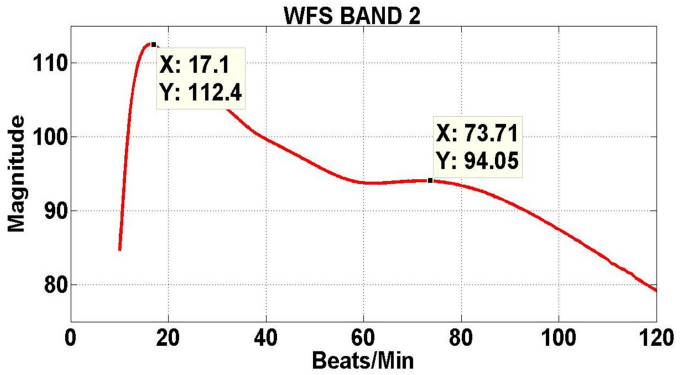

(b)

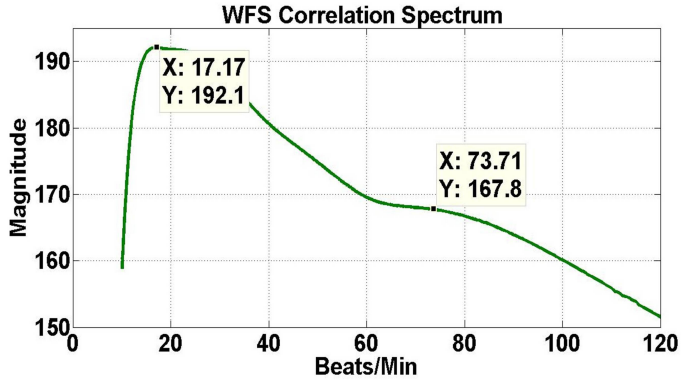

(c)

Figure 6.4: WT spectrum of the Received signal at: (a) 2.44 GHz band and (b) 5.25 GHz band (c) Correlation Spectrum of both band.

6.2.2 The Performance Analysis

The link budget, sensitivity and safety analysis and the detection range of the occupancy sensor are same as that given *Chapter 5*. Additionally the link budget and sensitivity analysis has been carried out, herein, by placing an wooden board of 30 mm thickness between the sensor and the human subject. Table 6.3 provides the details of link budget and sensitivity analysis for the proposed sensor.

Table 6.3: Link margin performance of the proposed occupancy sensor

Parameter	Single patch	Antenna array (Omni-directive)	Antenna array (Directive)
Thermal Noise	$-174\ dBm/Hz$		
SNR	$20\ dB$		
Sensitivity	$-138.62\ dBm$		
Received Power(Without Obstacle)*	-64.62	-57.32	-53.92
Received Power(With Obstacle)*	-81.73	-73.83	-70.23
Link Margin(Without Obstacle)*	74	80.7	84.7
Link Margin(With Obstacle)*	56.89	64.79	68.39

$\star$: Measured in dBm.

As the application is for indoor occupancy detection, it is must that the number of sensors required for a specific room be estimated. The maximum operational distance and the required number of sensors is estimated using Eq. 6.1 as follows

$$S_N = \frac{RA}{EA} units \tag{6.1}$$

where S_N = No. of sensor units, RA = room area in m^2, EA = exposure area of each sensor (πR_{max}^2). The experiment is initiated in a room of 25 m^2. Table 6.4 summarizes the sensor requirements in connection with maximum range and transmitted power.

Table 6.4: Output power and sensor unit requirement

Output Power (dBm)	Maximum range ($meters$)	No. of Sensor Units Requirement
-10	1.3	5
0	2.2	5
5	3	1
10	4	1
20	7.5	1

6.2.3 Indoor Location Estimation of Human Subject

The location or position of the human subject inside a room can be ascertained by calculating the angle of arrival. Many efforts were reported in the literature to estimate the angle of arrival. However, only few have concentrated on the human VSD centric approach while estimating the DOA. Table 6.5 provides the state-of-the-art of human VSD centric angle of arrival (direction of arrival-DOA) detection. The DOA is estimated by using multiple signal classification (MUSIC) algorithm [138]. Tt is quite possible that in practical situations such as in hospitals or the human victims buried under debris/rubble might not exactly face up to the sensor antenna. Measurement and estimation of the heartbeat and respiration rate using a Doppler based RF sensor is possible, even if the human chest is not pointed directly towards sensor [75]. In comparison to a single band sensor used in [75], we have employed a concurrent dualband sensor for detection purpose. Due to the advantages of concurrent multiband operation, the possibility of false signal generation has been mitigated in present approach. The human being may be in any orientation as shown in Fig. 6.5. For the present analysis, the human subject under test was distanced 2 m and positioned at different angles away from the transceiver. The sampling rate and the sampling inter-

Table 6.5: DoA system comparison

Parameter	**Isar et.al [139]**	**Yong et.al. [140]**	Proposed Sensor
Operational Band	2.4 GHz	2.45 GHz	Concurrent at 2.44 GHz and 5.25 GHz
Switching Mechanism	RF switch based operation	PLL based switch operation	Not Required
No. of System employed	One-A separate transmitter and receiver	One-A separate transmitter and receiver	One-Concurrent dualband transceiver
MIMO Operation Support	No	Yes	Yes
Subsystems Used	Commercial Subsystems	Commercial Subsystems	Indigenously customised concurrent dualband subsystems

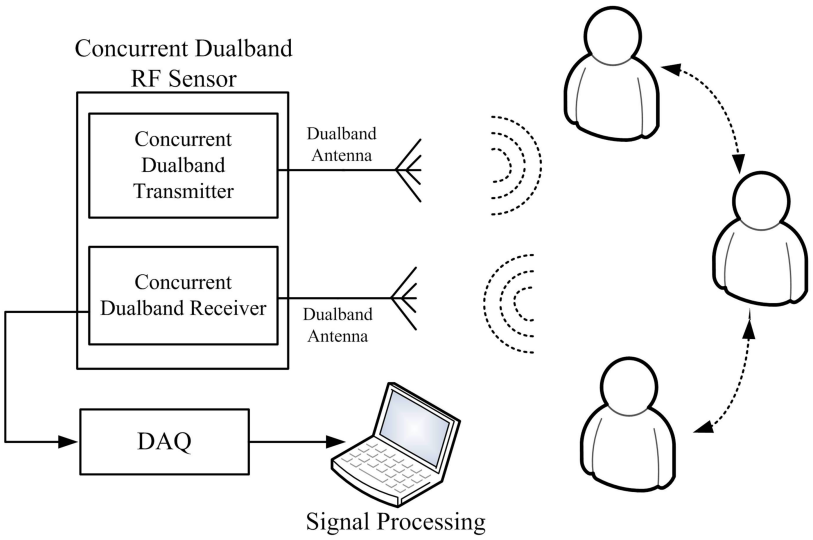

Figure 6.5: Conceptual diagram of measurement environment for DoA estimation.

val are kept same as that of occupancy measurement. The received data will be in the form of

$$y[n] = [y_1.....y_k] \tag{6.2}$$

Here, y_k is the baseband signal recorded at *Band 1* and *Band 2* and n is the total number of samples acquired. With the acquired multiband data, a DoA spectrum is calculated. The peaks in the pseudo spectrum are the DoA (angle of arrival-AoA) for the human subject under test. For the present analysis, the human subject under test was distanced 2 m and positioned manually at 30^o, 90^o, 130^o and 160^o away from the transmitting antenna such that human chest is not directly pointed towards the transmitting antenna. The placement of the human subject at these angles was done manually and this method had its own limitations. Fig.6.6 shows the estimated DoA at different angles with the proposed sensor. It shows that the human subject is positioned at an angle of 31.5^o, 91^o, 127^o and 166^o from the sensor. The difference in the actual and measured angles may be attributed to the manual measurement of angles for the placement of the human subject. Here, only one peak has been observed since only a single receiver antenna was employed. The catch line advantage of the

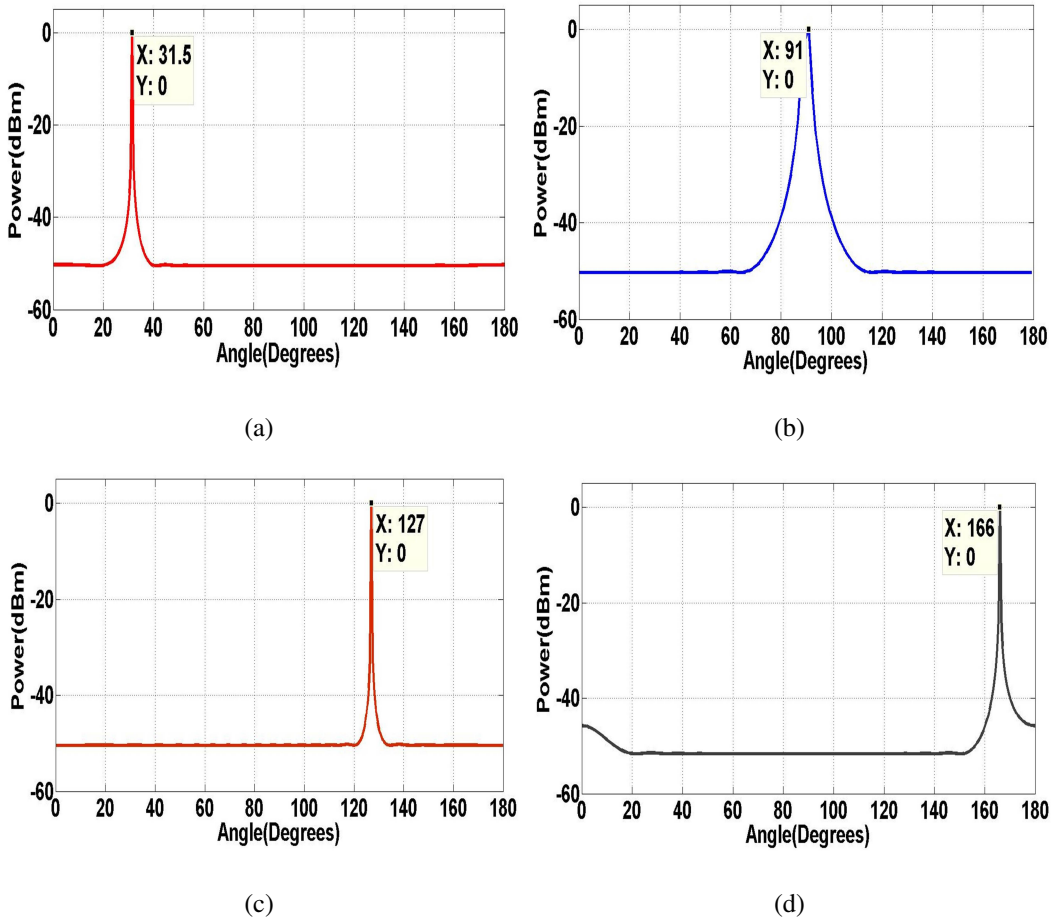

Figure 6.6: DOA estimation at:(a) 30^o (b) 90^o (c) 130^o (d) 160^o.

present detection work lies in the multiband operation of the sensor system. Data in the individual frequency band was assumed to be received from individual antennae, which are correlated to arrive at a final conclusion. This approach is found very useful in the tracking of multiple objects or continuously moving objects. Thus, the correlation of the multiband data not only provides the correct estimation of DoA, but it also reduces the motion artifacts, clutters and allied noise. In [140], MIMO operation was achieved by two different systems, while in our proposed approach, MIMO operation was achieved in a single sensor unit simultaneously operating in multiple frequency bands. The DoA estimation is very useful for law enforcement agencies to identify

the number of persons in a closed space or for through wall detection.

6.3 Conclusions

A dual input and dual output concurrent dualband RF sensor has been used to sense the presence of a human being inside a room. The inability of the existing occupancy sensors to detect stationary subject is alleviated in this RF sensor. The false alarms and the dead spots in the sensing operation is effectively reduced by using both heartbeat and respiration rate signals to sense the human presence. Due to concurrent dualband operation, the proposed sensor has a very compact size and low power consumption. This sensor will be very useful in elderly people home care and for law enforcement agencies to decide the human occupancy in a room.

Chapter 7

Conclusions and Future Scope

7.1 Conclusions

In this thesis, a concurrent dualband non-invasive vital-sign monitoring sensor system is proposed and demonstrated. The proposed system is devised on the popular Doppler shift theory and simultaneous operation over two frequency bands, namely 2.44 GHz and 5.25 GHz band.

Here, the baseband signal after the mixer stage is generally proportional to chest disarticulation and thus contains the information about the movement due to heartbeat and respiration. Using this information, the existence of a human life can be ascertained. Based on this notion, a non-invasive heart and respiration monitor is developed.

There are various technical obstructions in designing an NIVSD system such as the influence of clutter noise and phase noise, the harmonics, DC offset and null point problem. Various academicians and researchers had suggested many techniques to overcome these challenges whereby a stable and reliable detection has been achieved. For people having a large chest wall movement due to breathing, lower frequency system is better. For increased detection sensitivity, higher band systems are preferred. However, the existing single band systems can not provide these to attributes, in vital sign detection, simultaneously. The challenge to bridge the trade off between lower

noise content and higher detection accuracy was unattended before the initiation of this research work. This challenge had motivated the present thesis work.

The entire work is divided into four parts. In the first part of the system design and development, a concurrent dualband antenna, both omni-directional and directional type, to operate simultaneously at the designated bands was designed. Apart from this, a concurrent dualband LNA and a WPD was also designed as the subsystems for the proposed system.

In the second stage, simulation verification of the proposed system with ADS platform was carried out. Here measured *'S2P'* files of the subsystems were used for simulation. Then a measurement prototype was established with the VNA and two concurrent dualband patch antennae. The set up had shown accurate detection upto a distance of 1 m. With this experience, a measurement setup was developed with the help of our own customized concurrent dualband subsystems and off-the-shelf laboratory equipments. The individual subsystems were connected together via cables and connectors. The set up showed an accuracy of detection upto 2 m. But it had suffered from a lot of noise in the received data.

Based on the experience of the previous two stages, the problem of noise content is overcame by fabricating the entire circuitry on a single substrate. This approach minimised the noise in comparison to the previous versions as the need of cables and connectors are eliminated. Further, a novel method to process the noisy baseband signal is developed. With the help of the fabricated system and signal processing, it is observed that the noise content is significantly reduced and distinct peaks of respiration and heartbeat were observed at both the designated bands as well as after correlation of the individual band data.

Efforts are being initiated towards the design and development of a portable, handheld complete sensor system. Such systems can be very useful in post disaster rescue operations, battlefields, and in health care applications. Due to the non-invasive nature with minimal hardware requirement, a concurrent multiband NIVSD is expected

to rapidly acquire importance in day to day activities for many people despite their social or financial strata.

7.2 Future Scope

7.2.1 A Reconfigurable / Tunable Concurrent Dualband NIVSD

A reconfigurable / tunable NIVSD is to be designed to operate between the entire individual WLAN bands (i.e. 2.14 GHz to 2.45 GHz and 5.15 GHz to 5.35 GHz). This will help the user to choose an optimal frequency ratio for a particular operation. Fig. 7.1 shows the conceptual diagram and measurement prototype for the reconfigurable concurrent dualband RF system for non-invasive human vital sign detection.

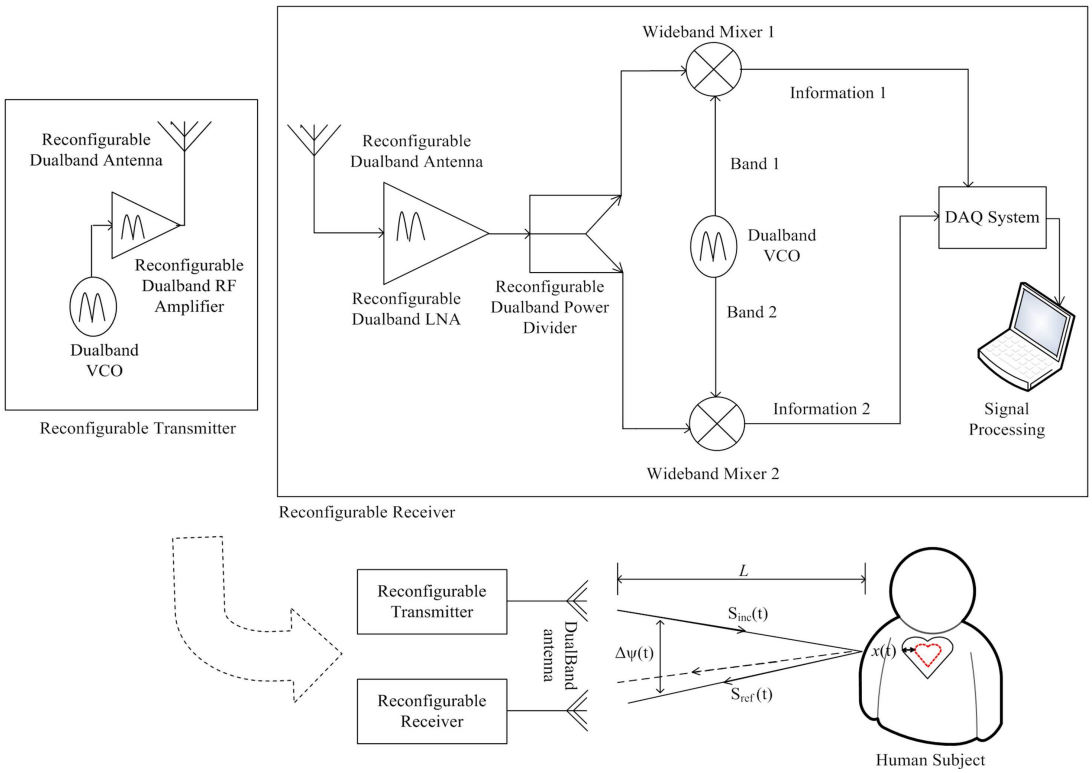

Figure 7.1: Conceptual block diagram of a reconfigurable multiband RF system for human VSD.

The selection of proper frequency ratio plays a key role for the accuracy and sensitivity of a concurrent multiband RF system employed for NIVSD application. The performance of such concurrent multiband RF system can be further improved by incorporation of the concept of reconfigurability. It provides the flexibility to select the individual operational bands depending on the need of the application(s). This novelty may be achieved by designing the individual reconfigurable subsystems.The additional feature of reconfigurability provides the benefit of selecting the best frequency ratio for a particular operation by tuning the frequency of operation at both bands concurrently.

The proper selection of frequency ratio provides twofold advantage over the static multiband RF radios. Firstly, the noise performance and sensitivity can be improved and secondly the improved accuracy can be obtained in the detection of weak human vital sign signals. All these features can be obtained via multiband RF systems with the incorporation of a varactor diode as a tuning element. By controlling the bias voltage of the varactor diode desired tuning can be achieved.

7.2.2 A Hand-held Concurrent Dualband Human Life Tracking Sensor

In real time application, it is not always feasible to carry bulky tracking systems for sensing human life. Hence, there is a need to develop a portable hand-held device to sense the human vital signs. This may be possible by indigenously comprehended concurrent dualband subsystems to replace the off-the-shelf laboratory equipment. A partial effort had been initiated during this thesis work by fabricating a transceiver prototype on a single substrate. Fig.5.12 depicts the prototype of the proposed portable hand-held concurrent dualband sensor for human vital sign detection. In future, this prototype is to be converted into full functioning hand-held device for NIVSD applications.

Appendix A

ATF−36163 Data Sheet

ATF-36163
1.5 – 18 GHz Surface Mount Pseudomorphic HEMT

Data Sheet

Description

The Avago ATF-36163 is a low-noise Pseudomorphic High Electron Mobility Transistor (PHEMT), in the SOT-363 (SC-70) package. When optimally matched for minimum noise figure, it will provide a noise figure of 1 dB at 12 GHz and 0.6 dB at 4 GHz.

Additionally, the ATF-36163 has low noise-resistance, which reduces the sensitivity of noise performance to variations in input impedance match. This feature makes the design of broad band low noise amplifiers much easier. The performance of the ATF-36163 makes this device the ideal choice for use in the 2nd or 3rd stage of low noise cascades. The repeatable performance and consistency make it appropriate for use in Ku-band Direct Broadcast Satellite (DBS) TV systems, C-band TV Receive Only (TVRO) LNAs, Multichannel Multipoint Distribution Systems (MMDS), X-band Radar detector and other low noise amplifiers operating in the 1.5 –18 GHz frequency range.

This GaAs PHEMT device has a nominal 0.2 micron gate length with a total gate periphery (width) of 200 microns. Proven gold-based metallization system and nitride passivation assure rugged, reliable devices.

Surface Mount Package
SOT-363 (SC-70)

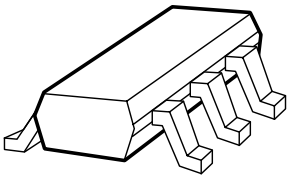

Features

- Lead-free Option Available
- Low Minimum Noise Figure:
  1 dB Typical at 12 GHz
  0.6 dB Typical at 4 GHz
- Associated Gain:
  9.4 dB Typical at 12 GHz
  15.8 dB Typical at 4 GHz
- Maximum Available Gain:
  11 dB Typical at 12 GHz
  17 dB Typical at 4 GHz
- Low Cost Surface Mount Small Plastic Package
- Tape-and-Reel Packaging Option Available

Applications

- 12 GHz DBS Downconverters
- 4 GHz TVRO Downconverters
- S or L Band Low Noise Amplifiers

Pin Connections and Package Marking

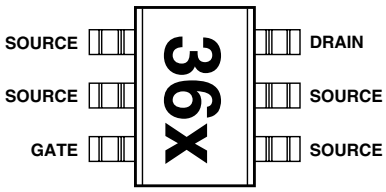

Note: Top View. Package marking provides orientation and identification.

" 36 " = Device code
" x " = Data code character

Attention: Observe precautions for handling electrostatic sensitive devices.
ESD Machine Model (Class A)
Refer to Avago Application Note A004R: Electrostatic Discharge Damage and Control.

ATF-36163 Absolute Maximum Ratings[1]

Symbol	Parameter	Units	Absolute Maximum
V_{DS}	Drain - Source Voltage	V	+3
V_{GS}	Gate - Source Voltage	V	-3
V_{GD}	Gate Drain Voltage	V	-3.5
I_D	Drain Current	mA	I_{dss}
P_T	Total Power Dissipation	mW	180
$P_{in\ max}$	RF Input Power	dBm	+10
T_{CH}	Channel Temperature	°C	150
T_{STG}	Storage Temperature	°C	-65 to 150

Thermal Resistance:
$\theta_{ch\text{-}c} = 160°C/W$

Note:
1. Operation of this device above any one of these parameters may cause permanent damage.

ATF-36163 Electrical Specifications $T_C = 25°C$, $Z_O = 50\ \Omega$, $V_{ds} = 1.5$ V, $I_{ds} = 10$ mA, (unless otherwise noted).

Symbol	Parameters and Test Conditions		Units	Min.	Typ.	Max.
NF	Noise Figure[1]	f =12.0 GHz	dB		1.2	1.4[1]
G	Gain at NF[1]	f = 12.0 GHz	dB	9	10	
g_m	Transconductance	V_{DS} = 1.5 V, V_{GS} = 0 V	mS	50	60	
I_{dss}	Saturated Drain Current	V_{DS} = 1.5 V, V_{GS} = 0 V	mA	15	25	40
$V_{p\ 10\%}$	Pinchoff Voltage	V_{DS} = 1.5 V, I_{DS} = 10% of I_{dss}	V	-1.0	-0.35	-0.15
BV_{GDO}	Gate Drain Breakdown Voltage	I_G = 30 µA	V			-3.5

Note:
1. Measured in a test circuit tuned for a typical device.

ATF-36163 Typical Parameters $T_C = 25°C$, $Z_O = 50\ \Omega$, $V_{ds} = 2$ V, $I_{ds} = 15$ mA, (unless otherwise noted).

Symbol	Parameters and Test Conditions		Units	Typ.
F_{min}	Minimum Noise Figure ($\Gamma_{source} = \Gamma_{opt}$)	f = 4 GHz	dB	0.6
		f = 12 GHz	dB	1.0
G_a	Associated Gain	f = 4 GHz	dB	15.8
		f = 12 GHz	dB	9.4
G_{max}	Maximum Available Gain[1]	f = 4 GHz	dB	17.2
		f = 12 GHz	dB	10.9
P_{1dB}	Output Power at 1 dB Gain Compression	f = 4 GHz	dBm	5
	under the power matched condition	f = 12 GHz	dBm	5
V_{GS}	Gate to Source Voltage for I_{DS} = 15 mA	V_{DS} = 2.0 V	V	-0.2

Note:
1. Gmax = MAG for K > 1 and Gmax = MSG for K ≤ 1, which is shown on the S-parameters tables.

Appendix B

MATLAB Code for Concurrent Dualband Matching Network

```
clc
clear all
close all
%
disp('============================================================
================')
disp('                          Dual-Stub  Dual-Frequency  Matching
Network')
disp('============================================================
================')
disp(' ')

disp(' ---------------/-----------/---------|')
disp(' main line Z0  /           /          ZL''')
disp(' -------------/---/---d---/---/---l---|')
disp('             /  ls1      /  ls2')
disp('            /___/       /___/')
disp(' ')

sln = [];% Solution Matrix

% Parameters
Z0_ohm = 50;     % characteristic impedance of each transmission
line (TL)
len_incr = 0.01; % increment in length (mm) at each iteration
diff_lmt = 0.01; % limit on difference in physical lengths (mm),
at two freqs.

% Data
fr_ghz = [2.44 5.25]; % dual frequencies in GHz

% Required Source Impedances for LNA Design
%zs = [(First Impedance) (Second impedance)];
%zout = (1/50)* [(First Impedance) (Second impedance)];]; zl =
conj(zout);
zl   =   (1/50)*[   First   Impedance      Second   impedance];
%DBOSC_S_PARA_DB_BIASNW_WITHPAD(matching)
% Required Source and Load Reflection Co-efficients for Maximum
Gain of Amplifier

%Gs    =    [(1/1.178)*exp(j*pi*-2.154/180)    (1/1.66)*exp(j*pi*-
60.037/180)];
%Gs = (zs-1)./(zs+1);
%Gl          =          [-0.3212*exp(j*pi*-0.7477/180)          -
0.1078*exp(j*pi*0.7191/180)];
Gl = (zl-1)./(zl+1);
```

```
Er = 3.2;       % substrate dielectric constant
H_mm = 1.524;   % substrate height in mm
W_mm = 3.64;  % width of each TL section with 50 Ohms
characteristic impedance
% effective dielectric constant for W/h > 1
er_eff = (Er+1)/2 + (Er-1)/(2*sqrt(1+12*H_mm/W_mm));
rf = fr_ghz(2)/fr_ghz(1); % frequency ratio
lmda_eff_mm    =    300./(fr_ghz*sqrt(er_eff));    %    effective
wavelengths at two freqs
beta_eff_mmi = 2*pi./lmda_eff_mm; % propagation constant in mm^-
1

ch = input('Press 0 for Source Matching OR 1 for Load Matching:
');
% Normalized impedances at dual freqs.
if (ch)
    zl = (1+Gl)./(1-Gl);
    Gm = Gl;
    disp('Load Matching')
else
    zl = (1+Gs)./(1-Gs);
    Gm = Gs;
    disp('Source Matching')
end
fprintf('\n Selected Dual Frequencies: f1 = %.4f-GHz; f2 = %.4f-
GHz', fr_ghz(1), fr_ghz(2))
disp(' ')
disp(['Selected Reflection Co-efficients: ' num2str(Gm)])
fprintf('\n Corresponding Impedances (Ohms):')
disp(zl)
disp('-------------------------------------------------------
-----------------')
disp(' Iterations Start')
disp('-------------------------------------------------------
-----------------')
l_mm =3; % length (mm) of I series TL section, to be varied in
loop 1
while(l_mm < 60) % start loop 1
    thl_rad = beta_eff_mmi*l_mm; % electrical length (degrees)
of I series TL
    tl = tan(thl_rad);

    yL = (1+j*zl.*tl)./(zl+j*tl); % admittance at the input of I
series TL
    gL = real(yL);
    bL = imag(yL);
    zL = 1./yL;
```

```
    d_mm =3; % length (mm) of II series TL section, to be varied
in loop 2
    while(d_mm < 60) % start loop 2
        thd_rad   =   beta_eff_mmi*d_mm;   %   electrical   length
(degrees) of II TL

        gmax   =   1./(sin(thd_rad).^2);   %   maximum   allowed
conductance for given d
        if((gL(1) > gmax(1)) | (gL(2) > gmax(2)))
            d_mm = d_mm + len_incr;
            continue;
        end

        d_lmda = d_mm./lmda_eff_mm;

        % calculation of lengths of the two shunt stubs
        ls12_lmda1 = stub2(zL(1),d_lmda(1),'oo'); % solution at
first freq
        ls12_f1_mm = ls12_lmda1*lmda_eff_mm(1);
        ls12_lmda2 = stub2(zL(2),d_lmda(2),'oo'); % solution at
second freq
        ls12_f2_mm = ls12_lmda2*lmda_eff_mm(2);

        % ths12_f1_deg = ls12_lmda1*180;
        % ths12_f2_deg = ls12_lmda2*180;

        % Checking if the physical lengths of the two shunt
stubs are equal
        % at the two desired frequencies
        diff    =    abs(vertcat(ls12_f1_mm-ls12_f2_mm,ls12_f1_mm-
[ls12_f2_mm(2,:); ls12_f2_mm(1,:)]));
        difs = sortrows(diff);
        if(nnz(difs(1,:) < diff_lmt)==2)
            % Series TL lengths are displayed if the target is
achieved
            fprintf(' Series TL physical lengths: l = %d-mm  d =
%d-mm', l_mm, d_mm)
            fprintf('\n Corresponding electrical lengths (deg)
at  f1:  thl  =  %.4f    thd  =  %.4f\n\n',  thl_rad(1)*180/pi,
thd_rad(1)*180/pi)
            %  Shunt  stub  lengths  displayed  for  the  achieved
target
            ps = find(diff(:,1) < diff_lmt);
            if(ps > 2) % Positions of lengths with differences
within limits
                ps1 = ps - 2; ps2 = 5 - ps;
```

```
            else
                ps1 = ps; ps2 = ps;
            end
            disp(' Shunt stub physical lengths (mm) at')
            disp([' f1: ' num2str(ls12_f1_mm(ps1,:))])
            disp([' f2: ' num2str(ls12_f2_mm(ps2,:))])
            disp(['err: ' num2str(difs(1,:))])
            disp('  Corresponding  electrical  lengths  (deg)  at
f1')
            disp(['Case1:                                          '
num2str(180*beta_eff_mmi(1)*ls12_f1_mm(ps1,:)/pi)])
            disp(['Case2:                                          '
num2str(180*beta_eff_mmi(1)*ls12_f2_mm(ps2,:)/pi)])
            disp(['Averg:                                          '
num2str(180*beta_eff_mmi(1)*(ls12_f1_mm(ps1,:)+ls12_f2_mm(ps2,:)
)/(2*pi))])

            % Solution Matrix
            sln    =    [sln;    l_mm    d_mm    ls12_f1_mm(ps1,:)
ls12_f2_mm(ps2,:) difs(1,:)];

            % stub_eleclen_f1_deg = ths12_f1_deg
            % stub_eleclen_f2_deg = ths12_f2_deg
            disp('-----------------------------------------------
------------')
        end
        d_mm = d_mm + len_incr;
    end % end of loop 2
    l_mm = l_mm + len_incr;
end % end of loop 1
fprintf(' Iterations End \n')
ch = input('PRESS any key to continue: ');

clc
disp('=========================================================
============')
disp('                          Dual-Stub  Dual-Frequency  Matching
Network')
disp('=========================================================
============')
disp(' ')
disp(' ---------------/-----------/---------|')
disp(' main line Z0  /           /          ZL''')
disp(' -------------/---/---d---/---/---l---|')
disp('             /  ls1      /  ls2')
disp('            /___/       /___/')
disp(' ')
```

```
disp('-------------------------------------------------------------
------------')
disp('                            VARIOUS DIMENSION SOLUTIONS')
disp('-------------------------------------------------------------
------------')
disp(['                                at ' num2str(fr_ghz(1)) 'GHz
at' num2str(fr_ghz(2)) 'GHz          Errors'])
disp('    l(mm)        d(mm)        ls1(mm)    ls2(mm)    ls1(mm)
ls2(mm)ls1(mm)   ls2(mm)')
disp('-------------------------------------------------------------
------------')
disp(sln)
disp('-------------------------------------------------------------
------------')
```

Appendix C

NE−4210S01 Data Sheet

PRELIMINARY DATA SHEET

NEC

HETERO JUNCTION FIELD EFFECT TRANSISTOR

NE4210M01

C to Ku BAND SUPER LOW NOISE AMPLIFIER
N-CHANNEL HJ-FET

DESCRIPTION

The NE4210M01 is a Hetero Junction FET that utilizes the hetero junction to create high mobility electrons. Its excellent low noise and high associated gain make it suitable for DBS, TVRO and another commercial systems.

FEATURES

- Super Low Noise Figure & High Associated Gain
  NF = 0.8 dB TYP., G_a = 11 dB TYP. at f = 12 GHz
- 6pin super minimold package
- Gate Width: Wg = 200μm

ORDERING INFORMATION

Part Number	Package	Supplying Form	Marking
NE4210M01-T1	6-pin super minimold	Embossed tape 8 mm wide. 1, 2, 3 pins face to perforation side of the tape	V73

ABSOLUTE MAXIMUM RATINGS (T_A = 25 °C)

Parameter	Symbol	Ratings	Unit
Drain to Source Voltage	V_{DS}	4.0	V
Gate to Source Voltage	V_{GS}	–3.0	V
Drain Current	I_D	I_{DSS}	mA
Gate Current	I_G	100	μA
Total Power Dissipation	P_{tot}	125	mW
Channel Temperature	T_{ch}	125	°C
Storage Temperature	T_{stg}	–65 to +125	°C

The information in this document is subject to change without notice.

Document No. P13682EJ1V0DS00 (1st edition)
Date Published August 1998 N CP(K)
Printed in Japan

RECOMMENDED OPERATING CONDITION (T_A = 25 °C)

Characteristic	Symbol	MIN.	TYP.	MAX.	Unit
Drain to Source Voltage	V_{DS}		2	3	V
Drain Current	I_D		10	20	mA
Input Power	P_{in}			+5	dBm

ELECTRICAL CHARACTERISTICS (T_A = 25 °C)

Parameter	Symbol	Test Conditions		MIN.	TYP.	MAX.	Unit
Gate to Source Leak Current	I_{GSO}	V_{GS} = –3 V			0.5	10	μA
Saturated Drain Current	I_{DSS}	V_{DS} = 2 V, V_{GS} = 0 V		20	60	90	mA
Gate to Source Cutoff Voltage	$V_{GS(off)}$	V_{DS} = 2 V, I_D = 100 μA		–0.2	–0.7	–2.0	V
Transconductance	g_m	V_{DS} = 2 V, I_D = 10 mA		50	65		mS
Noise Figuer	NF	f = 12 GHz	V_{DS} = 2 V I_D = 10 mA		0.8	1.1	dB
		f = 4 GHz			0.4		
Associated Gain	G_a	f = 12 GHz		9.0	11.0		dB
		f = 4 GHz			16.0		

PACKAGE DIMENSIONS

6 pin super minimold (Unit: mm)

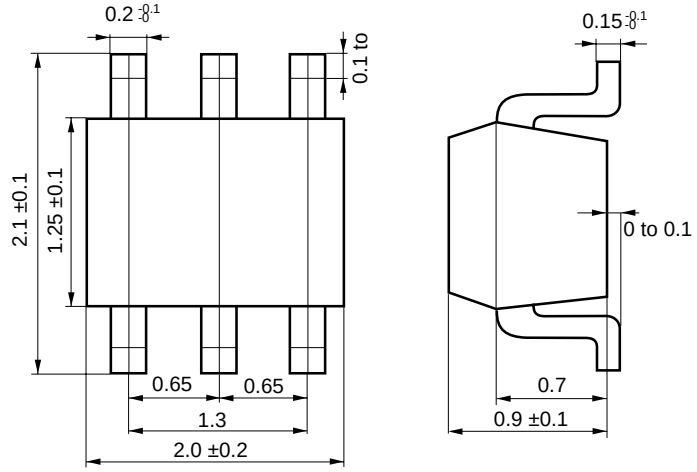

PIN CONNECTIONS

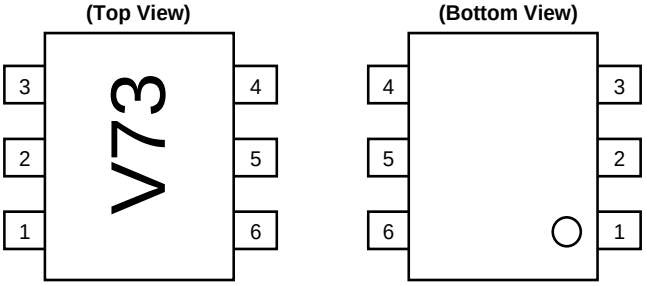

Pin No.	Pin Name
1	Gate
2	Source
3	Source
4	Drain
5	Source
6	Source

Appendix D

GALI−24+ Data Sheet

Surface Mount

Monolithic Amplifier

DC-6 GHz

Product Features

- High gain, 25 dB typ. at 100 MHz
- High IP3, 35 dBm typ.
- High Pout, P1dB 19 dBm typ.
- Internally Matched to 50 Ohms
- Transient protected
- Excellent ESD Protection
- Unconditionally stable
- Aqueous washable
- Protected by US patent 6,943,629

Gali-24+

CASE STYLE: DF782
PRICE: $1.75 ea. QTY. (20)

+RoHS Compliant
The +Suffix identifies RoHS Compliance. See our web site for RoHS Compliance methodologies and qualifications

Typical Applications

- Base station infrastructure
- Portable Wireless
- CATV & DBS
- MMDS & Wireless LAN

General Description

Gali-24+ (RoHS compliant) is a wideband amplifier offering high dynamic range. Lead finish is SnAgNi. It has repeatable performance from lot to lot and is enclosed in a SOT-89 package. It uses patented Transient Protected Darlington configuration and is fabricated using InGaP HBT technology. Expected MTBF is 3,000 years at 85°C case temperature. Gali-24+ is designed to be rugged for ESD and supply switch-on transients.

simplified schematic and pin description

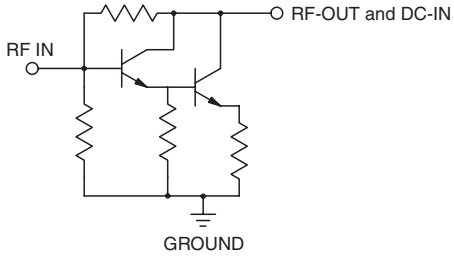

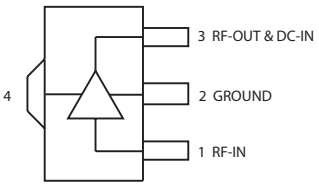

Function	Pin Number	Description
RF IN	1	RF input pin. This pin requires the use of an external DC blocking capacitor chosen for the frequency of operation.
RF-OUT and DC-IN	3	RF output and bias pin. DC voltage is present on this pin; therefore a DC blocking capacitor is necessary for proper operation. An RF choke is needed to feed DC bias without loss of RF signal due to the bias connection, as shown in "Recommended Application Circuit".
GND	2,4	Connections to ground. Use via holes as shown in "Suggested Layout for PCB Design" to reduce ground path inductance for best performance.

Electrical Specifications at 25°C and 80mA, unless noted

Parameter		Min.	Typ.	Max.	Units	Cpk
Frequency Range*		DC		6	GHz	
Gain	f=0.1 GHz	24.0	25.3	26.6	dB	≥1.5
	f=1 GHz		22.6			
	f=2 GHz	18.1	19.1	20.1		
	f=3 GHz		16.6			
	f=4 GHz	14.2	14.9	15.6		
	f=6 GHz		12.4			
Magnitude of Gain Variation versus Temperature (values are negative)	f=0.1 GHz		0.0021		dB/°C	
	f=1 GHz		0.0035			
	f=2 GHz		0.0045	0.0090		
	f=3 GHz		0.0056			
	f=4 GHz		0.0074			
	f=6 GHz		0.0154			
Input Return Loss	f=0.1 GHz		21.6		dB	
	f=1 GHz		20.4			
	f=2 GHz	14	17.5			
	f=3 GHz		15.4			
	f=4 GHz		14.9			
	f=6 GHz		19.0			
Output Return Loss	f=0.1 GHz		18.5		dB	
	f=1 GHz		11.5			
	f=2 GHz	7	9.1			
	f=3 GHz		8.8			
	f=4 GHz		8.8			
	f=6 GHz		7.2			
Reverse Isolation	f=2 GHz		26.7		dB	
Output Power @1 dB compression	f=0.1 GHz	18.3	19.3		dBm	≥1.5
	f=1 GHz	18.2	19.2			
	f=2 GHz	18.4	19.4			
	f=3 GHz		19.3			
	f=4 GHz		18.1			
	f=6 GHz		14.7			
Saturated Output Power (at 3dB compression)	f=0.1 GHz		21.1		dBm	
	f=1 GHz		20.9			
	f=2 GHz		21.0			
	f=3 GHz		20.4			
	f=4 GHz		19.1			
	f=6 GHz		16.0			
Output IP3	f=0.1 GHz	30.4	33.8		dBm	≥1.5
	f=1 GHz	31.5	35.0			
	f=2 GHz	32.7	36.3			
	f=3 GHz		35.3			
	f=4 GHz		33.1			
	f=6 GHz		30.3			
Noise Figure	f=0.1 GHz		4.2	5.2	dBm	≥1.5
	f=1 GHz		4.3			
	f=2 GHz		4.2	5.2		
	f=3 GHz		4.3			
	f=4 GHz		4.5	5.5		
	f=6 GHz		5.3			
Group Delay	f=2 GHz		97		psec	
Recommended Device Operating Current			80		mA	
Device Operating Voltage		5.4	5.8	6.2	V	≥1.5
Device Voltage Variation vs. Temperature at 80mA			-3.6		mV/°C	
Device Voltage Variation vs Current at 25°C			3.3		mV/mA	
Thermal Resistance, junction-to-case[1]			64		°C/W	

*Guaranteed specification DC-6 GHz. Low frequency cut off determined by external coupling capacitors.

Absolute Maximum Ratings

Parameter	Ratings
Operating Temperature*	-45°C to 85°C
Storage Temperature	-65°C to 150°C
Operating Current	160mA
Power Dissipation	1W
Input Power	13 dBm

Note: Permanent damage may occur if any of these limits are exceeded.
These ratings are not intended for continuous normal operation.
[1]Case is defined as ground leads.
*Based on typical case temperature rise 7°C above ambient.

Notes
A. Performance and quality attributes and conditions not expressly stated in this specification document are intended to be excluded and do not form a part of this specification document.
B. Electrical specifications and performance data contained in this specification document are based on Mini-Circuit's applicable established test performance criteria and measurement instructions.
C. The parts covered by this specification document are subject to Mini-Circuits standard limited warranty and terms and conditions (collectively, "Standard Terms"); Purchasers of this part are entitled to the rights and benefits contained therein. For a full statement of the Standard Terms and the exclusive rights and remedies thereunder, please visit Mini-Circuits' website at www.minicircuits.com/MCLStore/terms.jsp

Product Marking

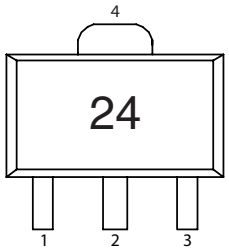

Markings in addition to model number designation may appear for internal quality control purposes.

Additional Detailed Technical Information

Additional information is available on our web site. To access this information enter the model number on our web site home page.

Performance data, graphs, s-parameter data set (.zip file)

Case Style: DF782

Plastic package, exposed paddle, lead finish: tin-silver over nickel

Tape & Reel: F55
7" reels with 20, 50, 100, 200, 500, 1K devices.

Suggested Layout for PCB Design: PL-019

Evaluation Board: TB-409-24+

Environmental Ratings: ENV08T2

Recommended Application Circuit

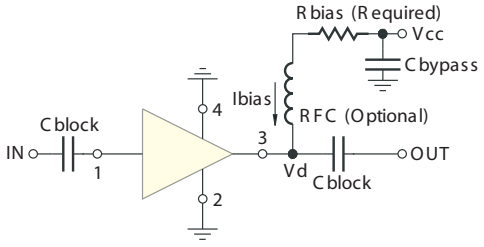

Test Board includes case, connectors, and components (in bold) soldered to PCB

R BIAS	
Vcc	**"1%" Res. Values (ohms) for Optimum Biasing**
8	28.7
9	41.2
10	53.7
11	66.5
12	78.7
13	90.9
14	105
15	115
16	127
17	140
18	154
19	165
20	178

Appendix E

SYM−63LH+ Data Sheet

Frequency Mixer SYM-63LH+

Level 10 (LO Power +10 dBm) 1 to 6000 MHz

The Big Deal

- Ultra broadband, 1 to 6000 MHz
- High isolation and good conversion loss across the band
- Low profile compact package

CASE STYLE: TTT166

Product Overview

Model SYM-63LH+ is an ultra broadband double balanced mixer utilizing core and wire transformers and a diode quad in a ring configuration. The transformers are designed to provide ultra wide bandwidth using simulation software together with Mini-Circuits proprietary transformer technology. These mixers provide an IF response from DC to 1000 MHz and are especially useful in wideband system applications such as IED.

Key Features

Feature	Advantages
Low conversion loss, 8dB for wide bandwidth	Low loss enables lower NF front ends thereby improving system sensitivity.
High LO to RF isolation	Less susceptibility to the LO signal interfering with system performance. Reduced levels of unwanted responses especially in a wideband system.
Broadband matching	The IF port VSWR is less than 1.5 to 1 over the specified frequency range. This simplifies the cascading of an amplifier following the mixer.
Compact low profile package 0.38 x 0.50 x 0.15”	Enables high density packaging
Insensitive to LO power level variations	Enable the use of an LO amplifier with reduced specs for gain flatness, consequently improving the potential to lower LO amplifier costs.

Surface Mount

Frequency Mixer

Level 10 (LO Power +10 dBm) 1 to 6000 MHz

SYM-63LH+

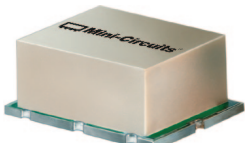

CASE STYLE: TTT166
PRICE: $12.95 ea. QTY (10-49)

+RoHS Compliant
The +Suffix identifies RoHS Compliance. See our web site for RoHS Compliance methodologies and qualifications

Maximum Ratings

Operating Temperature	-40°C to 85°C
Storage Temperature	-55°C to 100°C
RF Power	50mW
IF Current	40mA

Permanent damage may occur if any of these limits are exceeded.

Pin Connections

LO	2
RF	1
IF	3
GROUND	4,5,6

Features

- ultra wide bandwidth, 1-6000 MHz
- IF response to DC

Applications

- test equipment
- cable TV
- cellular
- PCS
- satellite distribution
- ISM/GPS
- WCDMA
- defence communications

Outline Drawing

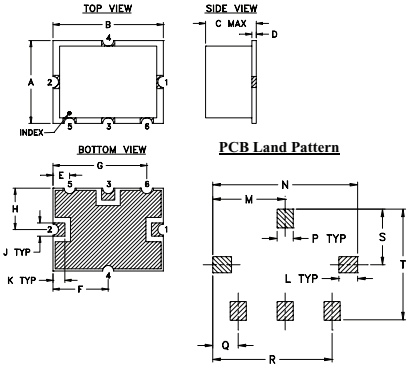

Suggested Layout,
Tolerance to be within ±.002

Outline Dimensions (inch / mm)

A	B	C	D	E	F	G	H	J
.38	.50	.15	.020	.075	.250	.425	.187	.050
9.65	12.70	3.81	0.51	1.91	6.35	10.80	4.75	1.27

K	L	M	N	P	Q	R	S	T	wt.
.050	.070	.270	.540	.060	.095	.445	.208	.415	grams
1.27	1.78	6.86	13.72	1.52	2.41	11.30	5.28	10.54	0.8

Demo Board MCL P/N: TB-12
Suggested PCB Layout (PL-079)

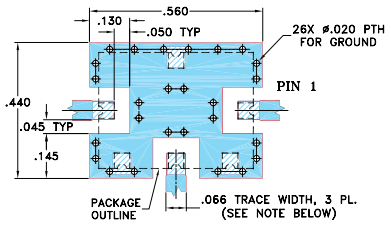

NOTE:

1. TRACE WIDTH IS SHOWN FOR ROGERS RO4350B WITH DIELECTRIC THICKNESS .030" ± .002"; COPPER: 1/2 OZ. EACH SIDE. FOR OTHER MATERIALS TRACE WIDTH MAY NEED TO BE MODIFIED.
2. THE USE OF SOLDER MASK OVER THE GROUND AREA UNDER THE UNIT AS SHOWN IS RECOMMENDED TO PREVENT POTENTIAL SHORTING. IF USER CHOOSES TO EXPOSE METAL UNDER THE ENTIRE UNIT GROUND PAD FOR IMPROVED GROUNDING, IT IS RECOMMENDED A SOLDER MASK DAM BE APPLIED AROUND EACH GROUND PAD TO ENSURE FILLET AND CONNECTION AT GROUND PADS.
3. BOTTOM SIDE OF THE PCB IS CONTINUOUS GROUND PLANE.

DENOTES PCB COPPER LAYOUT WITH SMOBC (SOLDER MASK OVER BARE COPPER), SEE NOTE 2.

DENOTES COPPER LAND PATTERN FREE OF SOLDER MASK

Electrical Specifications @ 25°C

FREQUENCY (MHz)		CONVERSION LOSS* (dB)				LO-RF ISOLATION (dB)						LO-IF ISOLATION (dB)						IP3 at center band (dBm)
LO/RF	IF	Mid-Band m			Total Range	L		M		U		L		M		U		
f_L-f_U		$\overline{X}$	σ	Max.	Max.	Typ.	Min.	Typ.	Min.	Typ.	Min.	Typ.	Min.	Typ.	Min.	Typ.	Min.	Typ.
1-6000	DC-1000	7.5	0.15	9.5	10.8	65	45	35	20	29	20	60	40	25	14	19	12	14

1 dB COMP.: +3 dBm typ.
* Conversion Loss at 30 MHz IF.
σ is a measure of repeatibility from unit to unit.

L = low range [f_L to 10 f_L]
U = upper range [f_U/2 to f_U]
M = mid range [10 f_L to f_U/2]
m= mid band [2f_L to f_U/2]

Typical Performance Data

Frequency (MHz)		Conversion Loss (dB)	Isolation L-R (dB)	Isolation L-I (dB)	VSWR RF Port (:1)	VSWR LO Port (:1)
RF	LO	LO +10dBm	LO +10dBm	LO +10dBm	LO +10dBm	LO +10dBm
1.00	31.00	5.83	65.41	60.62	1.68	3.60
10.00	40.00	6.07	63.21	58.28	1.09	3.54
100.00	130.00	6.21	53.47	46.17	1.04	3.45
145.00	175.00	6.21	51.34	43.08	1.04	3.46
505.00	535.00	6.28	42.90	33.70	1.37	2.72
1000.00	1030.00	6.65	41.76	34.89	2.07	1.72
1500.00	1530.00	7.31	32.97	23.84	2.07	1.27
2000.00	2030.00	6.87	30.92	24.37	2.01	1.70
3000.00	3030.00	8.60	26.67	34.89	2.42	2.64
4000.00	4030.00	7.94	28.22	18.49	1.76	2.75
5000.00	5030.00	8.24	36.41	19.92	2.09	2.09
5100.00	5130.00	8.18	38.17	20.34	2.05	2.18
5200.00	5230.00	8.20	40.26	20.55	1.86	2.33
5300.00	5330.00	8.25	42.62	20.82	1.65	2.57
5400.00	5430.00	8.34	43.72	21.01	1.60	2.77
5500.00	5530.00	8.43	42.20	21.03	1.76	2.76
5600.00	5630.00	8.60	39.70	21.01	2.11	2.84
5700.00	5730.00	8.76	37.69	21.00	2.61	2.88
5800.00	5830.00	8.85	36.36	20.92	2.89	2.84
6000.00	6030.00	9.28	34.92	20.45	2.77	2.19

Electrical Schematic

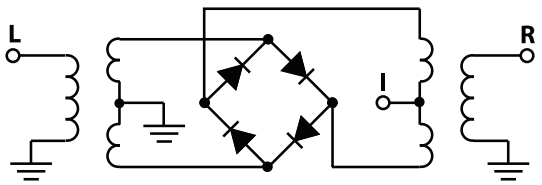

REV. B
M136981
ED-13824/3
SYM-63LH+
DJ/CP/AM
120424

SYM-63LH+
CONVERSION LOSS

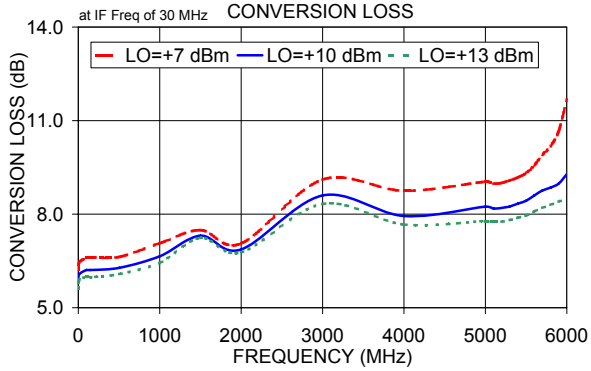

SYM-63LH+
L-R ISOLATION

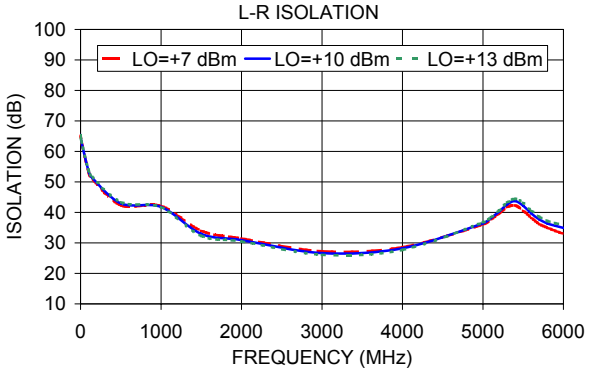

SYM-63LH+
L-I ISOLATION

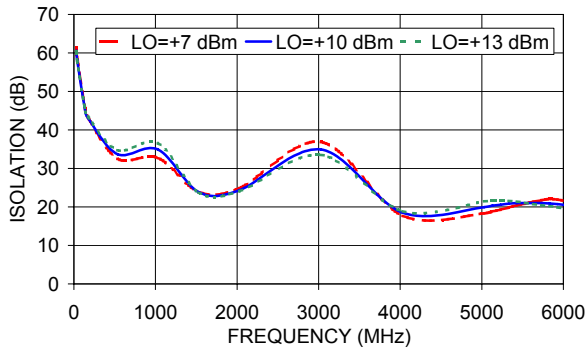

SYM-63LH+
RF VSWR

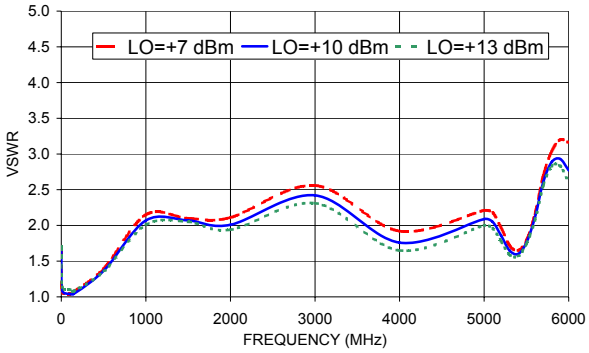

SYM-63LH+
LO VSWR

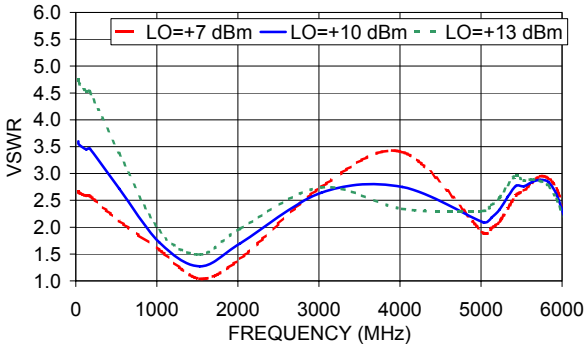

SYM-63LH+
IF VSWR

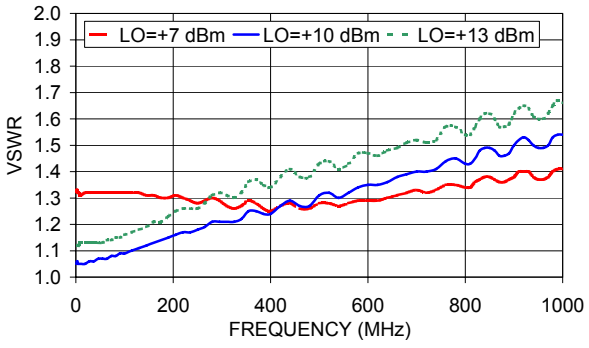

Bibliography

[1] J. C. Lin, "Noninvasive microwave measurement of respiration", *Proceedings of IEEE*, vol. 63, no. 10, p. 1530, Oct. 1975.

[2] B. Jang, S. Wi, J. Yook, M. Lee and K. Lee, "Wireless bio−radar sensor for heartbeat and respiration detection", *Progress in Electromagnetics Research C*, vol. 5, pp. 149−168, 2008.

[3] S. Myoung, J. Park, J. Yook and B. Jang, "2.4 GHz bio−radar system with improved performance by using phase−locked loop", *Microwave and Optical Technology Letters*, vol. 25, no. 9, pp. 2074−2076, Sept. 2010.

[4] S. Kim, G. Yun and J. Yook, "Wireless RF sensor structure for non−contact vital sign monitoring", *Korean Institute of Electromagnetic Engineering and science*, vol. 12, no. 1, pp. 37−44, Mar. 2012.

[5] H. Zhang, L. Li and Ke Wu, "24 GHz software−defined radar system for automotive applications", *European Conference on Wireless Technologies*, Munich, Oct. 2007, pp. 138−141.

[6] L. Chioukh, H. Boutayeb, Ke Wu and D. Deslandes, "Monitoring vital signs using remote harmonic radar concept", *European Radar Conference (EuRAD−11)*, Manchester, Oct. 2011, pp. 1269−1272.

[7] D. Droitcour, O. Lubecke, V. Lubecke, J. Lin and G. Kovac, "Range correlation and I/Q performance benefits in single−chip silicon Doppler radars for

noncontact cardiopulmonary monitoring", *IEEE Transaction on Microwave Theory and Techniques*, vol. 52, no. 3, pp. 838−848, Mar. 2004.

[8] E. Sultan, K. Manseta, A. Gandjbakhche and A. Daryoush,"Untethered helmet mounted functional near infrared biomedical imaging for hematoma detection", *In Proceedings of IEEE MTT−S International Microwave and RF Conference (IMaRC−2013)*, New Dehli, India, Dec. 2013, pp. 1−4.

[9] K. Manseta, A. Khwaja, E. Sultan, P. Daruwalla, K. Pourrezaei, L. Najafizadeh, A. Gandjbakhche and A. Daryoush,"Untethered helmet mounted functional near infrared biomedical imaging", *IEEE MTT−S International Microwave Symposium Digest*, Baltimore−MD, Jun. 2011, pp. 5−10.

[10] K. Manseta, E. Sultan, A. Khwaja, K. Pourrezaei, A. Joshi, L. Najafizadeh, A. Gandjbakhche, A. Daryoush, "Development challenges of brain functional monitoring using untethered broadband frequency modulated fNIR system", *IEEE Microwave Photonics Proceeding*, Montreal−Canada, 2010, pp. 295−299.

[11] A. Daryoush, "RF and microwave photonics in biomedical applications", *Ch.−9, Microwave Photonics: Devices and Applications*, Wiley, 2009.

[12] C. Stezer, G. Diskus, K. Lubke and H. Thim, "Microwave position sensor with sub millimeter accuracy", *IEEE Transaction on Microwave Theory and Technique*, vol. 47, no. 12, pp. 2621−2624, Dec. 1999.

[13] H. Zhang, L. Li and Ke. Wu, "Software−defined six−port radar technique for precision range measurements", *IEEE Sensors Journal*, vol. 8, no. 10, pp. 1745−1751, Oct. 2008.

[14] M. Shaji and M. Akhtar, "Microwave coplanar sensor system for detecting contamination in food products", *In Proceedings of IEEE MTT−S International Microwave and RF Conference (IMaRC−2013)*, New Delhi−India, Dec. 2013, pp. 1−4.

[15] A. Jha and M. Akhtar, "Automated RF measurement system for detecting adulteration in edible fluids", *In Proceedings of IEEE Applied Electromagnetics Conference (AEMC−13)*, Bhubaneswar−India, Dec. 2013, pp. 18−20.

[16] M. Akhtar, L. Feher and M. Thumm, "Noninvasive procedure for measuring the complex permittivity of resins, catalysts and other liquids using a partially filled rectangular waveguide structure", *IEEE Transactions on Microwave Theory and Techniques*, vol. 57, no. 2, pp. 458−470, Feb. 2009.

[17] M. Shete, M. Shaji and M. Akhtar, "Design of a coplanar sensor for the RF characterization of thin dielectric samples", *IEEE Sensors Journal*, vol. 13, no. 12, pp. 4706−4715, Dec. 2013.

[18] O. Lubecke, J. Lin, B. Park, C. Li, W. Massagram, V. Lubecke, A. Madsen, "Battlefield triage life signs detection techniques", *In Proc. SPIE Defense and Security Symposium*, vol. 6947− Radar Sensor Technology XII, no. 69470J, Apr. 2008.

[19] A. Aubert, B. Seps and F. Beckers, "Heart rate variability in athletes", *Sports Medicine*, vol. 33, no. 12, pp. 889−919, Oct. 2003.

[20] P. Kumar and T. Kumar, "A novel approach for clutter reduction in throughâĂŞthe−wall UWB radar imaging", *IETE Journal of Research*, vol. 58, no. 5, pp. 341−346, Sept. 2012.

[21] Y. An, B. Jang and J. Yook, "Detection of human vital signs and estimation of direction of arrival using multiple doppler radars", *Journal of The Korean Institute of Electromagnetic*, vol. 10, no. 4, pp. 250−255, Dec. 2010.

[22] D. Inserra and A. Tonello, "A Multiple antenna wireless testbed for the validation of DoA estimation algorithms", *International Journal of Electronics and Communications*, vol. 68, pp. 10−18, Jan. 2014.

[23] D. Inserra and A. Tonello, "A frequency domain LOS angle of arrival estimation approach in multipath channels", *IEEE Transactions on Vehicular Technology*, vol. 62. no. 6, pp. 2813−2818, Jul. 2013.

[24] A. Tonello and R. Rinaldo, "Frequency domain multiuser detection for impulse radio systems", *In Proceedings of IEEE Vehicular Technology Conference(VTC−05)*, Stockholm−Sweden, Jun. 2005, pp. 1381−1385.

[25] C. Gu and J. Lin, "Instrument−based noncontact Doppler radar vital sign detection system using heterodyne digital quadrature demodulation architecture", *IEEE Transaction on Instrumentation and Measurement*, vol. 59, no. 6, pp. 1580−1588, Jun. 2010.

[26] Y. Xiao, J. Lin, O. Lubecke and V. Lubecke, "Frequency tuning technique for remote detection of heartbeat and respiration using low−power double−sideband transmission in the Ka−Band", *IEEE Transaction on Microwave Theory and Techniques*, vol. 54, no. 5, pp. 2023−2032, May 2006.

[27] X. Yu, C. Li and J. Lin, "Two−dimensional noncontact vital sign detection using doppler radar array approach", *IEEE MTT−S International Microwave Symposium Digest (MTT−11)*, Baltimore, Jun. 2011, pp. 1−4.

[28] S. Guan, J. Rice, C. Li and G. Wang, "Bridge deflection monitoring using small, low−cost Radar sensors", *Structures Congress*, Boston−Massachusetts−USA, Apr. 2014, pp. 2853−2862.

[29] J. Bommer, A. Robb, R. Martinez, S. Ramamurthy, J. Harrigan, H. Muniganti, V. Mannangi and K. J. Vinoy, "Wireless aircraft fuel quantity indication system", *Sensors Applications Symposium*, Queenstown−New Zealand, Feb. 2014, pp. 305−310.

[30] B. Timby, *Fundamentals of nursing skills and concepts*, 9th Ed., Lippincott Williams & Wilkins, 2008, pp. 184−205.

[31] R. Page, "The early history of radar", *Proceedings of IRE*, vol. 50, no. 5, pp. 1232−1236, 1962.

[32] H. Shipton, "Radar History : The need for objectivity", *IEEE Transaction Aerospace Electronics Technology*, vol. AES−16, no. 2, p. 244, Mar. 1980.

[33] R. James, "History of radar", *IEE Review*, vol. 35, no. 9, pp. 343−349, 1989.

[34] M. Guarnieri, "The early history of radar", *IEEE Industrial Electronics Magazine*, vol. 4, no. 3, pp. 36−42, Sept. 2010.

[35] Y. Xiao, J. Lin, O. Lubecke and V. Lubecke, "Frequency tuning technique for remote detection of heartbeat and respiration using low−power double−sideband transmission in the Ka−Band", *IEEE Transaction on Microwave Theory and Techniques*, vol. 54, no. 5, pp. 2023−2032, May 2006.

[36] S. Nirmala, S. Dandapat and P. Bora, "Wavelet weighted diagnostic distortion measure for the Optic disc", *International Conference on Signal Processing and Communication(SPCOM−10)*, Bangalore−India, Jul. 2010, pp. 1−5.

[37] S. Nirmala, S. Dandapat and P. Bora, "Wavelet weighted blood vessel distortion measure for retinal images", *Biomedical Signal Processing and Control*, vol. 5, no. 4, pp. 282−291, Oct. 2010.

[38] L. Sharma, S. Dandapat and A. Mahanta, "ECG signal denoising using higher order statistics in Wavelet subbands", *Biomedical Signal Processing and Control*, vol. 5, no. 3, pp. 214−222, Jul. 2010.

[39] M. Manikandan and S. Dandapat, "Wavelet energy based diagnostic distortion measure for ECG", *Biomedical Signal Processing and Control*, vol. 2, no. 2, pp. 80−96, Apr. 2007.

[40] A. Tariq and H. Shiraz, "Doppler Radar vital signs monitoring using wavelet transform", *Proceedings of Antennas and Propagation Conference*, Loughborough−UK, Nov. 2010, pp. 293−296.

[41] J. Li and P. Stoica, "Efficient mixed−spectrum estimation with applications to target feature extraction", *IEEE Transaction on Signal Processing*, vol. 44, no. 2, pp. 281−295, Feb. 1996.

[42] S. Pavlov and S. Samkov, "Algorithm of signal processing in ultra wideband radar designed for remote measuring parameters of patient's cardiac activity", *Second International Workshop Ultra wideband and Ultrashort Impulse Signals*, Sevastpole−Ukraine, Sept. 2004, pp. 205−207.

[43] A. Madsen, N. Petrochilos, O. Lubecke and V. Lubecke, "Signal processing methods for Doppler radar heart rate monitoring", *Signal Processing Techniques for Knowledge Extraction and Information Fusion*, pp. 121−140 , 2008.

[44] E. Sharifahmadian and A. Ahmadian, "Adaptive signal processing algorithm for remote detection of heart rate (HR) using ultra−wideband waveforms based on principal component analysis", *Annual International Conference of the IEEE Engineering in Medicine and Biology Society (EMBC 2009)*, Minnesota−USA, 2009 , pp. 5717−5720.

[45] M. Rahman, B. Jang and K. Kim, "A new digital signal processor for Doppler radar cardiopulmonary monitoring system", *International Conference on Electrical and Computer Engineering*, Dhaka, Dec. 2008, pp. 76−79.

[46] M. Vergara, N. Petrochilos, O. Lubecke, A. Madsen and V. Lubecke, "Blind source separation of human body motion using direct conversion Doppler radar", *IEEE MTT−S International Microwave Symposium Digest*, Atlanta−USA, Jun. 2008, pp. 1321−1324.

[47] M. Vergara, O. Lubecke and V. Lubecke, "DC information preservation for cardiopulmonary monitor utilizing CW Doppler radar", *IEEE Engineering in Medicine and Biology Society Annual International Conference*, Vancouver, Aug. 2008, pp. 1246−1249.

[48] T. Chin, K. Lin, S. Chang and C. Chang, "A fast clutter cancellation method in quadrature Doppler radar for noncontact vital signal detection", *IEEE MTT−S International Microwave Symposium Digest*, Anaheim−CA, May. 2010, pp. 764−767.

[49] J. Cheng, J. Yeh, H. Yang, J. Tsai, J. Lin and T. Huang, "40$-GHz$ vital sign detection of heartbeat using synchronized motion technique for respiration signal suppression", *Proceedings of the 42nd European Microwave Conference*, Amsterdam−The Netherlands, Nov. 2012, pp. 21−24.

[50] A. Singh, and V. Lubecke, "Respiratory monitoring using a Doppler radar with passive harmonic tags to reduce interference from environmental clutter", *IEEE Engineering in Medicine and Biology Society Annual International Conference*, Minneapolis−MN, Sept. 2009, pp. 3837− 3840.

[51] D. Zito, D. Pepe, M. Mincica, F. Zito, D. Rossi, A. Lanata, E. Scilingo and A. Tognetti, "Wearable system−on−a−chip UWB radar for contact−less cardiopulmonary monitoring: Present status", *IEEE Engineering in Medicine and Biology Society Annual International Conference*, Vancouver−BC, Aug. 2008, pp. 5274−5277.

[52] C. Wu and Z. Huang, "Using the phase change of a reflected microwave to detect a human subject behind a barrier", *IEEE Transaction on Biomedical Engineering*, vol. 55, no. 1, pp. 267−272, Jan. 2008.

[53] J. Lin, "Microwave sensing of physiological movement and volume change: A review", *Bioelectromagnetics*, vol. 13, pp. 557−565, 1992.

[54] C. Gu, J. Long, J. Huangfu, S. Qiao, W. Cui, W. Ma and L. Ran, "An instruments−built Doppler radar for sensing vital signs", *8th International Symposium on Antennas, Propagation and EM Theory*, Kunming, Nov. 2008, pp. 1398−1401.

[55] F. Wang, C. Li, C. Hsiao, T. Horng, J. Lin, K. Peng, J. Jau, J. Li and C. Chen, "An injection−locked detector for concurrent spectrum and vital sign sensing", *IEEE MTT−S International Microwave Symposium Digest*, Anaheim−CA, May 2010, pp. 768−771.

[56] I. Immoreev and T. Tao, "UWB Radar for patient monitoring", *IEEE Aerospace and Electronic Systems Magazine*, vol. 23, no. 11, pp. 11−18, Nov. 2008.

[57] A. Stove, "Linear FMCW Radar techniques", *IEE Proceedings−F*, vol. 139, no. 5, pp. 343−350, Oct. 1992.

[58] S. Ivashov, V. Razevig, A. Sheyko and I. Vasilyev, "Detection of human breathing and heartbeat by remote radar", *Progress in Electromagnetic Research Symposium*, Italy, Mar. 2004, pp. 663−666.

[59] W. Jianqi, Z. Chongxun, L. Guohua and J. Xijing, "A new method for identifying the life parameters via radar", *EURASIP Journal on Advances in Signal Processing*, vol. 2007, no. 1, pp. 1−8, 2007.

[60] L. Anitori, A. Jong and F. Nennie, "FMCW radar for life−sign detection", *IEEE Radar Conference*, Pasadena−CA, May. 2009, pp. 1−6.

[61] A. Wiesner, "A multifrequency interferometric CW radar for vital signs detection", *IEEE Radar Conference*,Pasadena−CA, May. 2009, pp. 1−4.

[62] A. Droitcour, V. Lubecke, J. Lin and O. Lubecke, "A microwave radio for Doppler radar sensing of vital signs", *IEEE MTT−S International Microwave Symposium Digest*, Phoenix−AZ−USA, May. 2001, pp. 175−178.

[63] A. Droitcour, O. Lubecke, V. Lubecke and J. Lin, "0.25Îijm CMOS and BiCMOS Single Chip Direct Conversion Doppler Radars For Remote Sensing of Vital Signs", *IEEE International Solid−State Circuits Conference Digest (ISSCC−2002)*, San Francisco−USA, Feb. 2002, pp. 348−349.

[64] K. Chen, Y. Huang, J. Zhang and A. Norman, "Microwave life−detection systems for searching human subjects under earthquake rubble and behind barrier", *IEEE Transaction on Biomedical Engineering*, vol. 47, no. 1, pp. 105−114, Jan. 2000.

[65] S. Dragan, B. Park, and O. Lubecke, "Experimental evaluation of multiple antenna techniques for remote sensing of physiological motion", *IEEE MTT−S International Microwave Symposium*, Honolulu, Jun. 2007, pp. 1735−1738.

[66] X. Yu and J. Lin, "Noise analysis for noncontact vital sign detectors", *11th IEEE Annual Wireless and Microwave Technology Conference (WAMICON)*, Melbourne−FL, Apr. 2010, pp. 1−4.

[67] H. Kuo, H. Wang, P. Wang and H. Chuang, "60−GHz millimeter−wave life detection system with clutter canceller for remote human vital−signal sensing", *IEEE MTT−S International Microwave Workshop Series on Millimeter Wave Integration Technologies (IMWS)*, Sitges, Sept. 2011, pp. 93−96.

[68] A. Lazaro, D. Girbau and R. Villarino, "Techniques for clutter suppression in the presence of body movements during the detection of respiratory activity through UWB Radars", *Sensors*, vol. 14, pp. 2595−2618, 2014.

[69] Y. Xiao, J. Lin, O. Lubecke and V. Lubecke, "A Ka−band low power Doppler radar system for remote detection of cardiopulmonary motion", *In Proceedings of the 27th IEEE Annual Conference on Engineering in Medicine and Biology*, Shanghai−China, Sept. 2005, pp. 7151−7154.

[70] B. Park, O. Lubecke and V. Lubecke, "Arctangent demodulation with DC offset compensation in quadrature Doppler radar receiver systems", *IEEE Transaction on Microwave Theory and Techniques*, vol. 55, no. 5, pp. 1073−1079, May. 2007.

[71] C. Li, Y. Xiao and J. Lin, "Design guidelines for radio frequency non−contact vital sign detection", *Proceedings of the 29th Annual International Conference of the IEEE EMBS*, Lyon−France, Aug. 2007, pp.1651−1654.

[72] X. Yu, C. Li and J. Lin, "Two−dimensional noncontact vital sign detection using Doppler radar array approach", *IEEE MTT−S International Microwave Symposium Digest*, Baltimore, Jun. 2011, pp.1−4.

[73] C. Gu, C. Li, J. Lin, J. Long, J. Huangfu and L. Ran, "Instrument−based noncontact Doppler radar vital sign detection system using heterodyne digital quadrature demodulation architecture", *IEEE Transaction on Instrumentation and Measurement*, vol. 59, no. 6, pp. 1580−1588, Jun. 2010.

[74] Y. Immoreev and S. Samkov, "Ultra−wideband radar for remote measuring of main parameters of patientâĂŹs vital activity", *IEEE International Workshop on the Ultra Wideband and Ultra Short Impulse Signals (UWBUSIS−02)*, Kharkov−Ukraine, Oct. 2002, pp. 1−4.

[75] C. Li, Y. Xiao and J. Lin, "Experiment and spectral analysis of a low−power Ka−Band heartbeat detector measuring from four sides of a human body", *IEEE Transaction on Microwave Theory and Techniques*, vol. 54, no. 12, pp. 4464−4471, Dec. 2006.

[76] C. Li and J. Lin, "Random body movement cancellation in Doppler radar vital sign detection", *IEEE Transaction on Microwave Theory and Techniques*, vol. 56, no. 12, pp. 3143− 3152, Dec. 2008.

[77] D. Girbau, A. Lazaro, A. Ramos and R. Villarino, "Remote sensing of vital signs using a Doppler radar and diversity to overcome null detection", *IEEE Sensors Journal*, vol. 12, no. 3, pp. 512−518, Mar. 2012.

[78] J. Long, C. Gu, Y. Tao, J. Huangfu, S. Qiao, W. Cui, W. Ma and L. Ran, "A novel direct−conversion structure for non−contact vital sign detection system", *8th International Symposium on Antennas, Propagation and EM Theory (ISAPE−2008)*, Kunming, Nov. 2008, pp. 1282−1285.

[79] L. Chioukh, H. Boutayeb, D. Deslandes and Ke Wu, "Multi−frequency Radar Systems for Monitoring Vital Signs", *Proceedings of Asia−Pacific Microwave Conference (APMC)*, Yokohama, Dec. 2010, pp. 1669−1672.

[80] R. Fletcher and J. Han, "Low−cost differential front−end for Doppler radar vital sign monitoring", *IEEE MTT−S International Microwave Symposium Digest*, Boston−MA, Jun. 2009, pp. 1325−1328.

[81] J. Oum, D. Kim and S.Hong, "Two frequency radar sensor for non−contact vital signal monitor", *IEEE MTT−S International Microwave Symposium Digest*, Atlanta−GA, Jun. 2008, pp. 919−922.

[82] G. Deschamps, "Microstrip microwave antennas", *3rd UASF symposium on antennas*, 1953.

[83] R. Garg and K. Ray, *Microstrip line antenna design*, Artech House, USA, 2003.

[84] R. Garg, P. Bhartia, I. Bahl and A. Ittipiboon, *Microstrip Antenna Design Handbook*, Artech House, USA, 2001.

[85] A. Rathore, R. Nilavalan, H. Tarboush and T. Peter, "Compact dual−band (2.4/5.2 GHz) monopole antenna for WLAN applications", *International Workshop on Antenna Technology*, Mar. 2010, pp. 1−4.

[86] R. Garg and K. Rao, "Dual frequency microstrip antennas", *Electronics Letters*, vol. 19, pp. 357−358, May. 1983.

[87] A. Bhattacharyya and R. Garg, "A microstrip array of concentric annular rings", *IEEE Transaction on Antennas Propagation*, vol. 33, pp. 655−659, Jun. 1985.

[88] R. Garg, and V. Reddy, "Edge feeding of microstrip ring antennas", *IEEE Transaction on Antennas Propagation*, vol. 51, pp. 1941−1946, Aug. 2003.

[89] A. Pal, S. Behera and K. Vinoy, "Design of multi−frequency microstrip antennas using multiple rings", *IET Microwaves, Antennas & Propagation*, vol. 3, no. 1, pp. 77−84, Feb. 2009.

[90] M. Solanki, U. Kiran and K. Vinoy, "Broadband designs of a triangular microstrip antenna with a capacitive feed", *Journal of Microwaves, Optoelectronics and Electromagnetic Applications*, vol. 7, no. 1, pp. 44−53, Jun. 2008.

[91] K. J. Vinoy, "Multifunctional microstrip antennas for wireless applications", *IEEE Indian Antenna Week (IEEE IAW)*, Kolkatta−India, Dec. 2011, pp. 1−4.

[92] R. Gupta, U. Sharma, P. Sayanu and G. Kumar, "MEMS based reconfigurable dualband antenna", *Microwave and Optical Technology letters*, vol. 50, no. 6, pp. 1570−1575, Jun. 2008.

[93] Z. Park, C. Li and J. Lin, "A broadband microstrip antenna with improved gain for noncontact vital sign radar detection", *IEEE Antennas Wireless Propagation Letters*, vol. 8, pp. 939−942, Aug. 2009.

[94] Z. Park and J. Lin, "A beam steering broadband microstrip antenna for non-contact vital sign radar detection", *IEEE Antennas Wireless Propagation Letters*, vol. 10, pp. 235−238, Mar. 2011.

[95] W. Swelam, M. Soliman, A. Gomaa and T. Taha, "Compact dual−band microstrip patch array antenna for MIMO 4G communication systems", *IEEE Antennas and Propagation Society International Symposium (APSURSI−2010)*, Toronto, Jul. 2010, pp. 1−4.

[96] Y. Khraisat, "Design of 4 elements rectangular microstrip patch antenna with high gain for 2.4 GHz applications", *Modern Applied Science*, vol. 6, no. 1, pp. 68−74, Jan. 2012.

[97] C. Ghosh and S. Parui, "Design, analysis and optimization of a slotted microstrip patch antenna array at frequency 5.25 GHz for WLAN−SDMA system", *International Journal on Electrical Engineering and Informatics*, vol. 2, no. 2, pp. 102−112, 2010.

[98] J. Chitra and V. Nagarajan, "Double L−slot microstrip patch antenna array for WiMax and WLAN applications", *Computer and Electrical Engineering*, vol. 39, no. 3, pp. 1026−1041, Apr. 2013.

[99] K. Lau, K. Lukand and K. Lee, "Wideband U−slot microstrip patch antenna array", *IEE Proceedings of Microwaves, Antennas and Propagation*, vol. 148 ,no. 1, pp. 41−44, 2001.

[100] R. Li, T. Wu and M. Tentzeris, "A Dual−Band Unidirectional Coplanar Antenna for 2.4−5−GHz Wireless Applications", *Asia−Pacific Microwave Conference (APMC−08)*, Macau, Dec− 2008, pp−1−4.

[101] J. Baena et al., "Equivalent−circuit models for split−ring resonators and complementary split−ring resonators coupled to planar transmission lines", *IEEE Transaction on Microwave Theory and Techniques*, vol. 53, no. 4, pp. 1451−1461, Apr. 2005.

[102] R. Munson, “Conformal microstrip antennas and microstrip phased arrays”, *IEEE Transaction on Antennas and Propagation*, vol. AP−22, no. 1, pp. 74−78, Jan. 1974.

[103] E. Wilkinson, “An N−Way Hybrid Power Divider”, *IRE Transactions on Microwave Theory and Techniques*, vol. 8, no. 1, pp. 116−118, Jan. 1960.

[104] C. Monzon, “ A small dual−frequency transformer in two sections”, *IEEE Transaction on Microwave Theory Techniques*, vol. 51, no. 4, pp. 1157−1161, Apr. 2003.

[105] S. Srisathit, M. Chongcheawchamnan and A. Worapishet, “Design and realization of dual−band 3 dB power divider based on two−section transmission−line topology”, *Electronics Letters*, vol. 39, no. 9, pp. 723−724, May 2003.

[106] L. Wu, H. Yilmaz, T. Bitzer, A. Pascht and M. Berroth, “A dual−frequency Wilkinson power divider: For a frequency and its first harmonic”, *IEEE Microwave and Wireless Component Letters*, vol. 5, no. 2, pp. 107−109, Feb. 2005.

[107] L. Wu, S. Sun, H. Yilmaz and M. Berroth, “A dual−frequency Wilkinson power divider”, *IEEE Transaction on Microwave Theory Techniques*, vol. 54, no. 1, pp. 278−284, Jan. 2006.

[108] Z. Jia, Q. Zhu and F. Ao, “A 2−Way Broad−Band Microstrip Matched Power Divider”, *Proceedings of International Conference on Communications, Circuits and Systems*, Guilin, vol. 4, Jun. 2006, pp. 2592−2596.

[109] S. Oh et.al., “An unequal Wilkinson power divider with variable dividing ratio”, *IEEE MTT−S International Microwave Symposium*, Honolulu−HI, Jun. 2007, pp. 411− 414.

[110] M. Cheng and F. Wong, “A New Wilkinson power divider design for dualband application”, *IEEE Microwave and Wireless Components Letters*, vol. 17, no. 9, pp. 664−666, Sept. 2007.

[111] M. Park and B. Lee, "A Dual−Band Wilkinson power divider", *IEEE Microwave and Wireless Components Letters*, vol. 18, no. 2, pp. 85−87, Feb. 2008.

[112] A. Naghavi, M. Aghmiyouni, M. Jahanbakht and A. Neyestanak, "Hybrid wideband microstrip Wilkinson power divider based on lowpass filter optimized using particle swarm method", *Journal of Electromagnetic Waves and Applications*, vol. 24, no. 14−15, pp. 1877−1886, Aug. 2010.

[113] V. Dao, B. Choi and C. Park, "Dual−band LNA for 2.4/5.2GHz applications", *Asia−Pacific Microwave Conference(APMC)*, Yokohama, Dec. 2006, pp. 413−416.

[114] S. Yoo and H. Yoo, "A Compact Dualband LNA Using Self−matched Capacitor", *IEEE International Workshop on Radio−Frequency Integration Technology(RFIT)*, Rasa−Sentosa, Dec. 2007, pp. 227−230.

[115] M. Martins, J. Fernandes and M. Silva, "Techniques for Dual−Band LNA Design using Cascode Switching and Inductor Magnetic Coupling", *IEEE International Symposium on Circuits and Systems(ISCAS−2007)*, New Orleans−LA, May. 2007, pp. 1449−1452.

[116] H. Hashemi and A. Hajimiri, "Concurrent multiband low−noise amplifiers−theory, design, and applications", *IEEE Transactions on Microwave Theory and Techniques*, vol. 50, no. 1, pp. 288−301, Jan. 2002.

[117] D. Pozar, *Microwave Engineering*, 3rd Edition, Wiley−India, 2007.

[118] M. Amor, A. Fakhfakh, H. Mnif and M. Loulou, "Dual band CMOS LNA design with current reuse topology", *International Conference on Design and Test of Integrated Systems in Nanoscale Technology (DTIS 2006)*, Tunis, Sept. 2006, pp. 57−61.

[119] H. Atwater, "Microstrip Reactive Circuit Elements", *IEEE Transactions on Microwave Theory and Techniques*, vol. 31, no. 6, pp. 488−491, Jun. 1983.

[120] Y. Cassivi and Ke Wu, "Low cost microwave oscillator using substrate integrated waveguide cavity", *IEEE Microwave and Wireless Components Letters*, vol. 13, no. 2, pp. 48−50, Feb. 2003.

[121] N. Kumar and G. Kumar, "Biological effects of cell tower radiation on human body", *12th International Symposium on Microwave and Optical Technology (ISMOT−2009)*, New Delhi−India, Dec. 2009, pp. 1365−1368.

[122] C. Chou and J. Andrea, "Subcommittee co−chairs, IEEE Standard for Safety Levels with Respect to Human Exposure to Radio frequency Electromagnetic Field, 3kHz to 300 GHz [IEEE Std C95.1âĎć−2005(Revision of IEEE Std C95.1−1991)]", IEEE, New York, NY, USA, Apr. 2006.

[123] Brijesh Iyer, M. Garg, N. P. Pathak and D. Ghosh, "Concurrent dualband RF system for human respiration rate and heartbeat detection", *Procedings of International Conference of Information and Communication Technologies (ICT−2013)*, Tamilnadu−India, Apr. 2013, pp. 563−567.

[124] Brijesh Iyer, M. Garg, N. P. Pathak and D. Ghosh, "Contactless detection and analysis of human vital signs using concurrent Dual−Band RF system", *Elsevier Procedia Engineering*, vol. 64, pp. 185−194, 2013.

[125] Brijesh Iyer, A. Kumar, N. P. Pathak and D. Ghosh, "Concurrent multiband RF system for search and rescue of human life during natural calamities", *First IEEE MTT−S International Microwave and Radio frequency Conference (IMaRC−2013)*, New Delhi−India, Dec. 2013, pp. 1−4.

[126] Brijesh Iyer, A. Kumar and N. P. Pathak, "Design and analysis of concurrent dual−band subsystems for WLAN applications", *International Conference on Signal Processing and Communication (ICSC−2013)*, Noida−india, Dec. 2013, pp. 57−61.

[127] Brijesh Iyer and N. P. Pathak, "Concurrent dual−band LNA for non−invasive vital sign detection", *Microwave and Optical Technology Letters*, vol. 56, no. 2, pp. 391−394, Feb. 2014.

[128] R. Robergs, and R. Landwehr, "The surprising history of the 'HR_{max}=220−age' equation", *Journal of Exercise Physiology*, vol. 5, no. 2, pp. 1−10, May. 2002.

[129] J. Adams, "How to design an invisible aircraft", *IEEE Spectrum*, pp. 26−31, Apr. 1988.

[130] G. Vishal and N. Bansal, "Smart occupancy sensors to reduce energy consumption", *Energy Buildings*, vol. 32, no. 1, pp. 81−87, 2000.

[131] Market Report by Aricent Inc., "Home energy management−beyond the numbers", 2010, [on line]: available at www. aricent. com pdf Aricent_Group_HEMS.pdf.

[132] P. Zappi, E. Farella and L. Benini, "Enhancing the spatial resolution of presence detection in a PIR based wireless surveillance network", *IEEE Conference on Advanced Video and Signal Based Surveillance (AVSS−2007)* , London−UK, Sept. 2007, pp. 295−300.

[133] D. Caicedo and A. Pandharipande, "Ultrasonic array sensor for indoor presence detection", *20th European Signal Processing Conference (EUSIPCO 2012)*, Bucharest−Romania, Aug. 2012, pp. 175−179.

[134] G. Reyes, D. Wang, R. Nair, C. Li, X. Li and J. Lin, "VitalTrack: A Doppler Radar sensor platform for monitoring activity levels", *IEEE Topical Conference on Biomedical Wireless Technologies, Networks, and Sensing Systems (BioWireleSS−2012)*, Santa Clara−CA, Jan. 2012, pp. 29−32.

[135] L. Lu, C. Li and D. Lie, "Experimental demonstration of noncontact pulse wave velocity monitoring using multiple Doppler radar sensors", *Annual International Conference of Engineering in Medicine and Biology Society (EMBC−2010)*, Buenos Aires, Sept. 2010, pp. 5010−5013.

[136] C. Song, E. Yavari, A. Singh, O. Lubecke and V. Lubecke, "Detection sensitivity and power consumption vs. operation modes using system−on−chip based Doppler radar occupancy sensor", *IEEE Topical Conference on Biomedical*

Wireless Technologies, Networks, and Sensing Systems (BioWireleSS−12), Santa Clara−CA, Jan. 2012, pp. 17−20.

[137] E. Yavari, H. Jou, V. Lubecke, and O. Lubecke, "Doppler Radar Sensor for Occupancy Monitoring", *IEEE Radio and Wireless Symposium (RWS)*, Austin, Jan. 2013, pp. 316−318.

[138] S. Chandran, *Advances in Direction−of−Arrival Estimation*, Artech House, Inc. Norwood, MA, 2006.

[139] M.Isar, E. Yavari and O. Lubecke, "A low cost simple RF front end using time−domain multiplexing for direction of arrival estimation of physiological signals", *IEEE MTT−S International Microwave Symposium Digest (IMS−2013)*, Seattle−WA, Jun. 2013, pp. 1−4.

[140] A. Yong, B. Jang and J. Yook, "Detection of human vital signs and estimation of direction of arrival using multiple Doppler radars", *Journal of Korean Institute of Electromagnetic Engineering and Science*, vol. 10, no. 4, pp. 250−254, Dec. 2010.